Thesis

Topology and Strong correlation effect of Hidden symmetry breaking superconductor

Kosuke Nogaki

Department of Physics, Kyoto University

December, 2023

Abstract

Odd-parity superconductivity serves as a foundational platform for realizing topological superconductivity, wherein Majorana fermions emerge at the edges or defects of systems. In the realm of quantum computation, Majorana fermions are recognized as key candidates for fault-tolerant quantum computing. Consequently, the pursuit and realization of topological superconductivity have been central topics in condensed matter physics. Among the various potential candidates, spin-triplet superconductors are particularly promising due to their odd parity of inversion symmetry. However, naturally occurring spin-triplet superconductors are exceedingly rare, leading to a demand for alternative principles to achieve odd-parity superconductivity. In 2012, Yoshida *et al.* introduced a groundbreaking principle, suggesting that sublattice degrees of freedom could enable the formation of odd-parity superconductivity in spin-singlet superconductors. About a decade after this proposal, the discovery of $CeRh_2As_2$ by Khim *et al.* in 2021, which exhibits a multiple superconducting phase diagram, has attracted considerable attention. This discovery has spurred numerous experimental studies aimed at elucidating the characteristics of $CeRh_2As_2$, unveiling several mysteries. In light of this context, this thesis focuses on the topological aspects and strong correlation effects in $CeRh_2As_2$, as well as field-induced superconductivity, which is intrinsically linked to the sublattice degrees of freedom.

First, we establish the presence of topological crystalline superconductivity in the high-field phase of $CeRh_2As_2$. By clarifying the algebraic relationships of the space group, we demonstrate that a one-dimensional odd-parity superconducting state can be defined within a restricted Hilbert space. This space is conceptualized as a glide-symmetry-preserved one-dimensional subspace embedded in the full three-dimensional space. Within this framework, we define the Zak phase in this one-dimensional domain and express it through a Fermi-surface formula. These formulas are instrumental in indicating the topological number through the shape of the Fermi surface. Conducting electronic structure calculations based on density functional theory, we predict the existence of topological crystalline superconductivity. Furthermore, the validity of our formulas is corroborated by analyzing a simple tight-binding model, applicable across all odd-parity irreducible representations.

Second, we delve into the strong correlation effects in $CeRh_2As_2$. While the phase diagram of this material can be interpreted using Yoshida *et al.*'s original proposal, discrepancies arise

concerning the value of the parity transition field. To address this, we developed a bilayer Rashba-Hubbard model, which we analyzed using the fluctuation-exchange approximation. This model highlights the interplay between staggered Rashba spin-orbit coupling and magnetic fields, leading us to discover two-dimensional XY-type magnetic fluctuations. These fluctuations are consistent with the nuclear-magnetic resonance measurements reported by Kitagawa *et al.*. Further, by solving the linearized Éliashberg equation, we observed a parity transition characterized by a dominant $d_{x^2-y^2}$-wave and a subdominant p-wave gap function, both contributing to superconductivity. Our phase diagram, for a wide range of spin-orbit coupling strengths, indicates a significant enhancement of parity transition fields due to antiferromagnetic fluctuations. Notably, these antiferromagnetic quantum critical fluctuations confer robustness to the system against external magnetic fields.

Third, we introduce a novel mechanism for field-induced superconductivity. Historically, field-induced superconductivity has been observed in Chevrel-phase materials and organic superconductors, typically attributed to the Jaccarino-Peter effect. Additionally, in uranium-based superconductors, this phenomenon is linked to ferromagnetic quantum critical fluctuations. Recently, the discovery of a field-induced phase transition within the superconducting state of $CeRh_2As_2$ has shed light on the role of sublattice degrees of freedom in strongly correlated superconductors. Notably, certain uranium-based superconductors and the locally noncentrosymmetric cerium-based superconductor $CeSb_2$, along with magic-angle twisted trilayer graphene, also exhibit field-induced superconductivity. These observations in cerium- and uranium-based heavy fermion superconductors, as well as in magic-angle twisted trilayer graphene, underscore the potential of electron correlation effects in driving superconductivity. In our study, we demonstrate how the degeneracy of multipole fluctuations can be lifted, creating an unconventional channel for inter-sublattice Cooper pairing. The application of a magnetic field, which disrupts time-reversal symmetry, facilitates the emergence of unconventional Cooper pairing, driven by these degeneracy-lifted multipole fluctuations. Our calculated phase diagrams indicate the formation of a field-induced odd-parity superconducting state across a wide spectrum of spin-orbit coupling strengths.

Contents

List of publications

Papers related to the thesis

1. Kosuke Nogaki, Akito Daido, Jun Ishizuka, and Youichi Yanase,
   Topological crystalline superconductivity in locally noncentrosymmetric $CeRh_2As_2$,
   Phys. Rev. Research **3**, L032071 (2021).

2. Kosuke Nogaki and Youichi Yanase,
   Even-odd parity transition in strongly correlated locally noncentrosymmetric superconductors: Application to $CeRh_2As_2$,
   Phys. Rev. B **106**, L100504 (2022).

3. Kosuke Nogaki and Youichi Yanase,
   Field-induced superconductivity mediated by odd-parity multipole fluctuation,
   arXiv:2312.07053

Published papers not included in the thesis

1. Kosuke Nogaki and Youichi Yanase,
   Strongly parity-mixed superconductivity in the Rashba-Hubbard model,
   Phys. Rev. B **102**, 165114 (2020).

2. Markus Wallerberger, Samuel Badr, Shintaro Hoshino, Sebastian Huber, Fumiya Kakizawa, Takashi Koretsune, Yuki Nagai, Kosuke Nogaki, Takuya Nomoto, Hitoshi Mori, Junya Otsuki, Soshun Ozaki, Thomas Plaikner, Rihito Sakurai, Constanze Vogel, Niklas Witt, Kazuyoshi Yoshimi, and Hiroshi Shinaoka,
   sparse-ir: Optimal compression and sparse sampling of many-body propagators,
   SoftwareX **21**, 101266 (2023).

3. Kosuke Nogaki and Hiroshi Shinaoka,
Bosonic Nevanlinna Analytic Continuation,
Journal of the Physical Society of Japan **92**, 035001 (2023).

4. Hiroshi Shinaoka, Markus Wallerberger, Yuta Murakami, Kosuke Nogaki, Rihito Sakurai, Philipp Werner, and Anna Kauch *Multiscale Space-Time Ansatz for Correlation Functions of Quantum Systems Based on Quantics Tensor Trains*,
Phys. Rev. X **13**, 021015 (2023).

5. Kosuke Nogaki, Jiani Fei, Emanuel Gull, and Hiroshi Shinaoka,
Nevanlinna. jl: A Julia implementation of Nevanlinna analytic continuation,
SciPost Phys. Codebases 19 (2023).

6. Ryuji Hakuno, Kosuke Nogaki, and Youichi Yanase,
Magnetism and superconductivity in mixed-dimensional periodic Anderson model for UTe_2,
arXiv:2306.00405

7. Xuezhi Chen, Le Wang, Jun Ishizuka, Kosuke Nogaki, Yiwei Cheng, Fazhi Yang, Renjie Zhang, Zhenhua Chen, Fangyuan Zhu, Youichi Yanase, Baiqing Lv, Yaobo Huang,
Coexistence of near-E_F *flat band and van Hove singularity in a two-phase superconductor*,
arXiv:2309.05895

8. Jun Ishizuka, Kosuke Nogaki, Manfred Sigrist, Youichi Yanase,
Correlation-induced Fermi surface evolution and topological crystalline superconductivity in $CeRh_2As_2$
arXiv:2311.00324

Chapter 1

Introduction

This chapter introduces the *locally* non-centrosymmetric heavy-fermion superconductor $CeRh_2As_2$ and related topics. First, we explain the concept of the locally non-centrosymmetric crystalline structure and their indication on the electronic structure and the superconducting state (Sec. 1.1). The locally-inversion symmetry broken structure impacts as the staggered spin-orbit coupling which leads to the non-trivial spin-structure in the Kramers doublets. Second, we summarize all experimental results including the thermodynamic, spectroscopic, transport, and nuclear resonance measurements are summarized (Sec. 1.2). Some experiments serve the theoretical future problems. To conclude this chapter, we overview the organization of the thesis (Sec. 1.3)

This chapter delves into the intriguing property of the *locally* non-centrosymmetric heavy-fermion superconductor $CeRh_2As_2$ and associated topics. Initially, we explore the concept of locally non-centrosymmetric crystalline structures and their implications for electronic structure and superconducting states (Sec. 1.1). The locally broken inversion symmetry introduces staggered spin-orbit coupling, leading to non-trivial spin structures within the Kramers doublets. Subsequently, we provide a comprehensive summary of all experimental findings, encompassing thermodynamic, spectroscopic, transport, and nuclear resonance measurements (Sec. 1.2). These experimental insights pose intriguing theoretical challenges for future research. To conclude this chapter, we offer an overview of the thesis's organization and the direction of our investigation (Sec. 1.3).

1.1 Local inversion symmetric breaking and odd-parity superconductivity

Locally non-centrosymmetric superconductors possess a distinctive crystalline structure where inversion symmetry is broken at the sites of heavy ions while being preserved in the intermediate regions. Similar to the well-known phenomena associated with global inversion symmetry

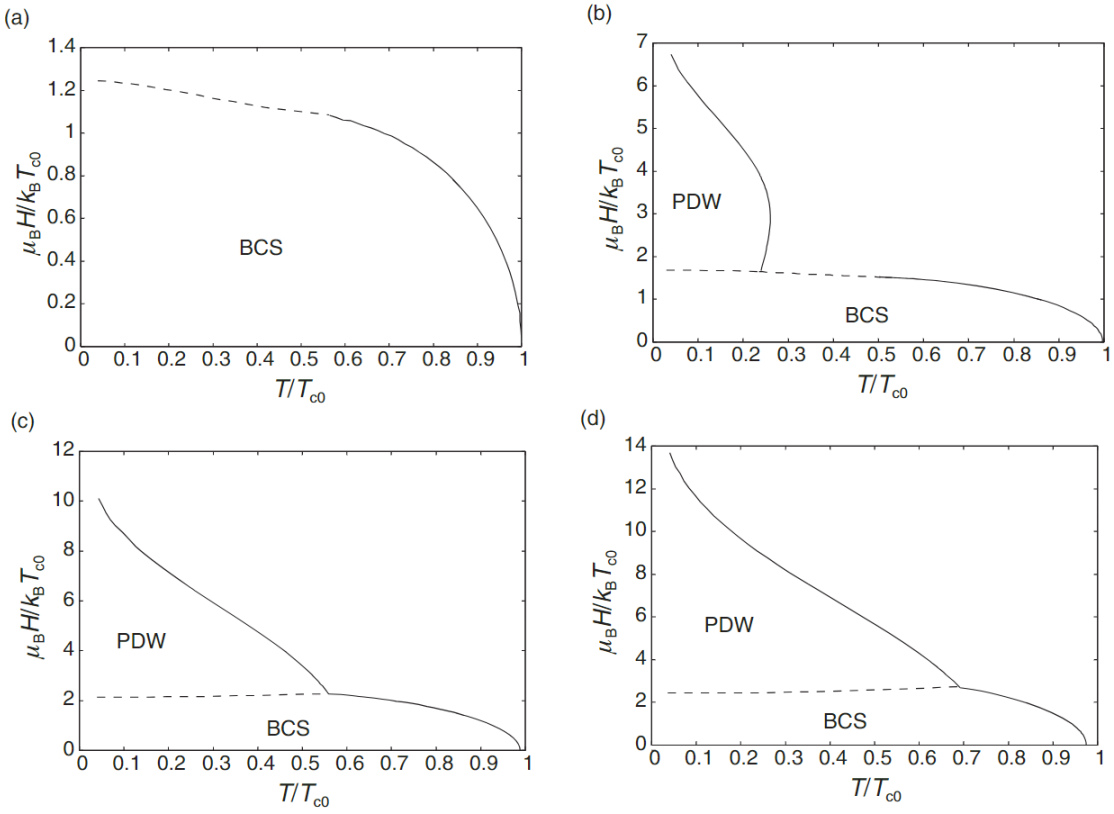

Figure 1.1: The phase diagrams for the bilayer superconductor for (a) $\alpha/t_\perp = 0$ (b) $\alpha/t_\perp = 1$ (c) $\alpha/t_\perp = 2$ (d) $\alpha/t_\perp = 3$, respectively. This figure was taken from Ref. [1]. Reprinted figure with permission from Ref. [1] © 2012 by the American Physical Society.

breaking, which leads to momentum-dependent spin-splitting and a variety of rich phenomena, local inversion symmetry breaking in these materials induces a non-trivial spin structure within the degenerate Kramers doublets. This unique spin structure facilitates the formation of sublattice-antisymmetric Cooper pairs. With the application of a magnetic field, the odd-parity superconducting state emerges as the most stable configuration. In the $H - T$ phase diagram of these systems, a phase transition could be observed from an even-parity state to an odd-parity state [Fig. 1.1]. This transition underscores the complex interplay between local structural asymmetry and superconductivity.

1.2 The overview on experimental observations

A decade has passed since the proposition of odd-parity superconductivity in crystals with locally broken inversion symmetry. During this period, the multiple superconducting phase dia-

gram has been observed in the locally non-centrosymmetric heavy-fermion system $CeRh_2As_2$ [2]. This phase diagram is commonly interpreted as resulting from a transition between even and odd-parity states within the superconducting phase. Following the discovery of $CeRh_2As_2$, extensive experimental efforts have been conducted, leading to the observation of several unfamiliar physical properties. Some of these findings present theoretical challenges that remain unresolved. In this section, we aim to summarize all known experimental results related to $CeRh_2As_2$ up to the time of writing this thesis.

1.2.1 Discovery of $CeRh_2As_2$ (Ref. [2])

In 2021, the discovery of the locally-noncentrosymmetric heavy-fermion superconductor $CeRh_2As_2$ has shed light on the importance of the crystalline structure of superconductor and their implications. [2]. In this compound, the two-phase superconducting state was observed in the *H-T* phase diagram. There is a kinked structure in the critical field curve in the phase diagram that indicates the phase transition between one superconducting phase into another superconducting phase 1.2(b). A similar kink structure was proposed in theoretical work on locally noncentrosymmetric superconductors [1]. This theory revealed that the application of the external magnetic field causes the phase transition from even- to odd-parity superconductivity. The realized odd-parity superconducting phase in the high-magnetic phase has the unusual Cooper pairing potential in which their sign changes depending on layers. Indeed, in $CeRh_2As_2$, the inversion symmetry is locally broken at Ce sites, while the inversion symmetry is globally preserved 1.2(a). These crystalline structures introduce sublattice degrees of freedom into electrons forming Cooper pairs. Therefore, odd-parity superconductivity in $CeRh_2As_2$ is intrinsic to a local non-centrosymmetric crystalline structure.

While a basic mean-field analysis using a two-sublattice model sheds light on key properties of $CeRh_2As_2$, several enigmatic aspects remain unresolved. Notably, specific heat measurements have indicated non-Fermi liquid behavior, diverging from conventional spin-fluctuation theory. This suggests the presence of non-magnetic quantum critical fluctuations in $CeRh_2As_2$. The nature of the compound's ground state also remains elusive. Crystal field analysis predicts that the energy gap between the ground state and the first excited state is approximately 30 K, coincidentally similar to the Kondo temperature (30-40 K), indicative of heavy-electron behavior. This overlap between crystal field levels and the Kondo temperature implies that the many-body ground state of $CeRh_2As_2$ might possess a multi-orbital character, being a hybrid of the ground state and first excited state of the crystal field, intricately intermixed via the Kondo effect. This scenario accounts for the quadrupole degrees of freedom in the electrons at the Fermi surface, potentially explaining the 'hidden order' observed in $CeRh_2As_2$. Renormalized band calculations have revealed Fermi surfaces with varying quadrupole moment expectations. Nesting between these Fermi surfaces could trigger a quadrupole density wave state. However, charge degrees of freedom are typically

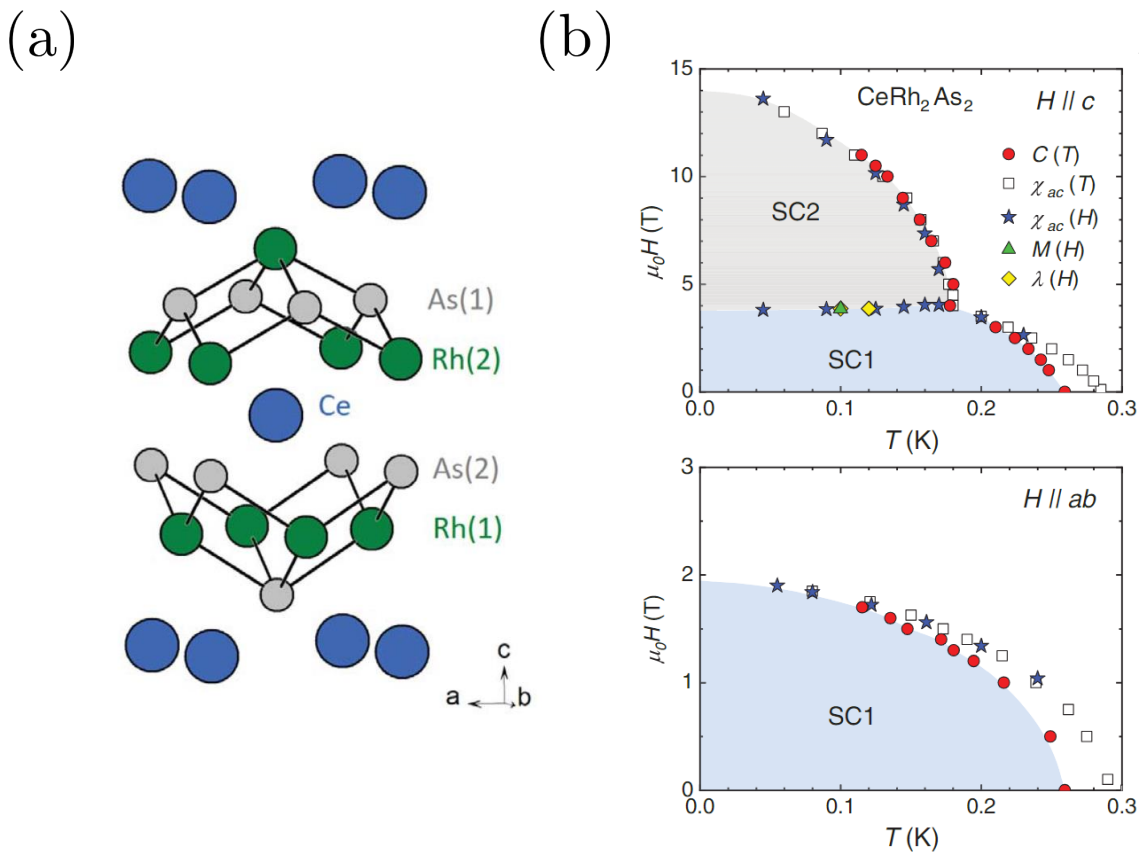

Figure 1.2: (a) Crystal structure of $CeRh_2As_2$. (b) Experimentally determined phase diagram of $CeRh_2As_2$. The transition line was determined by specific heat, magnetic susceptibility, Magnetization, and Magnetostriction measurements. From Ref. [2]. Reprinted with permission from AAAS.

suppressed by Coulomb correlation effects in such systems, pointing towards the need for further investigation to fully comprehend the origin of the quadrupole density wave state in $CeRh_2As_2$

1.2.2 Optical conductivity (Ref. [3])

Optical conductivity measurements provide insights into band dispersion above the Fermi level, E_F. In most cerium compounds, where Ce^{+3} ions adopt an f^1 configuration, the flat bands originating from f-orbitals are typically unoccupied. Therefore, the optical conductivity measurements reflect the optical transition probabilities, $|4f^n c^m\rangle + \hbar\omega \rightarrow |4f^{n+1}c^{m-1}\rangle$ [4]. As a result, optical conductivity measurements are crucial for understanding the low-energy structure of single-particle excitations. Kimura *et al.* have reported such measurement, highlighting inconsistencies between experimental observations and theoretical predictions based on density functional theory as shown in Fig. 1.3 [3]. This result suggests that strong-correlation effects plays an essential role in single-particle excitations. In contrast, for compounds with the $ThCr_2Si_2$-type crystal structure, which is the locally-centrosymmetric counterpart, there are reported agreements between theory and experiment [4, 5, 6]. The reasons for these discrepancies remain unclear, but they may be attributed to the strong c-f hybridization effects associated with the Kondo effect which is not taken into account in density functional theory. The reasons for the discrepancies observed in other structures remain unclear, but they may be related to strong c-f hybridization effects, characteristic of the Kondo effect, which is not adequately captured by density functional theory. Moreover, they also observed a trend of an enhanced density of states at the Fermi level, $D(E_F)$, in the $CaCe_2Ge_2$-type crystal structure compared to the $ThCr_2Si_2$-type structure.

1.2.3 Thermodynamic measurements (Ref [7, 8, 9, 10, 11, 12, 13])

To confirm the presence of a bulk phase transition, observations of thermodynamic quantities are essential. In $CeRh_2As_2$, two distinct phenomena are observed: two superconducting phases at T_{sc} and an unconventional hidden ordered phase at T_0. Precise measurements of thermodynamic quantities are also crucial for determining the order of these phase transitions. Hafner *et al.* have performed specific heat, thermal expansion coefficients, and Grüneisen parameter measurements [7]. Utilizing the Ehrenfest relation, they determined the pressure dependence of T_0 to be $dT_0/dp = 1.5\,\mathrm{K/GPa}$. This result suggests that the unconventional order at T_0 differs from the antiferromagnetic order in typical Kondo lattice systems. Analysis of the Grüneisen parameter indicated that $4f$ hybridization stabilizes the order at T_0. Furthermore, the authors explored the magnetic field dependence of anomalies in thermodynamic quantities. Under in-plane magnetic fields, the transition temperature T_0 increases. Remarkably, around $H_\perp \sim 9\,\mathrm{T}$, a phase transition from the order at T_0 (phase I) to

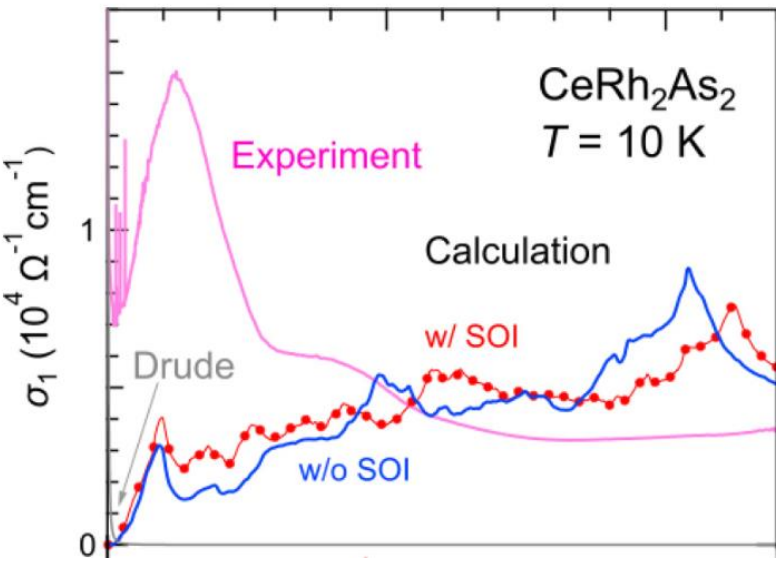

Figure 1.3: The measured optical conductivity in magenta, alongside the theoretical results in blue (without spin-orbit interaction) and red (with spin-orbit interaction). Reprinted figure with permission from Ref. [3] © 2021 by the American Physical Society.

another unconventional order (phase II) was observed, as shown in Fig. 1.4. Measurements of magnetostriction coefficient, resistivity, field derivative of magnetization, and torque revealed clear hysteresis. The absence of anomalies in AC susceptibility and magnetization rules out magnetic order, leading to the proposal of quadrupole order as the order parameter at T_0. In $CeRh_2As_2$, the Ce atom's C_{4v} site symmetry results in CEF splitting from $j = 5/2$ multiplets into three Kramers doublets. Naively, one might not expect quadrupole degrees of freedom in a heavy fermion system. However, the energy difference between the ground state and the first excited state is comparable to the Kondo temperature in this system. The simple Anderson impurity model, solved via non-crossing approximation, shows significant changes in quadrupole moments. In renormalized calculations, the expectation value of the quadrupole moment $\langle n\boldsymbol{k}|3J_z^2 - \boldsymbol{J}^2|n\boldsymbol{k}\rangle$ exhibits different values on different Fermi surfaces [14]. Furthermore, the nesting property between Fermi surfaces with different quadrupole moments suggests a quadrupolar density wave phase at T_0.

Determining the angle at which the high-magnetic odd-parity SC2 phase vanishes is crucial, as the field-angle dependence of the upper critical field provides insights into the microscopic state. Landaeta *et al.* conducted ac susceptibility, magnetic torque, and specific heat measurements across various magnetic field directions [Fig.1.5(a)] [8]. Their comprehensive study confirmed that the SC2 phase is rapidly suppressed around 35°. Additionally, they observed that $H_{\rm cr}$, which delineates phase I from phase II, is enhanced when the magnetic field

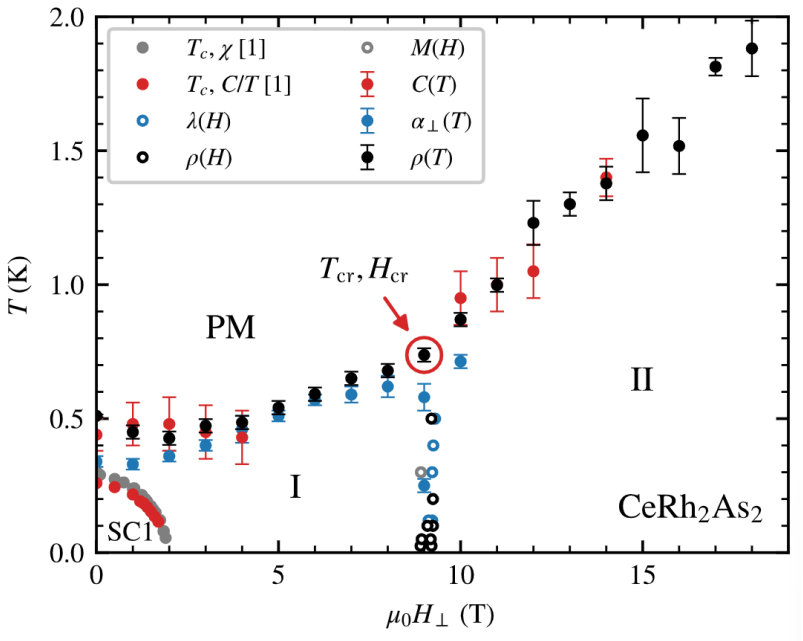

Figure 1.4: The phase diagram for the in-plane magnetic field. At $H_{cr} \sim 9\,\mathrm{K}$, the phase transition from phase I into phase II is indicated. From Ref. [7] © 2022 D. Hafner, P. Khanenko, E.-O. Eljaouhari, R. Küchler, J. Banda, N. Bannor, T. Lühmann, J. F. Landaeta, S. Mishra, I. Sheikin, E. Hassinger, S. Khim, C. Geibel, G. Zwicknagl, and M. Brando

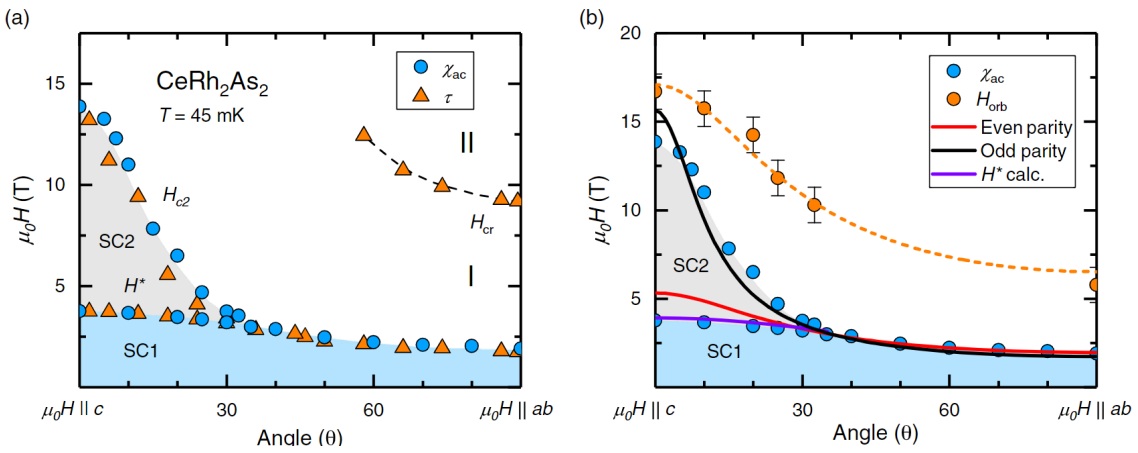

Figure 1.5: The phase diagram of the field-angle dependence of the superconducting phase transition and the unusual T_0 order. From Ref. [8] © 2022 J. F. Landaeta, P. Khanenko, D. C. Cavanagh, C. Geibel, S. Khim, S. Mishra, I. Sheikin, P. M. R. Brydon, D. F. Agterberg, M. Brando, and E. Hassinger.

is tilted [Fig. 1.5(a)]. To elucidate the source of the anisotropy in the superconducting phase diagram, they evaluated the angle dependence of the orbital limit, $H_{\rm orb}$. The experimental data was fitted using the theoretical formula:

$$H_{c2}(\theta) = \frac{H_{c2}^{c}}{\sqrt{\Gamma^2 \sin^2\theta + \cos^2\theta}} \tag{1.2.1}$$

where Γ represents the anisotropy parameter. Assuming $v_{\rm F}/m^*$, they deduced that $m_a^*/m_c^* = 2.6$. Moreover, by incorporating both orbital and Pauli limiting effects into the analysis, they found that $H_{\rm P}/g_\theta$ exhibits angular dependence similar to $H_{c2}(\theta)$ [Fig. 1.5(b)]. Further, they investigated the angle dependence of the upper critical field of the SC2 state. They concluded that the anisotropy of the SC2 phase stems from the in-plane alignment of the d-vector in the pseud-spin basis. Unlike other spin-triplet superconductors, where the anisotropy of the d-vector is obscured by orbital depairing effects and quantum criticality, $CeRh_2As_2$ appears to be the first example demonstrating the intrinsic anisotropy of spin-triplet superconductors.

The dimensionality of the electronic structure in $CeRh_2As_2$ is a crucial factor for understanding its multiple superconducting phase diagrams. A two-dimensional Fermi surface is conducive to a sublattice anti-symmetric odd-parity superconducting state. The anisotropy observed in electronic resistivity offers insights into the dimensionality of the electronic states in such compounds. Mishra *et al.* conducted electronic resistivity measurements in both in-plane and out-of-plane directions [9]. Their results show that the in-plane electronic resistivity $\rho_a(T)$ is approximately three-fourths the value of the out-of-plane resistivity $\rho_c(T)$

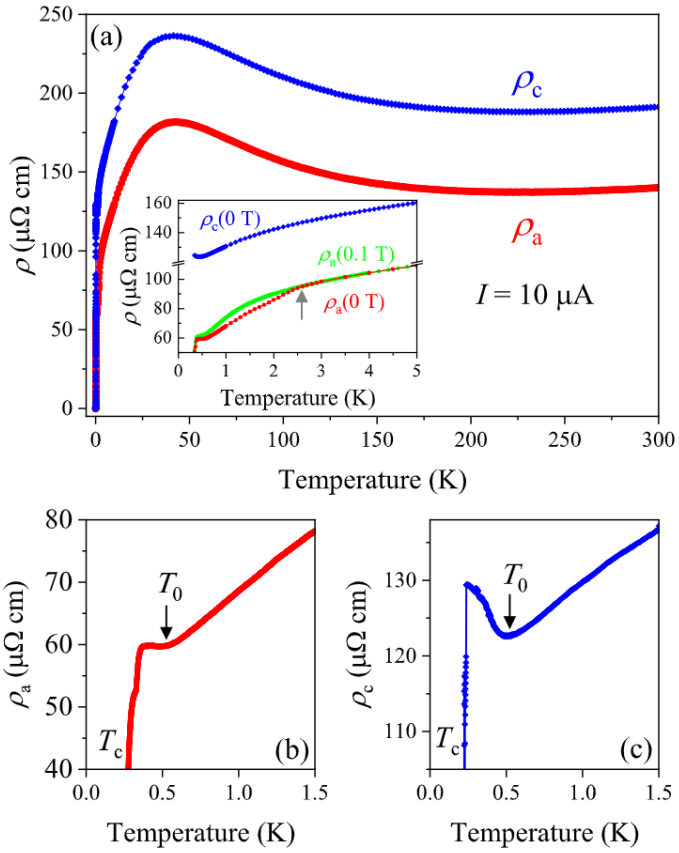

Figure 1.6: (a) Resistivities ρ_a and ρ_c. The inset shows the resistivities $\rho_a(0T)$, $\rho_a(0.1T)$, and $\rho_c(0T)$. (b-c) shows a zoomed-in view of the low-temperature resistivities ρ_a and ρ_c. Reprinted figure with permission from Ref. [9] © 2022 by the American Physical Society.

[Fig. 1.6]. This finding indicates that $CeRh_2As_2$ possesses a mildly anisotropic electronic structure. Moreover, the out-of-plane measurements reveal a distinct hump at the T_0 order. This observation suggests that the $\boldsymbol{q}$-vector of the QDW phase includes a significant z component, potentially leading to the opening of a gap along the c-axis.

The unidentified order at T_0 presents an alternative explanation for the superconducting multiple-phase diagram of $CeRh_2As_2$. Specifically, it suggests that the transition line of the T_0 order intersects with the bicritical point, where $T_c(H)$ and $H^*(T)$ merge. From a thermodynamic perspective, determining whether this point is a bicritical or tetracritical point is crucial, as it defines the nature of the transition lines. Semeniuk *et al.* [10] conducted detailed measurements on the $H-T$ phase diagram of $CeRh_2As_2$, focusing on heat capacity and electrical resistivity. In earlier studies, the inhomogeneity of the sample obscured the transition of the T_0 order, masked by the superconducting transition. However, in their study, the sample quality is significantly improved, raising the superconducting transition

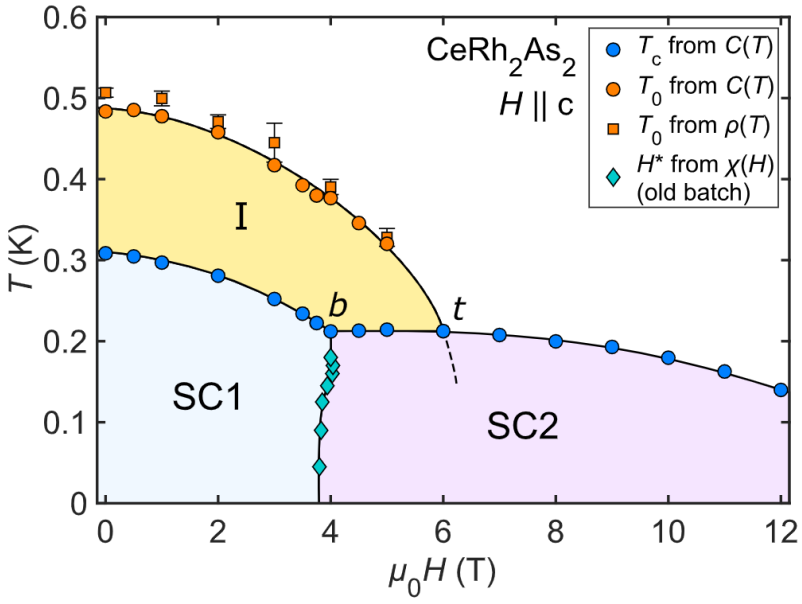

Figure 1.7: The $H-T$ phase diagram for the refined new samples. The transition line for T_0 order does not merge to the bicritical point. From Ref. [10] © 2023 K. Semeniuk, D. Hafner, P. Khanenko, T. Lühmann, J. Banda, J. F. Landaeta, C. Geibel, S. Khim, E. Hassinger, and M. Brando.

temperature to $0.31\,\mathrm{K}$. This enhancement in sample quality allowed both the superconducting transition and the T_0 transition to be distinctly observed in the heat capacity data, enabling a refinement of the phase diagram. The refined phase diagram, as shown in Fig. 1.7, clearly indicates that the T_0 transition does not intersect with the point where transitions within the superconducting state occur. This observation provides valuable insights into the complex superconducting behavior of $CeRh_2As_2$.

Applying pressure influences the electronic structure of the system, in particular, the heavy-fermion systems have a renormalized small energy scale and the duality of f-electrons is controlled by the pressure. In $CeRh_2As_2$, f-electron is thought to be itinerant. Siddiquee *et al.* have conducted the resistivity measurements under pressure [11]. The authors determined the phase diagram under pressure and found that odd-parity superconductivity is suppressed faster than the even-parity superconducting phase [Fig. 1.8]. Firstly, the transition temperature decreases by pressure until 2.5 GPa. Above 2.5 GPa, the transition temperature turns out to be enhanced. From data of resistivity, they would rule out the possibility of the valence fluctuation.

Separate studies by Pfeiffer *et al.* have shed light on the behavior of $CeRh_2As_2$ under high-pressure conditions, as detailed in their recent preprints [12, 13]. These studies primarily focused on resistivity measurements and their implications for the material's electronic

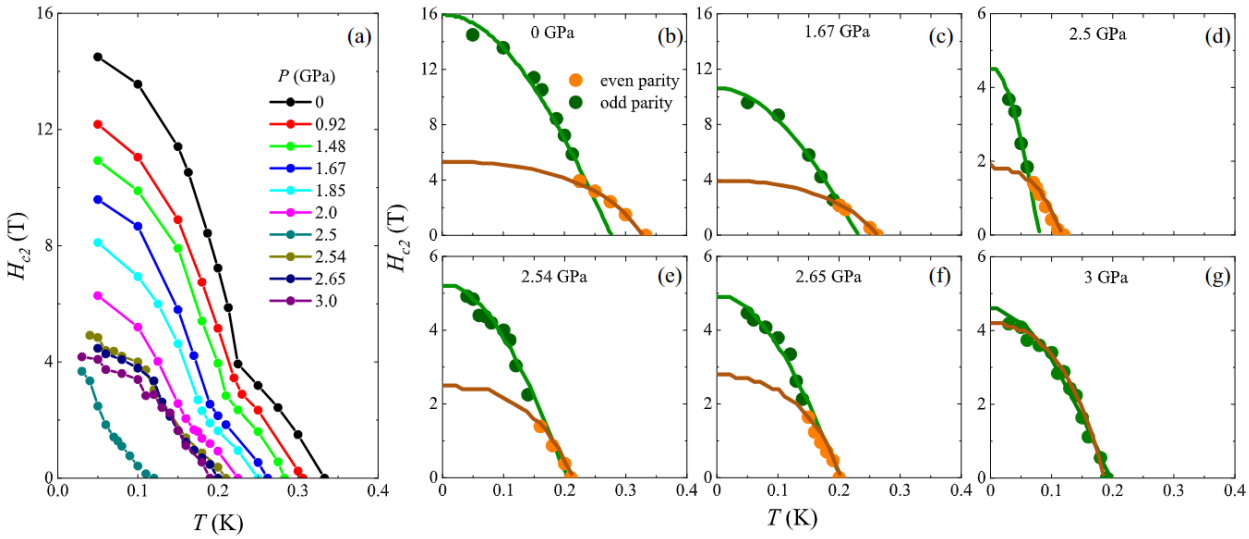

Figure 1.8: (a) The temperature-magnetic field phase diagrams for various pressure. (b)-(g) Theoretical fitting of even- and odd- superconducting states. From Ref. [11] © 2023 by the American Physical Society.

properties. Initially, the authors measured the temperature dependence of electrical resistivity under high pressure [12]. At ambient pressure, $CeRh_2As_2$ exhibits non-Fermi liquid behavior, characterized by a resistivity proportional to $T^{0.5}$. Intriguingly, the material enters a superconducting state before any transition to Fermi-liquid behavior occurs. However, when a pressure of $2.7, \mathrm{GPa}$ is applied, Fermi-liquid behavior ($\rho(T) \sim T^2$) is observed, indicating that the applied pressure drives the system away from its quantum critical point [Fig. 1.9(left a)]. Additionally, the study explores the pressure dependence of a hidden ordering temperature, T_0. It was discovered that the hidden order is completely suppressed at around $0.5\,\mathrm{GPa}$. This observation suggests that the conceptual phase diagram of $CeRh_2As_2$ aligns with other cerium-based heavy-fermion systems, where superconductivity is typically located near the quantum critical point. Notably, the superconducting 'dome' in $CeRh_2As_2$ is larger compared to other heavy-fermion systems, a phenomenon whose origin remains unclear. Furthermore, Pfeiffer *et al.* investigated the pressure dependence of the superconducting phase diagram [13]. Their results indicated a decrease in the parity transition field, suggesting a degeneracy in the transition temperatures of even- and odd-parity superconducting states [Fig. 1.9(right a)]. Initially, the interplay between the hidden order and the multiple superconducting phase diagram in $CeRh_2As_2$ garnered significant interest. Although the quantum critical point for the hidden order is located at $0.5\,\mathrm{GPa}$, the distinct multiple-phase diagram persists up to $2.67\,\mathrm{GPa}$. This persistence implies that the nature of the hidden order may not be directly related to the multiple superconducting phase transitions observed

in $CeRh_2As_2$.

1.2.4 NMR/NQR (Ref. [15, 16, 17])

Nuclear magnetic/quadrupole resonance measurements are crucial for gaining microscopic insights into the spin-state of heavy fermions near the Fermi level, E_F. Generally, unconventional superconductivity in heavy-fermion systems is driven by magnetic fluctuations, with some systems even exhibiting coexisting magnetic order and superconductivity. Understanding the nature of these magnetic states is thus key to comprehending superconductivity. Kibune *et al.* conducted ^{75}As nuclear quadrupole resonance measurements on $CeRh_2As_2$ and observed a mysterious broadening in the NQR spectra below $T_N = 0.25\,\mathrm{K}$[15]. Notably, while the As(2) NQR spectra broadened below T_N, the As(1) spectra remained unaffected. This broadening is believed to be a manifestation of anti-ferromagnetic order within the superconducting state. Utilizing the classical dipole model, the authors proposed the presence of A-type AFM (in-plane ferromagnetic and inter-plane antiferromagnetic) order with magnetic moments aligned parallel to the c-axis or a helical order with in-plane moments [Fig.1.10]. The former suggests an intriguing ferroic odd-parity magnetic multipole order. $CeRh_2As_2$ stands out as the only known material that exhibits magnetic order within the superconducting phase, where $T_N < T_c$. This contrasts with other cerium-based superconductors, where magnetic order typically appears at temperatures higher than the superconducting transition temperature. To further substantiate the presence of AFM order coexisting with superconductivity, comprehensive thermodynamic measurements are eagerly anticipated.

Kitagawa *et al.* have conducted ^{75}As nuclear magnetic resonance studies. Initially, they observed temperature variations in the Knight shift. Notably, while the Knight shift parallel to the c-axis exhibited a broad maximum at $3\,K$, the shift perpendicular to the c-axis continued to increase. These observations suggest that $CeRh_2As_2$ possesses XY-type magnetic anisotropy, a characteristic typically observed in cerium-based superconductors. The authors also measured the spin-lattice relaxation time, $1/T_1$, and found that it reaches a constant value, as shown in Fig. 1.11(a-b). According to the self-consistent renormalization theory, a widely accepted phenomenological theory for quantum critical fluctuations, such constant behavior of $1/T_1$ can be attributed to the two-dimensional nature of the magnetic fluctuations. This finding is particularly notable, as heavy-fermion superconductors usually exhibit three-dimensional magnetic fluctuations. Further, their observations of $1/T_1T$, which reflects fluctuating hyperfine fields, show distinctive behaviors. While $1/T_1T$ parallel to the c-axis displays a broad maximum at $3\,K$, the measurement perpendicular to the c-axis shows a continuous increase [Fig. 1.11(c)]. This again points to XY-type anisotropic magnetic fluctuations.

The parity of the Cooper pair significantly impacts the spin response in a superconducting system. In an even-parity spin-singlet superconductor, the spin susceptibility decreases

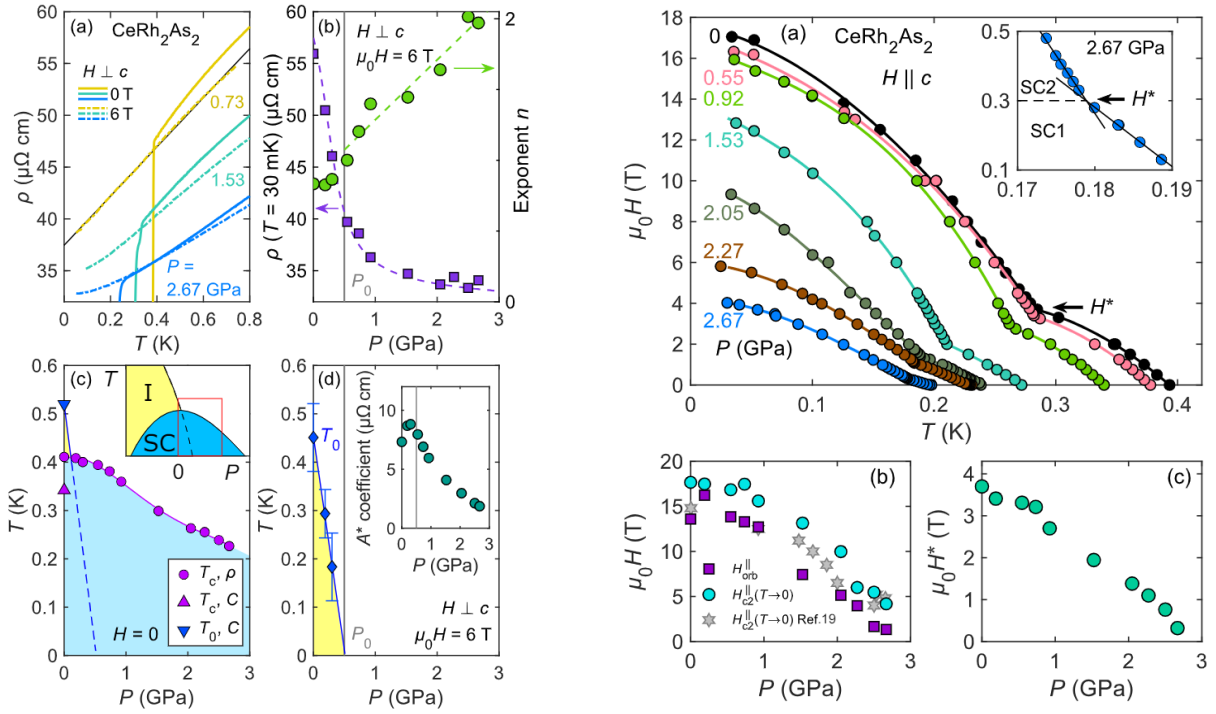

Figure 1.9: (left) The investigation into resistivity ρ against temperature T at selected pressures is outlined. Notably, the curvature of $\rho(T)$ increases with pressure. Additionally, the pressure dependence of ρ at 30 mK and the power-law exponent n for a 0.1-0.3 K temperature interval are presented, with magnetic field applied. This exponent was obtained from fitting the data with a power-law function, $\rho(T) = \rho_0 + A^*(T/T_{\mathrm{ref}})^n$, where ρ_0 and A^* are constants and $T_{\mathrm{ref}} = 0.3\,\mathrm{K}$. The zero-field phase diagram (c) Data from heat capacity measurements, represented by triangular markers. An inset provides a schematic of a possible broader phase diagram, highlighting the pressure-temperature range explored in this study. Phase diagram (d) for a 6 T in-plane field is also presented, including the pressure dependence of the A^* coefficient of the power-law function. (right) the focus shifts to superconductivity in $CeRh_2As_2$ under pressure in an out-of-plane magnetic field ($H \parallel c$). Field-temperature ($\mu_0 H$-T) phase diagrams show transitions between two superconducting phases, SC1 and SC2, at a magnetic field H^*, identifiable as a kink in the critical field curves, as marked for $P = 0$. An inset at 2.67 GPa illustrates the continuation of the SC1-SC2 transition. The pressure dependence of the orbital-limiting upper critical field ($H^{\parallel}_{\mathrm{orb}}$), estimated from the slopes of $H_{c2}(T)$ curves at T_c, and the zero-temperature limit of the upper critical field $H^{\parallel}_{c2}$ are compared with data from an independent study. Lastly, the pressure dependence of the phase switching field H^* is detailed. Left figure is from Ref. [12] © 2023 M. Pfeiffer, K. Semeniuk, J. F. Landaeta, R. Borth, C. Geibel, M. Nicklas, M. Brando, S. Khim, E. Hassinger. Right figure is from Ref. [13] © 2023 M. Pfeiffer, K. Semeniuk, J. F. Landaeta, M. Nicklas, C. Geibel, M. Brando, S. Khim, E. Hassinger

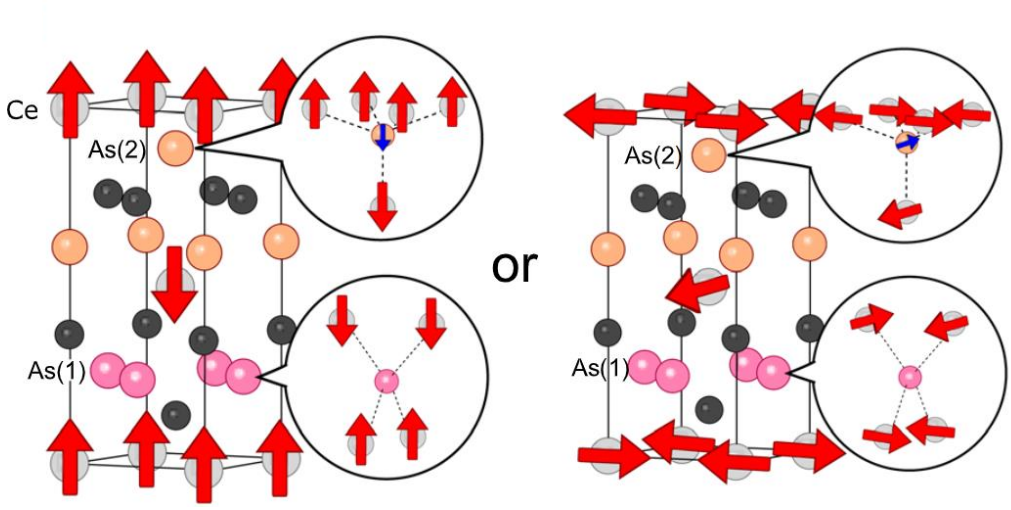

Figure 1.10: (Left) The magnetic structure of in-plane ferromagnetic and inter-plane antiferromagnetic order. (Right) The magnetic structure of a helical order with in-plane moment. Reprinted figure with permission from Ref. [15] © 2022 by the American Physical Society.

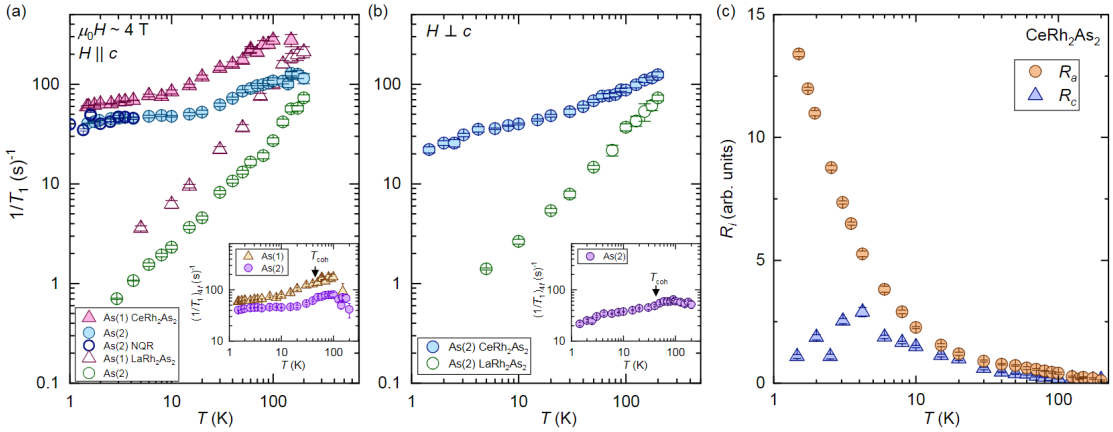

Figure 1.11: Temperature dependence of $1/T_1$ for (a) $H||c$ and (b) $H \perp c$ in $CeRh_2As_2$ $LaRh_2As_2$. (c) Temperature dependence of R_a and R_c at As(2) site in $CeRh_2As_2$. From Ref. [16] © 2022 Shunsaku Kitagawa, Mayu Kibune, Katsuki Kinjo, Masahiro Manago, Takanori Taniguchi, Kenji Ishida, Manuel Brando, Elena Hassinger, Christoph Geibel, and Seunghyun Khim.

following the superconducting phase transition. However, in an odd-parity spin-triplet superconductor, spin susceptibility persists in directions perpendicular to the d-vector. Consequently, a detailed study of spin susceptibility is crucial for understanding the microscopic nature of superconductivity. Ogata *et al.* have performed nuclear magnetic resonance measurements in a high magnetic field environment [17]. Initially, they observed the Knight shift from low to high fields and noted that the spin susceptibility in the SC2 phase decreases, contradicting theoretical predictions [Fig. 1.12(b)]. If the SC2 phase were a modulated odd-parity phase, the spin susceptibility along the c-axis should remain unchanged [18], raising questions yet to be answered. Furthermore, using the standard expression for estimating the Pauli limiting field,

$$\frac{1}{2}\delta\chi\mu_0 H_{\mathrm{P}}^2 = \frac{1}{2}\mu_0 H_c^2, \tag{1.2.2}$$

where H_c is the thermodynamic critical field, they estimated it to be 3.4 T in the SC1 phase, aligning well with the parity transition field between the SC1 and SC2 phases. Applying the same method to the SC2 phase, they estimated a Pauli limiting field of 4.8 T, which starkly contrasts with the observed critical field of 14 T. In $CeRh_2As_2$, the spin susceptibility decreases in the SC2 phase, yet the Pauli limiting effect seems inactive, indicating an unusual superconductivity nature. The authors suggest that these conflicting observations may be due to the inhomogeneity of superconductivity in the SC2 phase. In this phase, the phase of superconducting order parameter oscillates between layers. Since measurements were taken at the As site, the spin susceptibility at the As site might decrease while that at the Ce sites remains unaffected [Fig. 1.12(c) inset]. In the band basis, these significant decreases in spin susceptibility could manifest as Van Vleck susceptibility, which does not largely affect superconductivity.

1.2.5 Thermal conductivity (Ref. [19])

Thermal conductivity measurements are pivotal in determining the structure of the gap function in superconductivity. While Cooper pairs do not transport heat, Bogoliubov quasiparticles act as heat carriers. Therefore, these measurements offer insights into the shape and position of the node structure, shedding light on the microscopic details of superconducting order parameters. Onishi *et al.* conducted thermal transport measurements on $CeRh_2As_2$ [19]. By assuming the Wiedemann-Franz law, they analyzed the temperature dependence of the phononic thermal conductivity, $\kappa_{\mathrm{ph}}(T)$. Their findings indicate a near T-linear temperature dependence, $\kappa\mathrm{ph}(T) = T^{1.24}$, deviating from the expected $\kappa_{\mathrm{ph}}(T) = T^3$ behavior [Fig. 1.13(A)]. Such quasi-linear-in-T behaviors have also been observed in other Ce-based heavy-fermion compounds [20, 21]. The underlying origin of this deviation remains an open question for future theoretical research. Furthermore, they investigated the validity of the Wiedemann-Franz law in their experiments. Their results confirmed the law's applicability within the precision of the experiments, although a small deviation could not

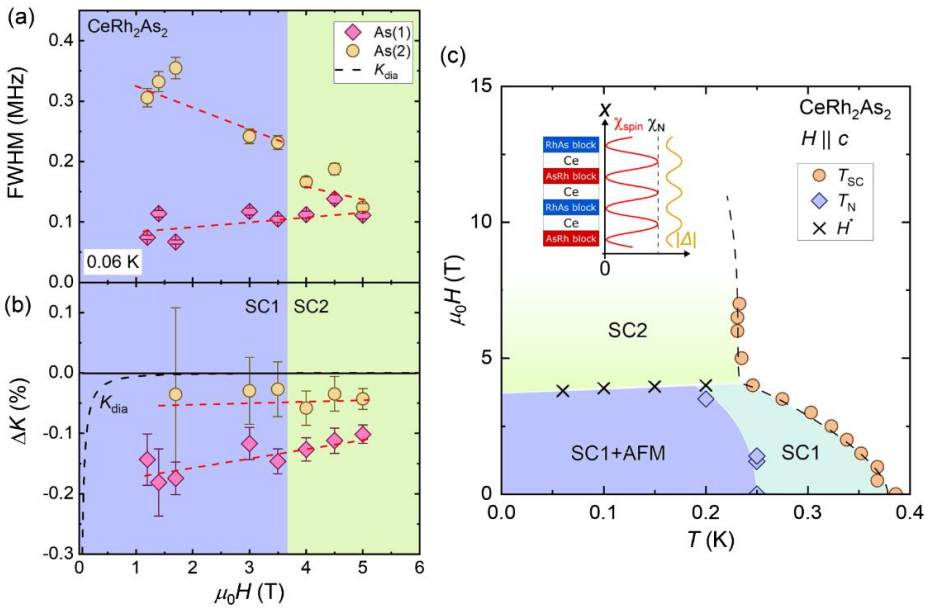

Figure 1.12: (Left) The magnetic structure of in-plane ferromagnetic and inter-plane antiferromagnetic order. (Right) The magnetic structure of a helical order with in-plane moment. Reprinted figure with permission from Ref. [17] © 2023 by the American Physical Society.

be completely ruled out [Fig. 1.13(B)]. Lastly, they explored the field dependence of thermal transport measurements to identify the node structure. However, due to impurities in the sample, they were unable to conclusively observe evidence of the node structure in the superconductivity of $CeRh_2As_2$.

1.2.6 Spectroscopic measurements (Ref. [22])

Spectroscopic measurements are pivotal for probing the wave function of a system, as they adhere to the selection rules governed by the light-matter coupling matrix element. In $CeRh_2As_2$, the Kondo effect leads to a complex admixture of localized f-electron and conduction electron wave functions, resulting in a non-trivial ground state. This complexity has been hinted at through magnetic entropy measurements and renormalized band calculations, suggesting a multi-orbital nature of the ground state [7]. Thus, a comprehensive study of the wave function at low temperatures using spectroscopic techniques is essential. Christovam *et al.* conducted Core-level photoelectron spectroscopy with hard x-rays (HAXPES), x-ray absorption spectroscopy (XAS), and non-resonant inelastic x-ray scattering (NIXS) measurements. The HAXPES and XAS measurements revealed a faint signal from the f^0 configuration, implying that the carrier density of f-electrons, n_f, is less than 1. Additionally, the temperature dependence of the linear dichroism, LD(T), exhibited characteristics

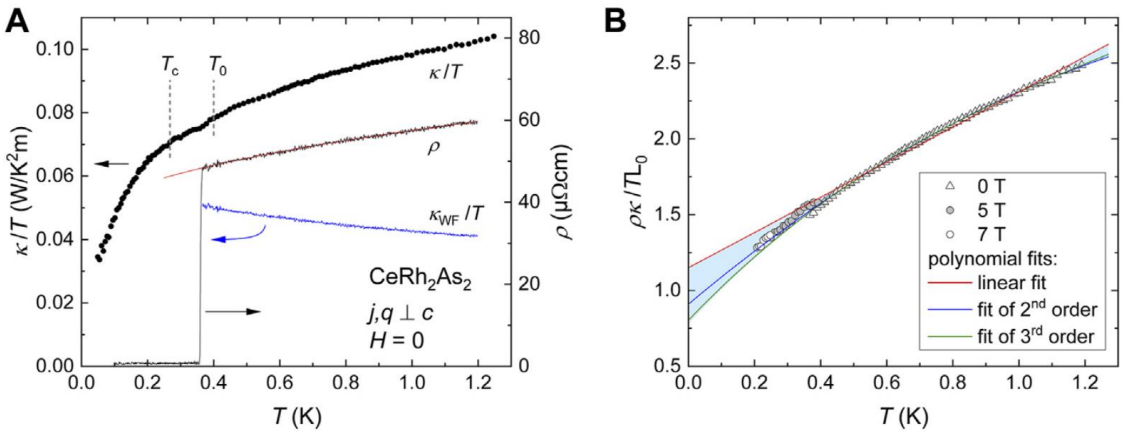

Figure 1.13: (A) The temperature dependence of the thermal conductivity of the compound. The electric resistivity is also shown. (B) The temperature dependence of the Lorenz ratio. From Ref. [19] © 2022 Onishi, Stockert, Khim, Banda, Brando and Hassinger.

unique to heavy-fermion systems. While the behavior between 50, K and 200, K aligned with simulations assuming a simple localized model, significant deviations at 3, K indicated the influence of the Kondo effect on $CeRh_2As_2$'s electronic structure [Fig 1.14(a-b)]. Analysis using a simplified Anderson impurity model with the non-crossing approximation could replicate this temperature dependency, underscoring the importance of hybridization due to the Kondo effect [Fig 1.14(c)]. To ascertain the shape of the wave function, NIXS measurements were performed, leading to the conclusion that the ground state wave function exhibits anisotropy aligned along the (110) direction. Ultimately, the ground state wave function was identified as a linear combination of crystalline field levels, expressed as:

$$\sqrt{0.58}\,|\Gamma_7^-\rangle\,, \quad \sqrt{0.29}\,|\Gamma_6\rangle\,, \quad \sqrt{0.08}\,|\Gamma_7^+\rangle\,. \tag{1.2.3}$$

This discovery provides a deeper understanding of the ground state properties in $CeRh_2As_2$.

1.2.7 Angle-resolved photoemission spectroscopy (Ref. [23, 24])

Angle-resolved photoemission spectroscopy (ARPES) measurements are crucial for revealing the spectral features of single-particle fermionic excitations in superconductors, providing a basis for comparison with electronic structure calculations. In strongly correlated electron systems like $CeRh_2As_2$, the nature of superconductivity is highly sensitive to the position of the van Hope singularity and the Fermi surface's shape. Thus, accurately determining the electronic structure and the shape of the Fermi surface is essential for understanding the multiple superconducting phase diagrams. Chen *et al.* and Wu *et al.* have performed

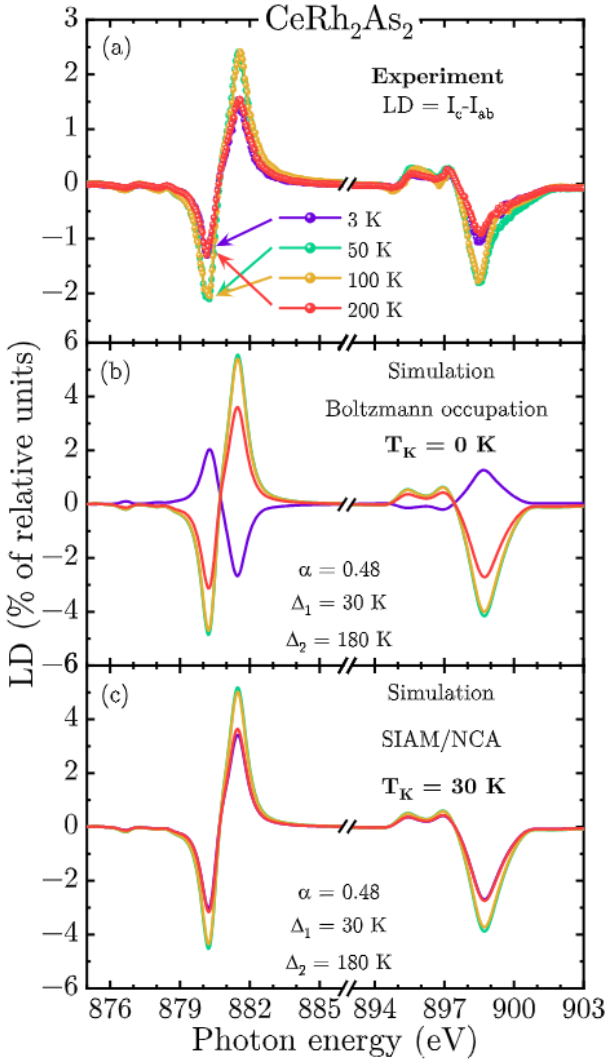

Figure 1.14: (a) The measured temperature dependence (T-dependence) of the Linear Dichroism (LD) is shown at various temperatures: 3 K (purple), 50 K (green), 100 K (yellow), and 200 K (red). The lower panels display two distinct simulations: (b) an ionic crystal-field calculation that considers the Boltzmann occupation of excited states but excludes the Kondo effect, and (c) the same crystal-field model that incorporates the Kondo effect, as detailed in the text. To enhance visibility, the scale of the LD has been multiplied by 100, representing the percentage of LD. From Ref. [22] © 2023 Denise S. Christovam, Miguel Ferreira-Carvalho, Andrea Marino, Martin Sundermann, Daisuke Takegami, Anna Melendez-Sans, Ku Ding Tsuei, Zhiwei Hu, Sahana Roessler, Manuel Valvidares, Maurits W. Haverkort, Yu Liu, Eric D. Bauer, Liu Hao Tjeng, Gertrud Zwicknagl, Andrea Severing.

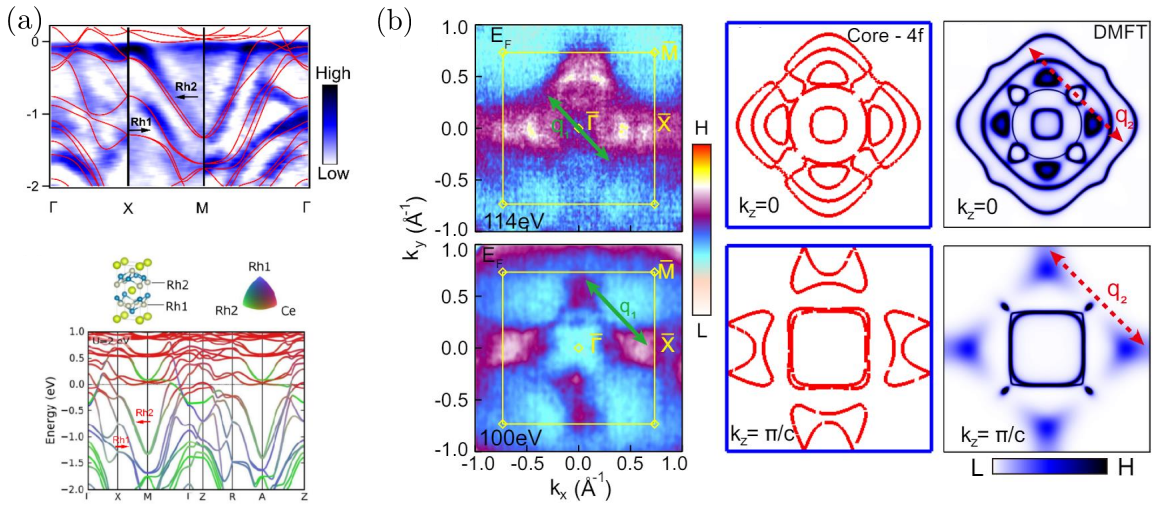

Figure 1.15: (a) (upper panel) The spectral weight of ARPES measurements with DFT+U calculation. (lower panel) The calculated band dispersion with orbital character weight. (b) (left low) The experimentally determined Fermi suerface (middle low) The Fermi surface of DFT calculation in which f-electron is treated as the core state. (right low) The Fermi surface of DFT+DMFT calculation. The nesting vectors are shown respectively. The figure (a) is from Ref. [23] © 2023 Xuezhi Chen, Le Wang, Jun Ishizuka, Kosuke Nogaki, Yiwei Cheng, Fazhi Yang, Renjie Zhang, Zhenhua Chen, Fangyuan Zhu, Youichi Yanase, Baiqing Lv, Yaobo Huang. The figure (b) is from Ref. [24] © 2023 Yi Wu, Yongjun Zhang, Sailong Ju, Yong Hu, Yanen Huang, Yanan Zhang, Huali Zhang, Hao Zheng, Guowei Yang, Evrard-Ouicem Eljaouhari, Baopeng Song, Nicholas C. Plumb, Frank Steglich, Ming Shi, Gertrud Zwicknagl, Chao Cao, Huiqiu Yuan, Yang Liu.

ARPES measurements on $CeRh_2As_2$ [23, 24]. Both studies report that $CeRh_2As_2$ exhibits a predominantly two-dimensional electronic structure. Chen *et al.* found that their experimental results align well with DFT+U calculations, but they noted a discrepancy: the van Hove singularity is positioned closer to the Fermi energy than predicted by the calculations. This deviation could be explained by renormalization effects due to the Kondo effect. Meanwhile, Wu *et al.* also confirmed the two-dimensional nature of the Fermi surface and showed that a density functional theory combined with dynamical mean-field theory (DFT+DMFT) calculation accurately reproduces the observed Fermi surface. The electronic structure derived from DFT+DMFT closely resembles that of DFT calculations where f-electrons are treated as core states. Both studies highlight that the nesting vector at $k_z = 0$ is compatible with that at $k_z = \pi$, suggesting that $CeRh_2As_2$ possesses strong two-dimensional nesting properties. These properties likely contribute to the material's quadrupole density wave (QDW) order and its superconductivity.

1.3 Organization of this thesis

Currently, odd-parity superconductivity is widely recognized as a promising platform for realizing topological superconductivity. Developing a comprehensive formulation to confirm topological superconductivity in $CeRh_2As_2$ stands as a crucial objective within the condensed matter physics community. However, there is no topological number in the three-dimensional system without time-reversal symmetry. Notably, the phase diagram of $CeRh_2As_2$ and results from theoretical mean-field calculations exhibit qualitative inconsistencies, presenting complex theoretical problems that have yet to be resolved. Moreover, the discovery of $CeRh_2As_2$ has highlighted the critical influence of sublattice degrees of freedom in superconductivity. This is not only relevant to $CeRh_2As_2$ but extends to certain uranium- and cerium-based compounds, as well as moiré systems, all of which possess crystalline structures with sublattice degrees of freedom and exhibit magnetic field-induced superconductivity. These developments suggest that a deeper exploration of sublattice degrees of freedom could be key to unlocking new insights into the nature of superconductivity in these materials.

The structure of this thesis is organized as follows: In Chapter 2, we delve into the realm of topological crystalline superconductivity in the high-magnetic field phase of $CeRh_2As_2$. Utilizing group theoretical methods, we derive a Fermi surface formula that reveals a topological $\mathbb{Z}_2$ number, inferred from the Fermi surface's shape. Additionally, we employ density functional theory to predict the existence of Majorana surface states, which are protected by glide symmetry. Chapter 3 focuses on the results derived from a strongly correlated model. Here, we explore how antiferromagnetic fluctuations contribute to the system's robustness against external magnetic fields. We also propose a novel mechanism for field-induced superconductivity, deeply rooted in the sublattice degrees of freedom in Chapter 4. The thesis concludes with Chapter 5, where we summarize the key findings and implications of our research.

Chapter 2

Topological crystalline superconductivity in locally noncentrosymmetric $CeRh_2As_2$

For decades, the concept of symmetry breaking has been pivotal in describing various phases of quantum matter, such as magnetism, density-wave, and superconductivity, as well as critical phenomena in condensed matter physics [25]. In recent years, the burgeoning field of topological science has illuminated new facets of quantum matter, revealing phases transitions beyond the conventional framework of symmetry breaking [26, 27, 28, 29]. This includes the discovery of topological phase transitions that occur without symmetry breaking and the recognition of topological insulators and superconductors as novel and intriguing phases of matter. One particularly exotic phenomenon in topological materials is the emergence of gapless modes at the boundaries and defects, despite topology being determined solely by bulk properties. Topological superconductors, for instance, are known to host Majorana fermions, which hold promise for applications in topological fault-tolerant quantum computation [30, 31]. This intersection of unique fundamental properties and potential applications has spurred extensive research efforts aimed at uncovering and understanding topological superconductivity [32, 33, 34, 35, 36, 37, 38, 39, 40, 41, 42, 43, 44, 45, 46, 47, 48, 49, 50, 51, 52, 53, 54, 55, 56, 57, 58, 59, 60, 61, 62, 63, 64, 65, 66, 67, 68, 69]. Despite these efforts, the realization and definitive characterization of topological superconductivity remain subjects of intense scientific debate.

Pioneering research has led to the classification of topological phases based on local symmetries, namely time-reversal, particle-hole, and chiral symmetries [70, 71, 72]. It has since been recognized that the unique symmetries of solid materials can enrich their topological properties. This understanding gave rise to the concept of topological crystalline insulators and superconductors (TCIs/TCSCs) [73, 74, 75, 76, 77, 78, 79, 80, 81, 82, 83, 84, 85, 86, 87, 88, 89, 90, 91, 92, 93, 94]. Despite this progress, the primary candidates for TCSCs

are typically odd-parity superconductors, similar to most known topological superconductors [27, 28, 29]. However, these odd-parity superconductors are often spin-triplet, a rarity in nature. Recently, there has been growing interest in superconductivity that defies the standard classification theory [95], with reports of odd-parity superconductivity arising from conventional spin-singlet pairing in $CeRh_2As_2$ [2]. This groundbreaking discovery could pave a new path for realizing topological superconductivity

The work described in this Chapter was inspired by a recent experimental discovery of an unconventional superconducting H-T phase diagram in the newly identified heavy-fermion superconductor $CeRh_2As_2$ [2]. This material exhibits a high upper critical field exceeding the Pauli-Clogston-Chandrasekhar limit and a phase transition between two distinct superconducting phases, making $CeRh_2As_2$ a prime candidate for exploring multiple superconducting phases. Unlike previous examples such as UPt_3 [96] and UTe_2 [97, 98, 99, 100], the unique phase diagram of $CeRh_2As_2$ has been linked to its locally noncentrosymmetric crystal structure [2], resonating with earlier theoretical predictions [1]. Following this experimental revelation, a flurry of theoretical investigations has emerged to explore this intriguing phenomenon [101, 102, 103, 104]

Noncentrosymmetric superconductivity in globally inversion asymmetric systems has been a subject of research for several decades [33, 34, 35, 36, 37, 67, 68, 105, 106, 107, 108, 109, 110, 111, 112, 113, 114]. This concept has been recently extended to locally noncentrosymmetric systems, uncovering unique superconducting phenomena [1, 18, 81, 115, 116, 117, 118, 119, 120, 121, 122]. The H-T phase diagram of $CeRh_2As_2$ aligns with predictions from a two-sublattice Rashba model [1, 121]. The consistency between experimental observations [2] and theoretical models [1, 121] suggests that local inversion symmetry breaking is critical in $CeRh_2As_2$, with the high magnetic field region likely hosting a pair-density-wave (PDW) state. In the PDW state, the superconducting gap function alternates in sign across different Ce layers. A key feature of this phase is its odd-parity superconductivity, predominantly characterized by spin-singlet pairing. This odd parity arises due to the inversion symmetry-related sign change of the gap function between sublattices. Hence, locally noncentrosymmetric crystals offer a platform for odd-parity superconductivity without the need for rare spin-triplet pairing. $CeRh_2As_2$ may thus represent a novel type of topological superconductor, distinct from potential spin-triplet superconductors like UPt_3[78, 86], UCoGe[87], and UTe_2 [123].

2.1 Symmetry and notations in superconducting state

We begin with clarifying notations for general space group operation $\hat{g}$ in the normal and superconducting states, which will be used in this chapter. Here, $\hat{}$ emphasizes that it is an element of abstract algebras. In the following section, the special case $\hat{g} = \hat{G}$ (the glide operation) is considered. In Seitz notation, $\hat{g}$ is given by $\{p|\boldsymbol{\tau}\}$, in which p and $\boldsymbol{\tau}$ are point

group operation and translation operation, respectively. It acts on real-space coordinates as:

$$\hat{g}\boldsymbol{x} = p\boldsymbol{x} + \boldsymbol{\tau}. \tag{2.1.1}$$

In the crystals, the relation $\boldsymbol{x} = \boldsymbol{R} + \boldsymbol{r}_n$ holds, where $\boldsymbol{R}$ and $\boldsymbol{r}_n$ are the center of a unit cell and relative position of the n-th sublattice within a unit cell. For electrons with internal degrees of freedom labeled by l is transformed as,

$$\hat{g}c_l^\dagger\left(\boldsymbol{R} + \boldsymbol{r}_n\right)\hat{g}^{-1} = c_{l'}^\dagger\left(p\boldsymbol{R} + \Delta\boldsymbol{R}_n^g + \boldsymbol{r}_{n'}\right)\mathcal{D}_{n'n}^{\mathrm{SL}}(p)\mathcal{D}_{l'l}^{\mathrm{int}}(p), \tag{2.1.2}$$

where $\mathcal{D}_{n'n}^{\mathrm{SL}}(p) = \delta_{n',\hat{g}(n)}$, $\mathcal{D}_{l'l}^{\mathrm{int}}(p)$ is a representation matrix associated with internal degrees of freedom, and $\Delta\boldsymbol{R}_n^g$ represents the displacement of the unit cells before and after the symmetry operation $\hat{g}$. The relation: $p\boldsymbol{r}_n = \Delta\boldsymbol{R}_n^g + \boldsymbol{r}_{n'}$ must be held. In the periodic boundary conditions, we conduct Fourier transform:

$$c_{\boldsymbol{k}ln}^\dagger \equiv \frac{1}{\sqrt{V}}\sum_{\boldsymbol{R}} e^{i\boldsymbol{k}\cdot\boldsymbol{R}}c_l^\dagger\left(\boldsymbol{R} + \boldsymbol{r}_n\right), \tag{2.1.3}$$

in which the basis is periodic in the Brillouin zone,

$$c_{\boldsymbol{k}ln}^\dagger = c_{\boldsymbol{k}+\boldsymbol{G}ln}^\dagger, \tag{2.1.4}$$

with any reciprocal lattice vector $\boldsymbol{G}$. Assuming that $\hat{T}_{\boldsymbol{a}}$ is a primitive lattice translation operator, we have

$$\hat{T}_{\boldsymbol{a}}c_{\boldsymbol{k}ln}^\dagger\hat{T}_{\boldsymbol{a}}^\dagger = \frac{1}{\sqrt{V}}\sum_{\boldsymbol{R}} e^{i\boldsymbol{k}\cdot\boldsymbol{R}}c_l^\dagger\left(\boldsymbol{R} + \boldsymbol{a} + \boldsymbol{r}_n\right) \tag{2.1.5}$$

$$= \frac{1}{\sqrt{V}}e^{-\boldsymbol{k}\cdot\boldsymbol{a}}\sum_{\boldsymbol{R}} e^{i\boldsymbol{k}\cdot(\boldsymbol{R}+\boldsymbol{a})}c_l^\dagger\left(\boldsymbol{R} + \boldsymbol{a} + \boldsymbol{r}_n\right) \tag{2.1.6}$$

$$= e^{-\boldsymbol{k}\cdot\boldsymbol{a}}c_{\boldsymbol{k}ln}^\dagger. \tag{2.1.7}$$

Therefore, $\boldsymbol{k}$ labels eigenvalues of the primitive lattice translation, and from the fact that $[\hat{H}, \hat{T}_{\boldsymbol{a}}] = 0$, we can divide the Hilbert space into each $\boldsymbol{k}$ sector,

$$\mathbb{V} = \bigoplus_{\boldsymbol{k}} \mathbb{V}_{\boldsymbol{k}}. \tag{2.1.8}$$

This is nothing but the Bloch theorem. The dimension of $\mathbb{V}_{\boldsymbol{k}}$ is identical with the number of degrees of freedom such as spin, orbital, and sublattice. In the space $\mathbb{V}_{\boldsymbol{k}}$, we can represent

the symmetry operation $\hat{g}$,

$$\hat{g}c^\dagger_{\boldsymbol{k},\alpha}\hat{g}^{-1} = \frac{1}{\sqrt{V}}\sum_{\boldsymbol{R}} e^{i\boldsymbol{k}\cdot\boldsymbol{R}} c^\dagger_{l'}\left(p\boldsymbol{R} + \Delta\boldsymbol{R}^g_n + \boldsymbol{r}_{n'}\right)\mathcal{D}^{\mathrm{SL}}_{n'n}(p)\mathcal{D}^{\mathrm{int}}_{l'l}(p) \tag{2.1.9}$$

$$= \frac{1}{\sqrt{V}}\sum_{\boldsymbol{R}'=p\boldsymbol{R}+\Delta\boldsymbol{R}^g_n} e^{i\boldsymbol{k}\cdot(p^{-1}(\boldsymbol{R}'-\Delta\boldsymbol{R}^g_n))} c^\dagger_{l'}\left(\boldsymbol{R}' + \boldsymbol{r}_{n'}\right)\mathcal{D}^{\mathrm{SL}}_{n'n}(p)\mathcal{D}^{\mathrm{int}}_{l'l}(p) \tag{2.1.10}$$

$$= \frac{1}{\sqrt{V}} e^{-ip\boldsymbol{k}\cdot\Delta\boldsymbol{R}^g_n}\sum_{\boldsymbol{R}'} e^{ip\boldsymbol{k}\cdot\boldsymbol{R}'} c^\dagger_{l'}\left(\boldsymbol{R}' + \boldsymbol{r}_{n'}\right)\mathcal{D}^{\mathrm{SL}}_{n'n}(p)\mathcal{D}^{\mathrm{int}}_{l'l}(p) \tag{2.1.11}$$

$$= c^\dagger_{p\boldsymbol{k}\,l'n'} e^{-ip\boldsymbol{k}\cdot\Delta\boldsymbol{R}^g_n}\mathcal{D}^{\mathrm{SL}}_{n'n}(p)\mathcal{D}^{\mathrm{int}}_{l'l}(p) \tag{2.1.12}$$

$$= c^\dagger_{p\boldsymbol{k},\beta}\mathcal{D}^g(\boldsymbol{k})_{\beta\alpha}, \tag{2.1.13}$$

where α, β represent total internal degrees of freedom of electrons, $\alpha = (l, n)$, $\beta = (l', n')$, and $\mathcal{D}^g(\boldsymbol{k})$ is the representation matrix of $\hat{g}$. From Eq. (2.1.13), $\mathcal{D}^g(\boldsymbol{k})_{\beta\alpha} = e^{-ip\boldsymbol{k}\cdot\Delta\boldsymbol{R}^g_n}\mathcal{D}^{\mathrm{SL}}_{n'n}(p)\mathcal{D}^{\mathrm{int}}_{l'l}(p)$. When the Hamiltonian $\hat{H} = \sum_{\boldsymbol{k},\alpha,\beta} c^\dagger_{\boldsymbol{k}\alpha}[\mathcal{H}(\boldsymbol{k})]_{\alpha\beta}c_{\boldsymbol{k}\beta}$ preserves the symmetry $\hat{g}$, $[\hat{H}, \hat{g}] = 0$, the following relation is satisfied

$$\mathcal{D}^g(\boldsymbol{k})\mathcal{H}(\boldsymbol{k})(\mathcal{D}^g(\boldsymbol{k}))^\dagger = \mathcal{H}(p\boldsymbol{k}). \tag{2.1.14}$$

Though superconducting gap function may break the space group symmetry $\hat{g}$, the symmetry in the normal state is preserved in combination with the $U(1)$ symmetry, at least when the superconductivity belongs to a one-dimensional irreducible representation. The representation matrix is given by

$$\mathcal{D}^g_{\mathrm{BdG}}(\boldsymbol{k}) = \begin{pmatrix} \mathcal{D}^g(\boldsymbol{k}) & 0 \\ 0 & \pm\left(\mathcal{D}^g(-\boldsymbol{k})\right)^* \end{pmatrix}_\tau, \tag{2.1.15}$$

where the positive (negative) sign corresponds to $\hat{g}$-even ($\hat{g}$-odd) superconductivity, as

$$\mathcal{D}^g(\boldsymbol{k})\Delta(\boldsymbol{k})(\mathcal{D}^g(-\boldsymbol{k}))^\top = \pm\Delta(p\boldsymbol{k}), \tag{2.1.16}$$

and we take Nambu basis as $\psi(\boldsymbol{k}) = (c_{\boldsymbol{k}}, c^\dagger_{-\boldsymbol{k}})^\top$. In the Nambu space, the Bogoliubov–de Gennes (BdG) Hamiltonian takes the form:

$$\hat{H}_{\mathrm{BdG}} = \frac{1}{2}\sum_{\boldsymbol{k}} \psi^\dagger(\boldsymbol{k})\mathcal{H}_{\mathrm{BdG}}(\boldsymbol{k})\psi(\boldsymbol{k}), \tag{2.1.17}$$

$$\mathcal{H}_{\mathrm{BdG}}(\boldsymbol{k}) = \begin{pmatrix} \mathcal{H}(\boldsymbol{k}) & \Delta(\boldsymbol{k}) \\ \Delta^\dagger(\boldsymbol{k}) & -\mathcal{H}^\top(-\boldsymbol{k}) \end{pmatrix}_\tau, \tag{2.1.18}$$

where we represent the index of Nambu space as τ. In the superconducting state, the particle-hole symmetry is always preserved,

$$\mathcal{C}\mathcal{H}_{\mathrm{BdG}}(\boldsymbol{k})\mathcal{C}^{-1} = -\mathcal{H}_{\mathrm{BdG}}(-\boldsymbol{k}), \tag{2.1.19}$$

$$\mathcal{C} = \begin{pmatrix} 0 & 1 \\ 1 & 0 \end{pmatrix}_\tau \mathcal{K}, \tag{2.1.20}$$

with $\mathcal{K}$ being the complex conjugation. From direct calculations, we confirm the following relation:

$$\mathcal{C}\mathcal{D}^{g}_{\mathrm{BdG}}(\boldsymbol{k}) = \pm\mathcal{D}^{g}_{\mathrm{BdG}}(-\boldsymbol{k})\mathcal{C}. \tag{2.1.21}$$

In the following, we adopt the notation $\{\hat{g}, \hat{C}\} = 0$ in the sense of Eq. (2.1.21) with the negative sign.

2.2 Crystal structure and glide symmetry

$CeRh_2As_2$ crystallizes in the centrosymmetric tetragonal $CaBe_2Ge_2$-type structure [2], featuring alternating layers of Ce and Rh_2As_2. A key characteristic of this structure is the local inversion symmetry breaking at Ce sites, despite the presence of a global inversion center between two Ce sites in the unit cell. The space group of $CeRh_2As_2$ is $P4/nmm$ (No.129), which includes a glide reflection and three screw rotations. When a magnetic field is applied parallel to the c-axis, the screw symmetries are disrupted, leaving only the glide symmetry intact. In our analysis, we focus on the glide operation $\hat{G}$, represented in Seitz notation as $\{M_z|\boldsymbol{a}/2 + \boldsymbol{b}/2\}$, where $\boldsymbol{a}$ and $\boldsymbol{b}$ are lattice vectors along the a and b axes, respectively.

In the Brillouin zone, the glide symmetry is maintained in the glide-invariant planes at $k_z = 0, \pi$. The Hilbert space can thus be divided based on each Bloch state and glide sector as follows:

$$\mathbb{V}_{k_z=0,\pi} = \bigoplus_{\boldsymbol{k}\in \mathrm{BZ}_{k_z=0,\pi}} \mathbb{V}^{\mathfrak{g}^+}_{\boldsymbol{k}} \oplus \mathbb{V}^{\mathfrak{g}^-}_{\boldsymbol{k}}. \tag{2.2.1}$$

Here, $\mathbb{V}_{\boldsymbol{k}}$ represents the Hilbert space of Bloch states labeled by $\boldsymbol{k}$, and $\mathfrak{g}^{\pm}$ are the eigenvalues of the glide operation. Since the Hamiltonian preserves glide symmetry, i.e., $[\hat{H}, \hat{G}] = 0$, eigenstates of the Hamiltonian can be labeled by glide eigenvalues as $|\boldsymbol{k}^{\mathfrak{g}^{\pm}}\rangle \in \mathbb{V}^{\mathfrak{g}^{\pm}}_{\boldsymbol{k}}$. To determine the eigenvalues in the spinful case, we consider the relation:

$$\hat{G}^2 = \{-E|\boldsymbol{a} + \boldsymbol{b}\}. \tag{2.2.2}$$

According to Eq. (2.2.2), any state $|\boldsymbol{k}\rangle$ in $\mathbb{V}_{k_z=0,\pi}$ satisfies:

$$\hat{G}^2 |\boldsymbol{k}\rangle = -e^{-i(k_x+k_y)} |\boldsymbol{k}\rangle, \tag{2.2.3}$$

leading to the conclusion that the glide eigenvalues are given by:

$$\mathfrak{g}^{\pm} = \pm ie^{-i(k_x+k_y)/2}. \tag{2.2.4}$$

2.3 Symmetry of superconductivity

Superconductivity in $CeRh_2As2$ is categorized under the point group D_{4h}, which encompasses 8 one-dimensional (1D) irreducible representations and 2 two-dimensional (2D) representations. Commonly, many Ce-based heavy-fermion systems exhibit spin-singlet superconductivity, and $CeRh_2As_2$ is expected to follow this trend at zero magnetic field ($H = 0$). Consequently, the low-field superconducting phase of $CeRh_2As_2$ is likely to be an even-parity state, corresponding to one of the A_{1g}, A_{2g}, B_{1g}, B_{2g}, or E_g states. On the other hand, in the presence of a high magnetic field, if we assume a pair-density-wave (PDW) state, the superconducting phase would transition to an odd-parity state, specifically A_{1u}, A_{2u}, B_{1u}, B_{2u}, or E_u. However, for the scope of this discussion, we will focus primarily on 1D odd-parity representations, as the E_u state is considered unlikely in $CeRh_2As_2$ [2].

2.4 $\mathbb{Z}_2$ invariants

In our discussion of the $\mathbb{Z}_2$ topological invariants, we focus on their protection by glide symmetry in the context of the PDW state. The PDW state is characterized as glide-odd superconductivity, where the superconducting gap function adheres to the following relation:

$$\mathcal{G}(\boldsymbol{k})\Delta(\boldsymbol{k})\mathcal{G}^{\top}(-\boldsymbol{k}) = -\Delta(M_z\boldsymbol{k}). \tag{2.4.1}$$

In this equation, $\mathcal{G}(\boldsymbol{k})$ denotes the representation matrix of the glide operation $\hat{G}$ within the Hilbert space $\mathbb{V}_{\boldsymbol{k}}$. The term $M_z\boldsymbol{k}$ is defined as $(k_x, k_y, -k_z)$, and $\Delta(\boldsymbol{k})$ represents the superconducting gap function. This relation encapsulates the key characteristic of the PDW state in terms of its behavior under the glide operation.

In our analysis, we concentrate on the glide invariant planes within the Brillouin zone, specifically at $k_z = 0, \pi$. Based on Eq.(2.4.1), we note that the particle-hole operation $\hat{C}$ and the glide operation $\hat{G}$ anti-commute, satisfying $\{\hat{C}, \hat{G}\} = 0$. Additionally, from Eq.(2.2.4), the glide eigenvalues are determined to be purely imaginary ($\pm i$) within the restricted Hilbert space on the line where $k_x + k_y = 0$. Integrating these results, we confirm that particle-hole symmetry is preserved within each glide sector:

$$\hat{G}\hat{C}\,|\boldsymbol{k}^{\mathfrak{g}^{\pm}}\rangle = -\hat{C}(\pm i)\,|\boldsymbol{k}^{\mathfrak{g}^{\pm}}\rangle = (\pm i)\hat{C}\,|\boldsymbol{k}^{\mathfrak{g}^{\pm}}\rangle\,. \tag{2.4.2}$$

Considering the breakdown of time-reversal symmetry under a magnetic field, each glide sector along this line is classified as 1D class D superconductivity. This classification is defined by a topological invariant $\mathbb{Z}_2$, as described by the integral of the Berry connection outlined in Ref. [84]:

$$\nu^{\mathfrak{g}^{\pm}} = \frac{1}{\pi}\int_{\Gamma_1}^{\Gamma_2} d\,k_i\,\mathcal{A}_i^{\mathfrak{g}^{\pm}}(\boldsymbol{k}) \quad (\mathrm{mod}\ 2), \tag{2.4.3}$$

where $\mathcal{A}_i^{\mathfrak{g}^\pm}(\boldsymbol{k})$ represents the i-th components of the Berry connection in each glide sector, expressed as $i\sum_{\text{occ.}}\langle\psi_{\boldsymbol{k}}^{\mathfrak{g}^\pm}|\partial_{k_i}|\psi_{\boldsymbol{k}}^{\mathfrak{g}^\pm}\rangle$. Here, $|\psi_{\boldsymbol{k}}^{\mathfrak{g}^\pm}\rangle$ denotes the occupied eigenstates of the Bogoliubov–de Gennes (BdG) Hamiltonian in each glide sector with the glide eigenvalue $\mathfrak{g}^\pm$. The time-reversal invariant momenta (TRIM) are designated as $\Gamma_1 = (0,0,0)$ (at the Γ point) or $(0,0,\pi)$ (at the Z point) and $\Gamma_2 = (\pi,-\pi,0)$ (at the M point) or $(\pi,-\pi,\pi)$ (at the A point), varying based on whether $k_z = 0$ or π.

In addition to the glide $\mathbb{Z}_2$ invariants $\nu^{\mathfrak{g}^\pm}$, it's possible to define the Chern number C as well as two Zak phases, γ and γ', on the lines $k_x + k_y = \pi$ and 0, respectively. However, these invariants are not independent entities. Specifically, it holds that $\gamma' = \nu^{\mathfrak{g}^+} + \nu^{\mathfrak{g}^-}$. We will later demonstrate that $\gamma = 0$. Consequently, the topological nature of the PDW state for $k_z = 0, \pi$ can be effectively characterized by identifying $\nu^{\mathfrak{g}^\pm}$ and C, denoted as $\nu_{0,\pi}^{\mathfrak{g}^\pm}$ and $C_{0,\pi}$ for each respective k_z value. The Chern number is related to these invariants as follows:

$$C = \gamma' - \gamma \pmod 2, \tag{2.4.4}$$

$$= \nu^{\mathfrak{g}^+} + \nu^{\mathfrak{g}^-} \pmod 2. \tag{2.4.5}$$

This implies that only one of $\nu^{\mathfrak{g}^\pm}$ is a strong topological index, in line with the K-theory classification for the strong indices $\mathbb{Z}\oplus\mathbb{Z}_2$ [84]. In this paper, we focus on $\nu^{\mathfrak{g}^\pm}$ and C modulo two in the context of $CeRh_2As_2$, as their determination does not depend on the specific details of the order parameter. They are dictated solely by the topology of the Fermi surfaces and do not necessitate a comprehensive calculation of the symmetry indicators [88, 89, 90, 91, 92, 93, 94].

To further simplify the expression in Eq. (2.4.3), we consider the relationship between the space inversion operation $\hat{I}$ and the glide operation $\hat{G}$:

$$\hat{I}\hat{G} = \hat{G}\hat{I}\{E|\boldsymbol{a}+\boldsymbol{b}\}, \tag{2.4.6}$$

In this equation, $\{E|\boldsymbol{a}+\boldsymbol{b}\}$ effectively reduces to a phase factor $e^{-i(k_x+k_y)}$. Consequently, in the Hilbert space $\mathbb{V}_{k_x+k_y=0,k_z=0,\pi}$, the operations $\hat{I}$ and $\hat{G}$ commute. This implies that the space inversion parity is well-defined within each glide sector, categorizing each sector as a 1D class D odd-parity superconductor. Utilizing the Fermi-surface formula for odd-parity superconductors [55, 56], we can evaluate the $\mathbb{Z}_2$ invariant based on the topology of the Fermi surfaces. This leads to the conclusion that the glide $\mathbb{Z}_2$ invariant $\nu^{\mathfrak{g}^\pm}$ is nontrivial (trivial) when the number of Fermi surfaces between Γ_1 and Γ_2 is odd (even):

$$\nu_0^{\mathfrak{g}^\pm} = \#\mathrm{FS}^\pm_{\Gamma\to M} \pmod 2, \tag{2.4.7}$$

$$\nu_\pi^{\mathfrak{g}^\pm} = \#\mathrm{FS}^\pm_{Z\to A} \pmod 2. \tag{2.4.8}$$

Thus, the topological nature of the PDW state in $CeRh_2As_2$ for $k_z = 0, \pi$ can be characterized by these simplified $\mathbb{Z}_2$ invariants.

In a similar fashion, the Zak phase γ can also be connected to the number of Fermi surfaces. Considering the Bogoliubov–de Gennes (BdG) Hamiltonian on the line $k_x + k_y = \pi$, which can be treated as a 1D odd-parity superconductor, the Fermi surface formula [55, 56] gives us:

$$\gamma_{0,\pi} = \#\mathrm{FS}_{\Gamma_1 \to \Gamma_2} \pmod 2. \tag{2.4.9}$$

Here, for $k_z = 0, \pi$, Γ_1 and Γ_2 correspond to X, R and X', R', respectively. Due to the four-fold rotation symmetry C_4^z, the occupation numbers of electrons at Γ_1 and Γ_2 are equal. As a result, electron bands must intersect the Fermi level an even number of times between Γ_1 and Γ_2. This leads to the conclusion that $\gamma_{0,\pi} = 0$.

In the following analysis, we perform first-principles calculations for $CeRh_2As_2$ to evaluate the $\mathbb{Z}_2$ invariants. These calculations are conducted in the absence of a magnetic field, where all electronic bands are doubly degenerate. The degenerate states, $|\boldsymbol{k}^{\mathfrak{g}^\pm}\rangle$ and $\hat{I}\hat{\Theta}\,|\boldsymbol{k}^{\mathfrak{g}^\pm}\rangle$, are a consequence of the inversion symmetry $\hat{I}$ and time-reversal symmetry $\hat{\Theta}$. The relationship:

$$\hat{G}\hat{I}\hat{\Theta}\,|\boldsymbol{k}^{\mathfrak{g}^\pm}\rangle = \hat{I}\hat{\Theta}\hat{G}\,|\boldsymbol{k}^{\mathfrak{g}^\pm}\rangle = \mathfrak{g}^\mp \hat{I}\hat{\Theta}\,|\boldsymbol{k}^{\mathfrak{g}^\pm}\rangle\,, \tag{2.4.10}$$

indicates that the degenerate states belong to distinct glide sectors. As a result, the number of Fermi surfaces is equal across the two glide sectors, aligning with the number of spinful bands that cross the Fermi level: $\#\mathrm{FS}^+_{\Gamma_1\to\Gamma_2} = \#\mathrm{FS}^-_{\Gamma_1\to\Gamma_2} \equiv \#\mathrm{FS}_{\Gamma_1\to\Gamma_2}$. Notably, the application of a magnetic field does not modify the $\mathbb{Z}_2$ invariants and the Chern number modulo two, provided it does not induce a Lifshitz transition. The implications of potential Lifshitz transitions will be addressed later in our discussion.

2.5 Band structure of $CeRh_2As_2$

We have conducted a DFT band structure calculation for $CeRh_2As_2$ using the WIEN2k code [124]. $CeRh_2As_2$ crystallizes in the space group $P4/nmm$ (No.129), with crystallographic parameters as experimentally determined and listed in Table 2.1 [2]. Our approach utilizes the full-potential linearized augmented plane wave plus local orbitals (LAPW+lo) method within the generalized gradient approximation (GGA), incorporating spin-orbit coupling effects. For our calculation, the maximum reciprocal lattice vector $K_{\max}$ is set such that $R_{\mathrm{MT}}K_{\max} = 8.0$. We have chosen muffin-tin radii R_{MT} of 2.50, 2.42, and 2.15 atomic units (a.u.) for Ce, Rh, and As atoms, respectively. A $13\times13\times5$ k-points grid is used for the self-consistent calculation. We have verified that increasing the density to an $18\times18\times8$ k-points grid yields almost identical results. Because the experimental values of the crystallographic parameters are different from those obtained by a lattice optimizing calculation [103], we calculated the electronic band structure using WIEN2k for the latter parameters and obtained nearly the same results.

Table 2.1: Atomic coordinates of $CeRh_2As_2$ [2]. Lattice constants are $a = b = 4.2801$ Å and $c = 9.8616$ Å.

Atom	x	y	z
Ce ($2c$)	0.25	0.25	0.25469
Rh1 ($2a$)	0.75	0.25	0
Rh2 ($2c$)	0.25	0.25	0.61742
As1 ($2b$)	0.75	0.25	0.5
As2 ($2c$)	0.25	0.25	0.86407

Figure 2.1(a) presents the band structure of $CeRh_2As_2$, which notably features heavy bands of Ce $4f$ electrons in proximity to the Fermi level. These Ce $4f$ orbitals predominantly contribute to the density of states at the Fermi level. The Fermi surfaces derived from our calculations are depicted in Fig. 2.2. We observe that the Fermi surface is primarily composed of Ce $4f$ electrons, with significant hybridization with Rh $4d_{x^2-y^2}$ electrons, except for the pink pockets near the A point [Fig. 2.2(d)]. The largest Fermi surface [Fig. 2.2(c)] exhibits a quasi-two-dimensional character, aligning with the predictions for the field-induced PDW state[1]. This is corroborated by experimental observations of the Kondo effect in $CeRh_2As_2$ [2], with an electronic specific heat coefficient γ of approximately $1000, \mathrm{mJ/mol, K^2}$, indicating the presence of heavy-fermion bands. Further insight is provided in Fig.2.3, where the partial density of states for Ce and Rh atoms, along with the total density of states, are displayed. Additionally, the orbital weights for the Ce $4f$, Rh1 $4d$, Rh2 $4d$, As1 $4p$, and As2 $4p$-orbitals are illustrated in Fig.2.4. The data confirm that the primary contributions near the Fermi level are from the Ce $4f$-orbital, in line with the heavy-fermion behavior observed in experiments on $CeRh_2As_2$ [2].

In the subsequent discussion, we base our analysis on DFT calculations. The universality of the formulas (2.4.7) and (2.4.8) for $\mathbb{Z}_2$ invariants allows us to assess whether $CeRh_2As_2$ qualifies as a TCSC, contingent upon the topology of its Fermi surfaces. While our focus is on the spin-singlet pairing dominant pair-density-wave (PDW) state, it's important to note that the key aspects for applying the Fermi-surface formula are the odd-parity and glide-odd characteristics of the PDW state. These characteristics are underpinned by the inversion operation's negative character and the glide operation for A_{1u}, A_{2u}, B_{1u}, and B_{2u} states, irrespective of whether the spin-singlet or spin-triplet component predominates. Thus, our formula remains applicable to spin-triplet dominant states as well, such as those proposed in Ref. [101]. It should be noted that the magnitude of the spin-triplet channel influences various physical properties, including the paramagnetic effect and the local density of states [118]. These properties can be experimentally measured, underscoring the need for further theoretical and experimental efforts to elucidate the nuances of the high-field phase. However, our

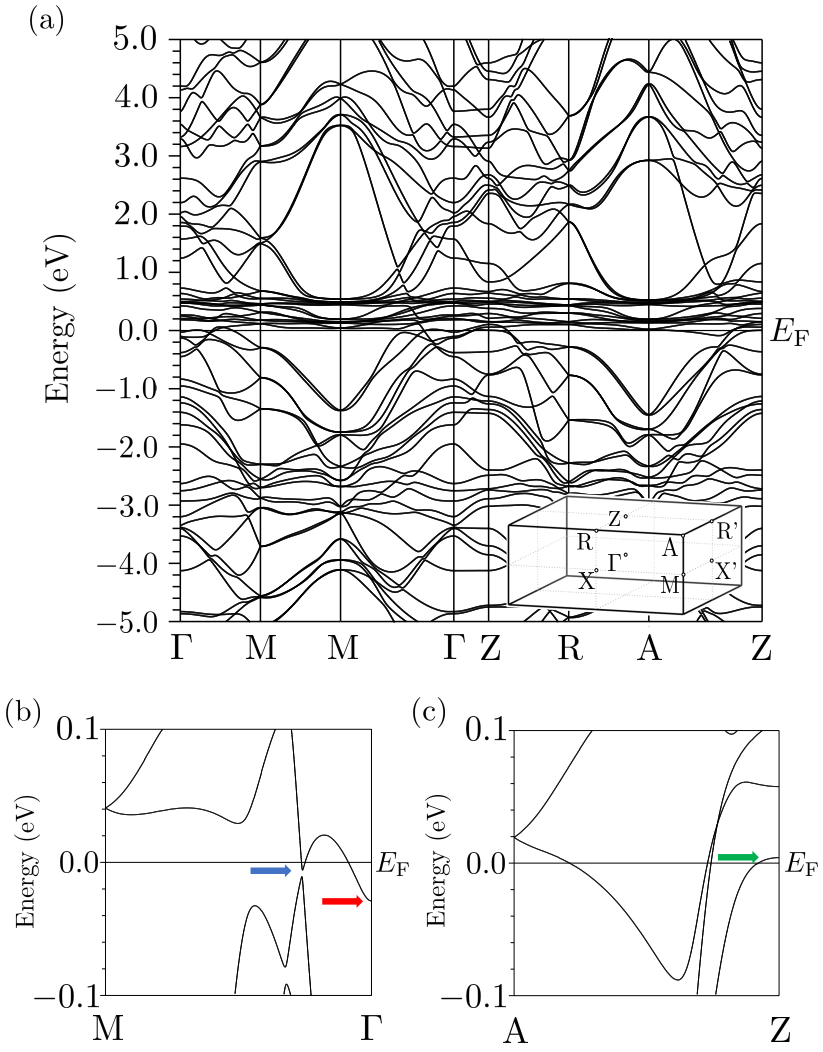

Figure 2.1: Electronic band structure of $CeRh_2As_2$ with spin-orbit coupling calculated by WIEN2k. (a) The whole bands along symmetric lines. The heavy bands of Ce $4f$ electrons are seen near the Fermi level. (b) Enlarged view along the M-Γ line. The bands cross the Fermi level three times. (c) Enlarged view along the A-Z line. The bands cross the Fermi level four times.

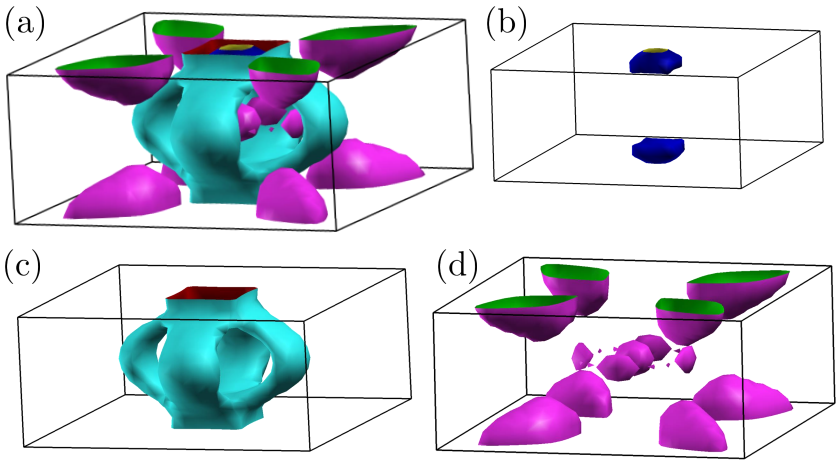

Figure 2.2: (a) Fermi surfaces of $CeRh_2As_2$. Each Fermi surface is shown in (b)–(d). The Fermi surfaces other than the pockets around the A point in (d) are mainly constituted by Ce $4f$ electrons. The figures are generated by XCrySDen software [125].

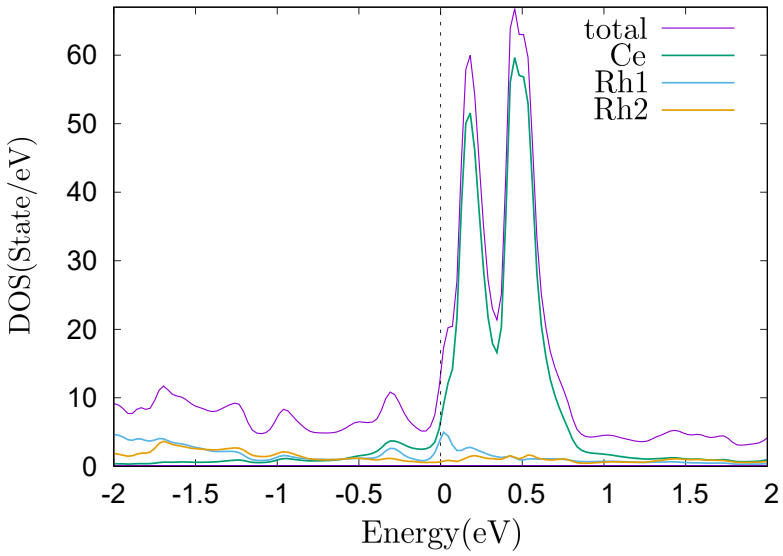

Figure 2.3: Total density of states and partial density of states of Ce, Rh1, and Rh2 sites.

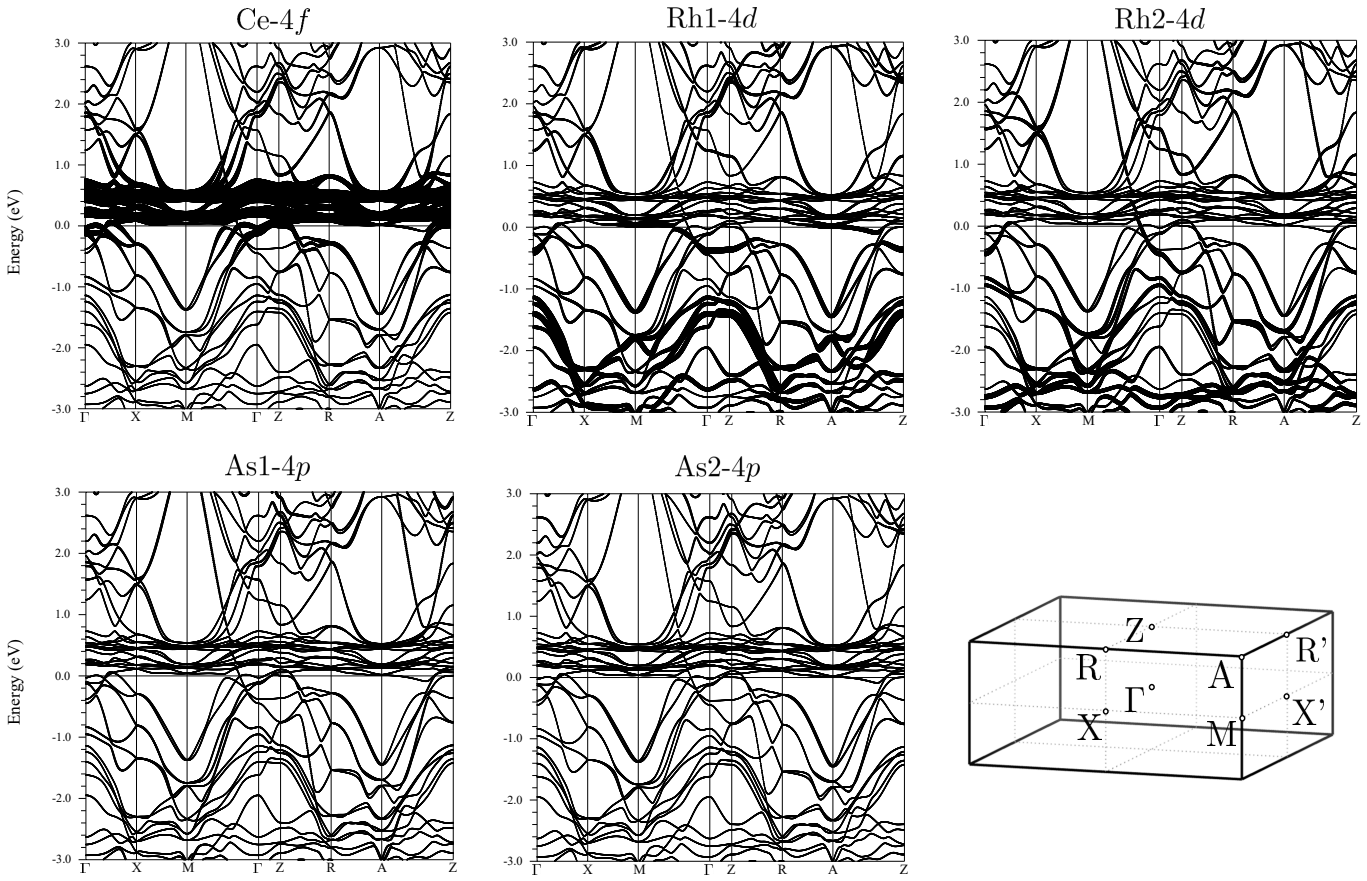

Figure 2.4: Orbital weight for the Ce-4f, Rh1-4d, Rh2-4d, As1-4p, and As2-4p orbitals. Symmetry points in the Brillouin zone are also illustrated.

forthcoming results remain valid regardless of these specifics.

2.6 TCSC in $CeRh_2As_2$

We now turn our attention to the $\mathbb{Z}_2$ invariants in $CeRh_2As_2$. Specifically, we examine the topology on the glide-invariant plane at $k_z = 0$. Analysis of the Γ-M line, as shown in Fig. 2.1(b), reveals that bands intersect the Fermi level three times. Consequently, both $\nu_0^{\mathfrak{g}^\pm}$ are determined to be nontrivial, signifying the presence of TCSC. Notably, TCSC in $CeRh_2As_2$ is robust against Zeeman splitting. Under a magnetic field range of 4 T to 14 T, where the PDW state is observed [2], the Zeeman splitting energy is estimated to be within the range of $2 \sim 8$ meV, assuming a g-factor of $g = 10$, which is likely an overestimation. At the Γ point (indicated by the red arrow in the figure), the conduction band is approximately 30 meV below the Fermi level, which implies that the occupation number remains unchanged under the influence of the magnetic field. While the band crossings marked by the blue arrow might be affected by the magnetic field, this does not alter the $\mathbb{Z}_2$ invariants as per the formula (2.4.7). Therefore, the parity of the number of Fermi surfaces is preserved under the magnetic field, maintaining the nontrivial nature of the $\mathbb{Z}_2$ invariants $\nu_0^{\mathfrak{g}^\pm}$ in the PDW state.

We now turn our attention to the other glide-invariant plane, $k_z = \pi$. Along the Z-A line, as depicted in Fig.2.1(c), the bands intersect the Fermi level four times, making $\nu_\pi^{\mathfrak{g}^\pm}$ trivial. However, the presence of a shallow hole band (marked by a green arrow), with its energy at the Z point estimated to be around ~ 4 meV, suggests the possibility of a Lifshitz transition in a magnetic field, potentially leading to nontrivial $\mathbb{Z}_2$ invariants. The $\mathbb{Z}_2$ topological invariants of $CeRh_2As_2$, based on band structure calculations, are detailed in Table 2.2. We hypothesize that under high magnetic fields at the Z point, a Zeeman split band may undergo this Lifshitz transition, rendering both the Chern number and $\mathbb{Z}_2$ invariant nontrivial. The well-defined nature of the Chern number on any constant k_z plane, and the observed difference between C_0 and $C\pi$, suggests a parallel with the Weyl superconducting state as in UPt_3 [126].

Table 2.2: $\mathbb{Z}_2$ topological invariants and Chern number of $CeRh_2As_2$ in the PDW state based on the first-principles calculation. A possibility of a Weyl superconducting state is shown. In the high-field region, one of the Zeeman split bands is supposed to cause Lifshitz transition at the Z point.

	$(\nu_0^{\mathfrak{g}^+}, \nu_0^{\mathfrak{g}^-}, C_0)$	$(\nu_\pi^{\mathfrak{g}^+}, \nu_\pi^{\mathfrak{g}^-}, C_\pi)$	Weyl SC
Low field	$(1, 1, \text{even})$	$(0, 0, \text{even})$	$\times$
High field	$(1, 1, \text{even})$	$(1, 0, \text{odd})$ or $(0, 1, \text{odd})$	$\circ$

These results establish $CeRh_2As_2$ as a promising platform for topological crystalline superconductivity (TCSC). It is important to emphasize that the glide $\mathbb{Z}_2$ invariants are nontriv-

ial, specifically on the $k_z = 0$ plane. Consequently, this leads to the emergence of boundary Majorana states on the $(\bar{1}10)$ surface, which maintains glide symmetry. This symmetry is constituted by the vectors $\boldsymbol{a} + \boldsymbol{b}$ and $\boldsymbol{c}$.

2.7 Model study

To demonstrate the emergence of Majorana surface states, we employed numerical calculations using a tight-binding model tailored for $CeRh_2As_2$. This model aligns with our first-principles calculations, with parameters set to ensure $\#\mathrm{FS}^{\pm}_{\Gamma_1\to\Gamma_2}$ are odd (even) at $k_z = 0$ ($k_z = \pi$). Here, we present a single-orbital tight-binding model focused solely on the Ce atoms. The model incorporates superconducting gap functions represented in the A_{1u}, A_{2u}, B_{1u}, and B_{2u} categories. This framework is specifically designed for analyzing topological surface states in $CeRh_2As_2$.

2.7.1 Normal-part Hamiltonian and model parameters

First, we show the spin-independent part of the Hamiltonian:

$$\hat{H}_{\mathrm{kin}} = -t\sum_{i,s,\sigma}\left(c^{\dagger}_{i+a,s,\sigma}c_{i,s,\sigma} + c^{\dagger}_{i+b,s,\sigma}c_{i,s,\sigma} + h.c\right) \tag{2.7.1}$$

$$- t'\sum_{i,s}\Big(c^{\dagger}_{i,s,A}c_{i,s,B} + c^{\dagger}_{i+a,s,A}c_{i,s,B} + c^{\dagger}_{i+b,s,A}c_{i,s,B} + c^{\dagger}_{i+a+b,s,A}c_{i,s,B}$$

$$+ c^{\dagger}_{i+c,s,A}c_{i,s,B} + c^{\dagger}_{i+a+c,s,A}c_{i,s,B} + c^{\dagger}_{i+b+c,s,A}c_{i,s,B} + c^{\dagger}_{i+a+b+c,s,A}c_{i,s,B} + h.c.\Big) \tag{2.7.2}$$

$$= \sum_{\boldsymbol{k},s}\Big[-2t(\cos k_x a + \cos k_y a)\sigma_0 - \frac{t'}{2}(1+e^{-ik_x a})(1+e^{-ik_y a})(1+e^{-ik_z c})(\sigma_x + i\sigma_y) \tag{2.7.3}$$

$$- \frac{t'}{2}(1+e^{ik_x a})(1+e^{ik_y a})(1+e^{ik_z c})(\sigma_x - i\sigma_y)\Big]_{\sigma\sigma'} c^{\dagger}_{\boldsymbol{k},s,\sigma}c_{\boldsymbol{k},s,\sigma'}. \tag{2.7.4}$$

where we take primitive translation vectors as $\boldsymbol{a} = (a, 0, 0)$, $\boldsymbol{b} = (0, a, 0)$, and $\boldsymbol{c} = (0, 0, c)$. Here, $c_{i,s,\sigma}$ ($c^{\dagger}_{i,s,\sigma}$) are annihilation (creation) operators for the Ce $4f$ electron with the lattice point $\boldsymbol{R}_i$, spin s, and sublattice σ. Equations (2.7.1) and (2.7.2) represent the intra-sublattice hopping and inter-sublattice hopping, respectively, with t and t' being intra- and inter-sublattice hopping integrals (Fig. 2.5). To obtain Eq. (2.7.3), we conducted Fourier

transform in which Bloch basis is periodic in the Brillouin zone,

$$c_{i,s,A} = \frac{1}{\sqrt{N}} \sum_{\boldsymbol{k}} c_{\boldsymbol{k},s,A} e^{i\boldsymbol{k}\cdot\boldsymbol{R}_i}, \tag{2.7.5}$$

$$c_{i,s,B} = \frac{1}{\sqrt{N}} \sum_{\boldsymbol{k}} c_{\boldsymbol{k},s,B} e^{i\boldsymbol{k}\cdot\boldsymbol{R}_i}. \tag{2.7.6}$$

Next, we show the spin-dependent part of the Hamiltonian:

$$\hat{H}_{\mathrm{ASOC}} = \sum_{s,s',\sigma} \alpha_\sigma \boldsymbol{g}(\boldsymbol{k}) \cdot c^\dagger_{\boldsymbol{k},s,\sigma} \boldsymbol{s}_{s,s'} c_{\boldsymbol{k},s',\sigma}, \tag{2.7.7}$$

$$\hat{H}_{\mathrm{Zeeman}} = \sum_{s,s',\sigma} -\mu_B \boldsymbol{H} \cdot c^\dagger_{\boldsymbol{k},s,\sigma} \boldsymbol{s}_{s,s'} c_{\boldsymbol{k},s',\sigma}. \tag{2.7.8}$$

$\hat{H}_{\mathrm{ASOC}}$ represents the antisymmetric spin-orbit coupling (ASOC) depending on the sublattice, that is, $\alpha_A = -\alpha_B = \alpha$. Since the site symmetry of the Ce site is C_{4v}, the g-vector has a Rashba-type form, $\boldsymbol{g}(\boldsymbol{k}) = (-2t \sin k_y a, 2t \sin k_x a, 0)$. The inter-sublattice ASOC is forbidden due to the presence of inversion center between A and B sublattices. $\hat{H}_{\mathrm{Zeeman}}$ represents the Zeeman coupling, and hereafter we assume $\boldsymbol{H} = (0, 0, H)$.

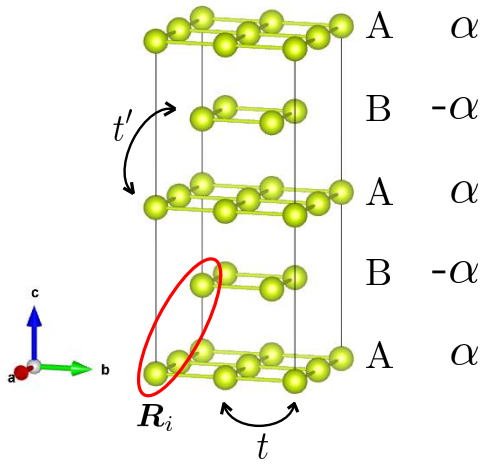

Figure 2.5: Structure of the tight-binding model. The Ce atoms of $CeRh_2As_2$ form the body-centered tetragonal lattice. The environmental Rh_2As_2 layers break the local inversion symmetry at the Ce sites. The local inversion symmetry breaking introduces the A and B sublattice structure. The Rashba-type antisymmetric spin-orbit coupling on each sublattice affects the electronic structure, and the sign of the spin-orbit coupling is opposite between the A and B sublattices. The red circle represents a unit cell, and t (t') represents intra-(inter-)sublattice hopping. We set the A sublattice as a center of a unit cell.

Taking the basis as $\phi(\boldsymbol{k}) = (c_{\boldsymbol{k}\uparrow A}, c_{\boldsymbol{k}\downarrow A}, c_{\boldsymbol{k}\uparrow B}, c_{\boldsymbol{k}\downarrow B})^\top$, the representation matrix of total Hamiltonian takes the form,

$$\hat{H} = \hat{H}_{\text{kin}} + \hat{H}_{\text{ASOC}} + \hat{H}_{\text{Zeeman}} = \sum_{\boldsymbol{k}} \phi^\dagger(\boldsymbol{k}) \mathcal{H}(\boldsymbol{k}) \phi(\boldsymbol{k}). \tag{2.7.9}$$

The glide symmetry playing the key role in this Chapter is

$$\hat{G} = \{M_z | \boldsymbol{a}/2 + \boldsymbol{b}/2\}. \tag{2.7.10}$$

Acting on the one-particle basis, $\hat{G}$ yields the following relationship:

$$\hat{G} \left| \boldsymbol{R}, \uparrow, A \right\rangle = i \left| R_x, R_y, -R_z, \uparrow, B \right\rangle, \tag{2.7.11}$$

$$\hat{G} \left| \boldsymbol{R}, \downarrow, A \right\rangle = -i \left| R_x, R_y, -R_z, \downarrow, B \right\rangle, \tag{2.7.12}$$

$$\hat{G} \left| \boldsymbol{R}, \uparrow, B \right\rangle = i \left| R_x + a, R_y + a, -R_z, \uparrow, A \right\rangle, \tag{2.7.13}$$

$$\hat{G} \left| \boldsymbol{R}, \downarrow, B \right\rangle = -i \left| R_x + a, R_y + a, -R_z, \downarrow, A \right\rangle. \tag{2.7.14}$$

Therefore, we represent $\hat{G}$ in this basis as,

$$\hat{G}\phi^\dagger(\boldsymbol{k})\hat{G}^{-1} = \phi^\dagger(k_x, k_y, -k_z) \begin{pmatrix} 0 & 0 & ie^{-i(k_x+k_y)a} & 0 \\ 0 & 0 & 0 & -ie^{-i(k_x+k_y)a} \\ i & 0 & 0 & 0 \\ 0 & -i & 0 & 0 \end{pmatrix} \tag{2.7.15}$$

$$= \phi^\dagger(k_x, k_y, -k_z) \begin{pmatrix} 0 & e^{-i(k_x+k_y)a} \\ 1 & 0 \end{pmatrix}_\sigma \otimes (is_z) \tag{2.7.16}$$

$$= \phi^\dagger(k_x, k_y, -k_z) \mathcal{G}(\boldsymbol{k}). \tag{2.7.17}$$

On the glide-invariant planes, $k_z = 0$ or π, we can block diagonalize the Hamiltonian with the basis diagonalizing the representation matrix of glide symmetry $\mathcal{G}(\boldsymbol{k})$,

$$U^\dagger \mathcal{H}(\boldsymbol{k}) U = \begin{pmatrix} \mathcal{H}^{\mathfrak{g}^+}(\boldsymbol{k}) & 0 \\ 0 & \mathcal{H}^{\mathfrak{g}^-}(\boldsymbol{k}) \end{pmatrix}, \tag{2.7.18}$$

$$\mathcal{H}^{\mathfrak{g}^\pm}(\boldsymbol{k}) = -2t(\cos k_x + \cos k_y) s_0 - \alpha \boldsymbol{g}(\boldsymbol{k}) \cdot \boldsymbol{s} - \left(\mu_B H \pm 4t' \cos\frac{k_x}{2} \cos\frac{k_y}{2} \delta_{k_z,0} \right) s_z. \tag{2.7.19}$$

Here, $\mathcal{H}^{\mathfrak{g}^\pm}(\boldsymbol{k})$ are the glide sector Hamiltonian. The unitary matrix U is obtained as,

$$U = \frac{1}{\sqrt{2}} \begin{pmatrix} e^{-i(k_x+k_y)a/2} & 0 & -e^{-i(k_x+k_y)a/2} & 0 \\ 0 & -e^{-i(k_x+k_y)a/2} & 0 & e^{-i(k_x+k_y)a/2} \\ 1 & 0 & 1 & 0 \\ 0 & 1 & 0 & 1 \end{pmatrix} \tag{2.7.20}$$

$$= \frac{1}{\sqrt{2}} \begin{pmatrix} e^{-i(k_x+k_y)a/2} s_z & -e^{-i(k_x+k_y)a/2} s_z \\ s_0 & s_0 \end{pmatrix}. \tag{2.7.21}$$

To demonstrate the bulk-boundary correspondence and the emergence of Majorana states in $CeRh_2As_2$, we adopt the following parameters

$$(t, t', \alpha, h, \mu) = (1.0, 0.1, 0.3, -0.1, -3.8), \tag{2.7.22}$$

in which the number of Fermi surfaces, $\#\mathrm{FS}^{\pm}_{\Gamma_i \to \Gamma_j}$ modulo 2, is equivalent to the band structure calculation for $CeRh_2As_2$. Figure 2.6 shows the Fermi surfaces of the tight-binding model on the glide-invariant planes, $k_z = 0, \pi$. The number of Fermi surfaces in each glide sector is odd at $k_z = 0$, while it is even at $k_z = \pi$, consistent with the main text.

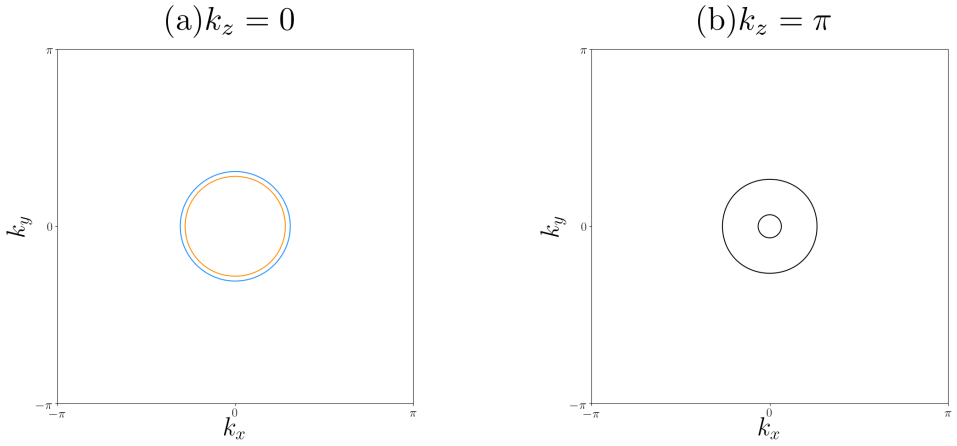

Figure 2.6: Fermi surfaces of the tight-binding model on (a) $k_z = 0$ and (b) $k_z = \pi$. (a) Orange and blue lines show the Fermi surface belonging to the glide-positive and glide-negative sector, respectively. (b) On $k_z = \pi$, the energy spectrum of each glide sector are doubly degenerate, and we show them by black lines. Thus, the number of Fermi surfaces counted for the glide $\mathbb{Z}_2$ invariants is odd on $k_z = 0$, while it is even on $k_z = \pi$.

2.7.2 Superconducting gap functions, BdG Hamiltonian, and glide sectors for each irreducible representations

Now, we discuss the superconducting order parameter. We here ignore inter-sublattice pairing for simplicity. Since the site symmetry of the Ce site is C_{4v}, spin-singlet component and spin-triplet component can locally mix, although the inversion parity can be globally defined. In the BCS state, which is the conventional even-parity state expected as the low-field phase in $CeRh_2As_2$, the gap function has the form,

$$\Delta_{\mathrm{BCS}}(\boldsymbol{k}) = \begin{pmatrix} (\psi(\boldsymbol{k}) + \boldsymbol{d}(\boldsymbol{k}) \cdot \boldsymbol{s})\, i s_y & 0 \\ 0 & (\psi(\boldsymbol{k}) - \boldsymbol{d}(\boldsymbol{k}) \cdot \boldsymbol{s})\, i s_y \end{pmatrix}_{\sigma}. \tag{2.7.23}$$

The spin-triplet component of gap functions appear with the different sign between sublattices in accordance with the sign of ASOC. As the inversion operation $\hat{I}$ interchanges sublattices and flips the wave number $\boldsymbol{k}$, the space inversion parity is globally even. On the other hand, in the PDW state [1], the spin-singlet (spin-triplet) gap functions have different (same) sign,

$$\Delta_{\rm PDW}(\boldsymbol{k}) = \begin{pmatrix} (\psi(\boldsymbol{k}) + \boldsymbol{d}(\boldsymbol{k})\cdot\boldsymbol{s})\, is_y & 0 \\ 0 & (-\psi(\boldsymbol{k}) + \boldsymbol{d}(\boldsymbol{k})\cdot\boldsymbol{s})\, is_y \end{pmatrix}_\sigma , \tag{2.7.24}$$

and therefore, the space inversion parity is globally odd even when the spin-singlet pairing is dominant. The even-odd parity transition between the BCS and PDW states has been theoretically proposed [1]. Because the odd-parity PDW state is more robust against the magnetic field than the BCS state, the two phases appear in the H-T phase diagram. The low-field phase is the BCS state, while the high-field phase is the PDW state, as illustrated in the main text [Fig. 1(b)].

The gap functions are classified by the global point group symmetry D_{4h}, and the odd-parity PDW state belongs to one of the odd-parity irreducible representations. In this work we focus on the one-dimensional representations, A_{1u}, A_{2u}, B_{1u}, B_{2u}, as we mention in the main text. Here, we describe the gap functions with using the basis functions as $\psi(\boldsymbol{k}) = \psi_0 \times$(basis) and $\boldsymbol{d}(\boldsymbol{k}) = d_0 \times$ (basis). The basis are shown in Table. 3.2.

Table 2.3: Superconducting gap functions classified by the irreducible representations of D_{4h} point group.

Irreducible representation	$\psi(\boldsymbol{k})i\sigma_y/\psi_0$	$[\boldsymbol{d}(\boldsymbol{k})\cdot\boldsymbol{\sigma}]i\sigma_y/d_0$
A_{1u}	$\sin k_x \sin k_y (\cos k_x - \cos k_y)$	$\sin k_x \hat{\boldsymbol{x}} + \sin k_y \hat{\boldsymbol{y}}$
A_{2u}	1	$\sin k_y \hat{\boldsymbol{x}} - \sin k_x \hat{\boldsymbol{y}}$
B_{1u}	$\sin k_x \sin k_y$	$\sin k_x \hat{\boldsymbol{x}} - \sin k_y \hat{\boldsymbol{y}}$
B_{2u}	$\cos k_x - \cos k_y$	$\sin k_y \hat{\boldsymbol{x}} + \sin k_x \hat{\boldsymbol{y}}$

We perform the unitary transformation for the BdG Hamiltonian on the glide-invariant planes with

$$U_{\rm BdG} = \frac{1}{\sqrt{2}} \begin{pmatrix} e^{-i(k_x+k_y)a/2}s_z & 0 & -e^{-i(k_x+k_y)a/2}s_z & 0 \\ s_0 & 0 & s_0 & 0 \\ 0 & e^{-i(k_x+k_y)a/2}s_z & 0 & -e^{-i(k_x+k_y)a/2}s_z \\ 0 & s_0 & 0 & s_0 \end{pmatrix}, \tag{2.7.25}$$

(2.7.26)

and obtain the block-diagonalized (glide sector) Hamiltonian $\mathcal{H}^{\mathfrak{g}^\pm}_{\rm BdG}(\boldsymbol{k})$ as in the normal state,

$$U^\dagger_{\rm BdG}\mathcal{H}_{\rm BdG}(\boldsymbol{k})U_{\rm BdG} = \begin{pmatrix} \mathcal{H}^{\mathfrak{g}^+}_{\rm BdG}(\boldsymbol{k}) & 0 \\ 0 & \mathcal{H}^{\mathfrak{g}^-}_{\rm BdG}(\boldsymbol{k}) \end{pmatrix}_\sigma, \tag{2.7.27}$$

$$\mathcal{H}^{\mathfrak{g}^\pm}_{\rm BdG}(\boldsymbol{k}) = \begin{pmatrix} \mathcal{H}^{\mathfrak{g}^\pm}(\boldsymbol{k}) & \Delta^{\mathfrak{g}}(\boldsymbol{k}) \\ (\Delta^{\mathfrak{g}}(\boldsymbol{k}))^\dagger & \left(-\mathcal{H}^{\mathfrak{g}^\pm}(-\boldsymbol{k})\right)^\top \end{pmatrix}, \tag{2.7.28}$$

$$\mathcal{H}^{\mathfrak{g}^\pm}(\boldsymbol{k}) = -2t(\cos k_x + \cos k_y)s_0 - \alpha \boldsymbol{g}(\boldsymbol{k})\cdot\boldsymbol{s} - \left(\mu_B H \pm 4t' \cos\frac{k_x}{2}\cos\frac{k_y}{2}\,\delta_{k_z,0}\right)\sigma_z, \tag{2.7.29}$$

$$\Delta^{\mathfrak{g}}(\boldsymbol{k}) = (-\psi(\boldsymbol{k}) + \boldsymbol{d}(\boldsymbol{k})\cdot\boldsymbol{s})\, i s_y. \tag{2.7.30}$$

Since Majorana states appear at surfaces preserving the glide symmetry, which is generated by $\boldsymbol{a}+\boldsymbol{b}$ and $\boldsymbol{c}$, the $(\bar{1}10)$ surface is the host of Majorana surface states. To calculate the energy spectrum in the open boundary condition, we retake primitive translation vector as $\boldsymbol{a}' = \boldsymbol{a}+\boldsymbol{b} = (a,a,0)$, $\boldsymbol{b}' = \boldsymbol{b} = (0,a,0)$, and $\boldsymbol{c}' = \boldsymbol{c} = (0,0,c)$. The volume of a unit cell does not change under this operation,

$$V = |(\boldsymbol{a}\times\boldsymbol{b})\cdot\boldsymbol{c}| = |(\boldsymbol{a}'\times\boldsymbol{b}')\cdot\boldsymbol{c}'|. \tag{2.7.31}$$

Correspondingly, the wave numbers are $k_{a'} = \boldsymbol{k}\cdot\boldsymbol{a}' = k_x + k_y$, $k_{b'} = \boldsymbol{k}\cdot\boldsymbol{b}' = k_y$, and $k_{c'} = \boldsymbol{k}\cdot\boldsymbol{c}' = k_z$. We conduct calculations in the effective cubic Brillouin zone ($-\pi < k_{a'}, k_{b'}, k_{c'} \le \pi$), with assuming the open boundary condition for $k_{b'}$ though periodic boundary condition for $k_{a'}$. We take $L_{b'} = 64$ and $L_{a'} = 256$ for the system size.

2.8 Majorana states on glide-symmetric surfaces

In this section, we present the surface state calculations obtained by diagonalizing the BdG Hamiltonian, as introduced in the previous section, under open boundary conditions. Figure 2.7 displays the $(\bar{1}10)$ and $(1\bar{1}0)$ surface states at $k_z = 0, \pi$ across all odd-parity and glide-odd irreducible representations. Specifically, for the $k_z = 0$ plane, we differentiate the glide sectors using color coding: orange lines represent the glide-positive sector, while blue lines denote the glide-negative sector. Conversely, for $k_z = \pi$, we only depict the glide-positive sector, as it is degenerate with the glide-negative sector.

All our results align with the theoretical formula that connects Fermi surface topology to the glide $\mathbb{Z}_2$ invariants. In Figs. 2.7(a)-(d), we observe a unique, non-degenerate Majorana state at zero energy in each glide sector, specifically at $k_{a'} = 0$. This finding correlates with the odd number of $\#\mathrm{FS}^{\pm}_{\Gamma\to M}$ shown in Fig. 2.6(a) and the nontrivial $\mathbb{Z}_2$ invariants on the $k_z = 0$ plane. Conversely, Figs. 2.7(e), (f), and (h) display an energy gap in the surface spectrum at $k_z = \pi$. This observation is in line with the trivial glide $\mathbb{Z}_2$ invariants, as inferred from the even $\#\mathrm{FS}^{\pm}_{Z\to A}$ count [Fig. 2.6(b)]. Despite Fig. 2.7(g) showing zero modes at $k_{a'} = 0$,

these zero-energy states do not constitute stable Majorana states due to the presence of two modes for each sector and boundary. This observation too is consistent with the trivial glide $\mathbb{Z}_2$ invariants.

From the results in this section, our statements on the topological superconductivity and Majorana states have been verified based on the minimal tight-binding model study. We stress that the arguments do not essentially depend on the details of superconducting order parameter as well as the electronic structure, unless the topology of Fermi surfaces is altered.

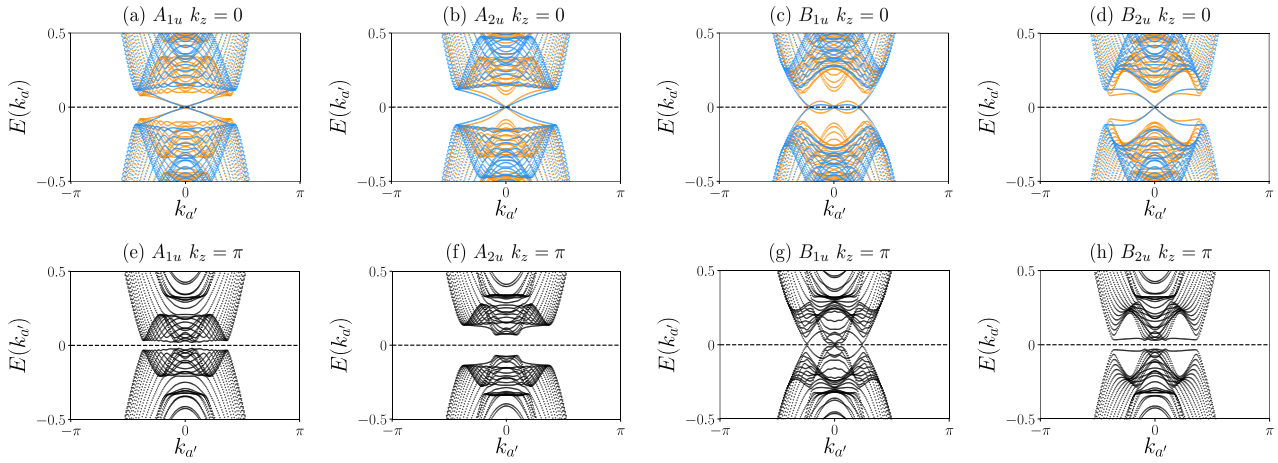

Figure 2.7: $(\bar{1}10)$ and $(1\bar{1}0)$ surface states of the tight-binding BdG Hamiltonian on (a-d) $k_z = 0$ and (e-f) $k_z = \pi$. Symmetry of superconducting gap functions is (a,e) A_{1u}, (b,f) A_{2u}, (c,g) B_{1u}, and (d,h) B_{2u} representations. We take $\psi_0 = 0.1$, $d_0 = 0.05$ for the A_{2u} representation while $\psi_0 = 0.3$, $d_0 = 0.2$ for the others. The orange and blue lines represent the glide-positive and glide-negative sectors, respectively. For $k_z = \pi$, only the spectrum of glide-positive sector is shown because it is equivalent to the glide-negative sector.

2.9 Summary and conclusion

In this chapter, we present a theoretical investigation into the electronic structure and topological superconductivity of the recently discovered heavy-fermion superconductor $CeRh_2As_2$. Initially, we utilized group theory to elucidate the algebra of symmetry operations in the Bloch representation. This allowed us to decompose the Hilbert space on the glide-invariant planes at $k_z = 0$ and $k_z = \pi$ into distinct glide sectors. Considering the PDW state in the high-field superconducting phase, as proposed, we derived a Fermi-surface formula for the $\mathbb{Z}_2$ invariants. These invariants specify the TCSC that is protected by nonsymmorphic glide symmetry. Furthermore, we performed first-principles calculations to analyze $CeRh_2As_2$'s

electronic structure. By evaluating the $\mathbb{Z}_2$ invariants, we identified TCSC originating from the heavy-fermion bands of Ce $4f$ electrons hybridized with conduction electrons. The emergence of Majorana fermions on surfaces preserving the glide symmetry was demonstrated using a tight-binding model. This work positions $CeRh_2As_2$ as a novel class of topological superconductors for two primary reasons: (1) The topological superconductivity observed does not require spin-triplet pairing or a topological band structure. (2) Its topological nature is safeguarded by nonsymmorphic symmetry, unique in that it lacks an equivalent in continuous systems [127].

Chapter 3

Even-odd parity transition in strongly correlated locally noncentrosymmetric superconductors : An application to $CeRh_2As_2$

The quest for odd-parity superconductors is pivotal in the design of topological materials, a topic extensively discussed in literature [26, 27, 28, 29]. According to Fermi statistics and within the framework of the Bardeen, Cooper, and Schrieffer (BCS) theory [128], odd-parity superconductors are generally categorized as spin-triplet superconductors. This BCS theory has been instrumental in explaining a wide range of superconductivity phenomena. In the realm of topological science, the constraints on Cooper pairs have reignited interest in relatively rare spin-triplet superconductors. Examples include UPt_3 [68, 78, 86, 96], UCoGe [87, 129, 130], and UTe_2 [99, 100, 123, 131]. However, it is important to note that some internal degrees of freedom of Cooper pairs are not accounted for in the conventional BCS theory.

Recent studies have increasingly focused on local noncentrosymmetry in superconductors, bringing to light the significance of the sublattice degree of freedom in Cooper pairs [1, 18, 81, 86, 115, 117, 118, 119, 120, 121, 122, 132, 133, 134, 135]. Intriguingly, this research has revealed that sublattice antisymmetric Cooper pairing is permissible, resulting in odd-parity superconducting states without requiring spin-triplet pairs. Consequently, the sublattice degree of freedom offers a novel approach to designing topological odd-parity superconductors through conventional spin-singlet pairing mechanisms [81, 127]. In the context of locally noncentrosymmetric superconductors under high magnetic fields, theoretical predictions suggest the thermodynamic stability of a sublattice antisymmetric superconducting state, referred to as the pair-density-wave (PDW) state [1].

The discovery of two distinct superconducting phases in the H-T phase diagram of

$CeRh_2As_2$ has heightened interest in the sublattice degree of freedom in superconductors, as evidenced by numerous studies [2, 3, 7, 8, 15, 16, 19, 101, 102, 103, 104, 127, 136, 137, 138]. The unique two-sublattice crystalline structure of $CeRh_2As_2$ results in local inversion symmetry breaking at the Ce sites while maintaining global symmetry [2]. The striking similarity between the experimental phase diagrams and those predicted by weak-coupling theory [1, 2] strongly indicates the pivotal role of local inversion symmetry breaking in $CeRh_2As_2$. This observation has led to the interpretation of the two superconducting phases as a manifestation of an even-odd parity transition within the superconducting state [2, 8].

Contrary to the earlier discussions, two critical issues concerning $CeRh_2As_2$ warrant further examination. Firstly, the exact microscopic mechanism underlying the superconductivity in $CeRh_2As_2$ remains an open question. This chapter delves into the hypothesis that unconventional superconductivity in this material may be mediated by quantum critical fluctuations. Secondly, the observed parity transition field in $CeRh_2As_2$ notably surpasses the Pauli-Clogston-Chandrasekhar limit, exceeding the predictions of weak-coupling theory by a factor of five [1, 2]. While two scenarios have been previously proposed within the framework of weak-coupling theory [104, 137], our approach seeks to shed light on these discrepancies by exploring an intrinsic phase diagram pertinent to strongly correlated, locally noncentrosymmetric superconductors.

To address the aforementioned challenges, we concentrate on the electronic correlation effects in Ce f-electrons, which exhibit a localized character. The significantly large electronic specific heat coefficient, $\gamma \sim 1000, \mathrm{mJ/mol\,K^2}$, is indicative of heavy-fermion bands in proximity to the Fermi level in $CeRh_2As_2$. Additionally, the observed non-Fermi-liquid behaviors are suggestive of quantum criticality within this material [2, 7, 16]. These experimental findings underscore the profound influence of Coulomb interactions on the electronic state of $CeRh_2As_2$. Consequently, there is a burgeoning interest in theoretical investigations of strong correlation effects, especially in locally noncentrosymmetric superconductors.

In this chapter, we embark on an in-depth analysis of quantum critical multipole fluctuations, their role in superconductivity, and the superconducting phase diagrams specific to locally noncentrosymmetric, strongly correlated electron systems. For this purpose, we employ the fluctuation exchange (FLEX) approximation, known for effectively replicating the critical behaviors as outlined in self-consistent renormalization theory [139]. The FLEX approach intricately links the Green function and self-energy, thereby incorporating vital factors such as retardation effects, quasi-particle scattering, and internal fields. We then compare our theoretical findings with the superconducting phase diagrams of $CeRh_2As_2$ to discuss the origins of superconductivity in this material. Through this comparison, we unveil XY-type antiferromagnetic fluctuations that align with nuclear magnetic resonance (NMR) observations [16]. Furthermore, our results indicate superconductivity predominantly characterized by $d_{x^2-y^2}$-wave pairing. Significantly, the enhanced parity transition field observed in our study offers a resolution to the previously identified discrepancies in the phase diagram

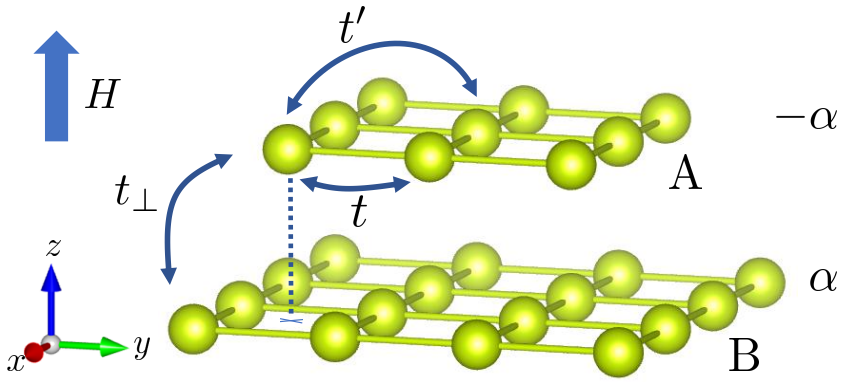

Figure 3.1: Schematic figure of the bilayer Rashba-Hubbard model. Yellow circles represent the Ce atoms of $CeRh_2As_2$. We introduce first- and second-neighbor intra-layer hopping integrals. We also introduce an inter-layer hopping integral as $t_\perp$. The staggered Rashba-type antisymmetric spin-orbit coupling is included in the model as it arises from the asymmetric potential by Rh_2As_2 layers. The magnetic field is applied parallel to the z axis.

of $CeRh_2As_2$.

3.1 Bilayer Rashba-Hubbard model

We focus on the low-energy coherent heavy-fermion band and construct the bilayer Rashba-Hubbard model, in which Coulomb correlation and spin-orbit coupling are taken into account [140, 141]. Note that all parameters of our model are renormalized through the Kondo effect. The model is given by

$$\hat{H} = \sum_{\boldsymbol{k}} \varphi^\dagger(\boldsymbol{k}) \mathcal{H}_0(\boldsymbol{k}) \varphi(\boldsymbol{k}) + U \sum_{i,\sigma} n_{i\uparrow\sigma} n_{i\downarrow\sigma}, \tag{3.1.1}$$

where U is the on-site Coulomb repulsion, $\mathcal{H}_0(\boldsymbol{k}) = \varepsilon(\boldsymbol{k}) s_0 \otimes \sigma_0 + \alpha \boldsymbol{g}(\boldsymbol{k}) \cdot \boldsymbol{s} \otimes \sigma_z - \mu_B H s_z \otimes \sigma_0 + \tilde{t}_\perp(\boldsymbol{k}) s_0 \otimes \sigma_+ + \tilde{t}_\perp(-\boldsymbol{k}) s_0 \otimes \sigma_-$, $\varphi(\boldsymbol{k}) = (c_{\boldsymbol{k}\uparrow\mathrm{A}}, c_{\boldsymbol{k}\downarrow\mathrm{A}}, c_{\boldsymbol{k}\uparrow\mathrm{B}}, c_{\boldsymbol{k}\downarrow\mathrm{B}})^\top$, and $c_{\boldsymbol{k}s\sigma}$ ($c^\dagger_{\boldsymbol{k}s\sigma}$) is an annihilation (creation) operator for an electron with momentum $\boldsymbol{k}$, spin s, and sublattice $\sigma \in \{\mathrm{A}, \mathrm{B}\}$ (Fig. 3.1). Here, s_μ and σ_μ consisting of the 2×2 unit matrix and three Pauli matrices represent spin and sublattice degrees of freedom, respectively.[1] The first term of $\mathcal{H}_0$ represents intra-layer hopping including the chemical potential and is given by $\varepsilon(\boldsymbol{k}) = -2t(\cos k_x + \cos k_y) + 4t' \cos k_x \cos k_y - \mu$. The vector $\boldsymbol{g}(\boldsymbol{k})$ describes the Rashba-type antisymmetric spin-orbit coupling given by $\boldsymbol{g}(\boldsymbol{k}) = [-\partial\varepsilon(\boldsymbol{k})/\partial k_y, \partial\varepsilon(\boldsymbol{k})/\partial k_x, 0]$, and H represents the Zeeman magnetic field parallel to the z-axis. The last two terms of $\mathcal{H}_0$ describe

[1] μ runs over $\{0, x, y, z\}$, and $\sigma_\pm$ are given by $(\sigma_x \pm i\sigma_y)/2$.

inter-layer hopping given as $\tilde{t}_\perp(\boldsymbol{k}) = t_\perp(1+e^{-ik_x})(1+e^{-ik_y})$. This model is a straightforward extension of the Rashba-Hubbard model for globally inversion-asymmetric strongly correlated electron systems [109, 114, 142, 143, 144, 145, 146, 147, 148, 149, 150, 151, 152]. Hereafter, we set $t' = 0.3$, $t_\perp = 0.1$, $\mu_{\rm B} = 1$, and $U = 3.9$ with a unit of energy $t = 1$ and determine the chemical potential so that the electron density per site n is 0.85. In the present numerical study, we use 64×64 $\boldsymbol{k}$-meshes, and 16384, 8192, or 4096 Matsubara frequencies for $T = 0.004$, $0.004 < T < 0.01$, or $0.01 \leq T$, respectively. By comparing with the quantum Monte Carlo method, the FLEX approximation was confirmed as a reliable method within the intermediate-coupling region in which the Coulomb interaction U is smaller than half of the bandwidth W, namely, the condition for justification of the FLEX approximation is $U/W \lessapprox 0.5$ [153, 154, 155, 156, 157]. Our choice of model parameters satisfies this condition and the FLEX approximation is expected to give a good description of strongly correlated superconductors in this case.

3.2 Self-consistent condition for fluctuation exchange approximation

The noninteracting Green functions for $U = 0$ are expressed by the 4×4 matrix form in the spin and sublattice basis,

$$G^{(0)}(\boldsymbol{k}, i\omega_n) = \left(i\omega_n s_0 \otimes \sigma_0 - \mathcal{H}_0(\boldsymbol{k})\right)^{-1}, \tag{3.2.1}$$

where $\omega_n = (2n+1)\pi T$ are fermionic Matsubara frequencies. In the interacting case $U \neq 0$, the dressed Green functions contain a self-energy, $\Sigma(\boldsymbol{k}, i\omega_n)$,

$$G(\boldsymbol{k}, i\omega_n) = \left(i\omega_n s_0 \otimes \sigma_0 - \mathcal{H}_0(\boldsymbol{k}) - \Sigma(\boldsymbol{k}, i\omega_n)\right)^{-1}. \tag{3.2.2}$$

Within the FLEX approximation, the self-energy is expressed with use of an effective interaction, $\Gamma^n(\boldsymbol{k}, i\nu_n)$, as

$$\Sigma_{\xi\xi'}(\boldsymbol{k}, i\omega_n) = \frac{T}{N}\sum_{\boldsymbol{q}, i\nu_n} \Gamma^n_{\xi\xi_1\xi'\xi_2}(\boldsymbol{q}, i\nu_n) G_{\xi_1\xi_2}(\boldsymbol{k}-\boldsymbol{q}, i\omega_n - i\nu_n), \tag{3.2.3}$$

and the effective interaction is given by

$$\Gamma^n_{\xi_1\xi_2\xi_3\xi_4}(\boldsymbol{k}, i\nu_n) = U_{\xi_1\xi_2\xi_5\xi_6}\left(\chi_{\xi_5\xi_6\xi_7\xi_8}(\boldsymbol{k}, i\nu_n) - \frac{1}{2}\chi^{(0)}_{\xi_5\xi_6\xi_7\xi_8}(\boldsymbol{k}, i\nu_n)\right) U_{\xi_7\xi_8\xi_3\xi_4}, \tag{3.2.4}$$

where $U_{\xi_1\xi_2\xi_3\xi_4}$ is bare interaction tensor which satisfies the following relation

$$\sum_{\xi_1\xi_2\xi_3\xi_4} U_{\xi_1\xi_2\xi_3\xi_4} c^\dagger_{\xi_1} c_{\xi_2} c_{\xi_3} c^\dagger_{\xi_4} = U\sum_{i,\sigma} n_{i\uparrow\sigma} n_{i\downarrow\sigma}, \tag{3.2.5}$$

$$U_{\xi_1\xi_2\xi_3\xi_4} = \delta_{\sigma_1,\sigma_2}\delta_{\sigma_2,\sigma_3}\delta_{\sigma_3,\sigma_4} U_{s_1 s_2 s_3 s_4}, \tag{3.2.6}$$

$$U_{\uparrow\downarrow\uparrow\downarrow} = U_{\downarrow\uparrow\downarrow\uparrow} = -U_{\uparrow\uparrow\downarrow\downarrow} = -U_{\downarrow\downarrow\uparrow\uparrow} = U, \tag{3.2.7}$$

and $i\nu_n$ are bosonic Matsubara frequencies. Here, $\chi(\boldsymbol{k}, i\nu_n)$ is the generalized susceptibility. We introduce the bare susceptibility

$$\chi^{(0)}_{\xi_1\xi_2\xi_3\xi_4}(\boldsymbol{q}, i\nu_n) = -\frac{T}{N}\sum_{\boldsymbol{k}, i\omega_n} G_{\xi_1\xi_3}(\boldsymbol{k}, i\omega_n)G_{\xi_4\xi_2}(\boldsymbol{k}-\boldsymbol{q}, i\omega_n - i\nu_n), \tag{3.2.8}$$

and compute the generalized susceptibility by

$$\chi_{\xi_1\xi_2\xi_3\xi_4}(\boldsymbol{q}, i\nu_n) = \chi^{(0)}_{\xi_1\xi_2\xi_3\xi_4}(\boldsymbol{q}, i\nu_n) + \chi^{(0)}_{\xi_1\xi_2\xi_5\xi_6}(\boldsymbol{q}, i\nu_n)U_{\xi_5\xi_6\xi_7\xi_8}\chi_{\xi_7\xi_8\xi_3\xi_4}(\boldsymbol{q}, i\nu_n). \tag{3.2.9}$$

According to Eqs. (3.2.2)-(3.2.9), G, Σ, Γ^n, $\chi^{(0)}$, and χ depend on each other, and therefore, we self-consistently determine these functions.

For functions with fermionic Matsubara frequencies $A(\boldsymbol{q}, i\omega_n)$, the static limit $A(\boldsymbol{q}, 0)$ is evaluated by an approximation justified at low temperatures,

$$A(\boldsymbol{q}, 0) \simeq \frac{A(\boldsymbol{q}, i\pi T) + A(\boldsymbol{q}, -i\pi T)}{2}. \tag{3.2.10}$$

For the analyze of superconducting phase transition, particle-particle channel irreducible vertex function Γ^a is needed. Γ^a is obtained by

$$\Gamma^a_{\xi_1\xi_2\xi_3\xi_4}(\boldsymbol{q}, i\nu_n) = U_{\xi_1\xi_2\xi_3\xi_4}/2 + U_{\xi_1\xi_2\xi_5\xi_6}\chi_{\xi_5\xi_6\xi_7\xi_8}(\boldsymbol{q}, i\nu_n)U_{\xi_7\xi_8\xi_3\xi_4}. \tag{3.2.11}$$

3.3 Multipole susceptibility

Initially, our discussion centers on quantum critical multipole fluctuations. The dynamical susceptibility tensor in this context is represented by the generalized susceptibility, defined as:

$$\chi_{\hat{\mathcal{O}}}(\boldsymbol{q}, i\nu_n) = \sum_{\xi_1\xi_2\xi_3\xi_4} \hat{\mathcal{O}}_{\xi_1\xi_2}\chi_{\xi_2\xi_1\xi_3\xi_4}(\boldsymbol{q}, i\nu_n)\hat{\mathcal{O}}_{\xi_3\xi_4}, \tag{3.3.1}$$

where $i\nu_n$ denote the bosonic Matsubara frequencies and ξ, in a shortened form, represents $\xi = (s, \sigma)$.

In this framework, the operators $\hat{\mathcal{O}}$ are identified as (extended) multipole operators, such as $\hat{\mathcal{O}} = \hat{s} \otimes \hat{\sigma}$ [158, 159, 160]. These are classified into even-parity (odd-parity) multipoles corresponding to $\hat{\sigma}_0, \hat{\sigma}_x$ ($\hat{\sigma}_y, \hat{\sigma}_z$). Table 3.1 provides a comprehensive classification of these multipole operators in our system. For the purpose of normalization, we follow the convention $\mathrm{tr}\left[\hat{\mathcal{O}}^\dagger\hat{\mathcal{O}}\right] = 1$. Consequently, the operators are expressed in terms of Pauli matrices as $\hat{s}_\mu = s_\mu/\sqrt{2}$ and $\hat{\sigma}_\mu = \sigma_\mu/\sqrt{2}$.

In Fig. 4.1(a), we present the magnetic field's influence on the maximum values of both transverse and longitudinal magnetic susceptibilities. It is observed that while the transverse

Table 3.1: Classification of the multipole operators in the bilayer Rashba-Hubbard model. Here, $\hat{s}_\pm = (\hat{s}_x \pm i\hat{s}_y)/\sqrt{2}$ are ladder operators for spin. E (O) represents the even-parity (odd-parity) multipole operators. C, L, and T represent charge, longitudinal spin, and transverse spin operators, respectively. $\hat{\sigma}_0$ and $\hat{\sigma}_z$ ($\hat{\sigma}_x$ and $\hat{\sigma}_y$) are intrasublattice (intersublattice) operators.

$\hat{\mathcal{O}}$	$\hat{\sigma}_0$	$\hat{\sigma}_x$	$\hat{\sigma}_y$	$\hat{\sigma}_z$
$\hat{s}_0$	E C intra	E C inter	O C inter	O C intra
$\hat{s}_z$	E L intra	E L inter	O L inter	O L intra
$\hat{s}_\pm$	E T intra	E T inter	O T inter	O T intra

susceptibility increases with the magnetic field, the longitudinal susceptibility shows a decrease. Notably, the even-parity magnetic multipole fluctuation, represented by $\boldsymbol{s} \otimes \sigma_0$, and the odd-parity magnetic multipole fluctuation, corresponding to $\boldsymbol{s} \otimes \sigma_z$, are nearly degenerate. However, a slight preference for the odd-parity multipole is evident. The susceptibilities of other multipoles are found to be negligibly small in comparison. From Fig. 4.1(b), both transverse and longitudinal magnetic susceptibilities exhibit peak structures around the antiferromagnetic wave vector $\boldsymbol{Q} = (\pi, \pi)$. This pattern suggests the development of antiferromagnetic spin fluctuations in the system. Importantly, the momentum dependence of these susceptibilities appears to be unaffected by the magnetic field. Based on these observations, we postulate a predominant XY-type antiferromagnetic fluctuation,[2] aligning with NMR measurements conducted on $CeRh_2As_2$ [16]. Furthermore, we have verified that the behavior of the multipole susceptibility remains qualitatively consistent across different strengths of spin-orbit coupling, denoted as $\alpha/t_\perp$.

3.4 Superconductivity

To investigate superconductivity, we adopt the linearized Éliashberg equation which is given by

$$\lambda \Delta_{\xi\xi'}(k) = \frac{T}{N} \sum_{k'} \Gamma^a_{\xi\xi_1\xi_2\xi'}(k-k') F_{\xi_1\xi_2}(k), \tag{3.4.1}$$

$$F_{\xi_1\xi_2}(k) = G_{\xi_1\xi_3}(k') \Delta_{\xi_3\xi_4}(k') G_{\xi_2\xi_4}(-k'), \tag{3.4.2}$$

where Δ is the gap function and Γ^a is the particle-particle channel irreducible vertex function. Here, we adopted abbreviated notation $k = (\boldsymbol{k}, i\omega_n)$. With the power method, we

[2]The term 'XY-type fluctuation' indicates that transverse fluctuations are more prominent than longitudinal ones in the paramagnetic state.

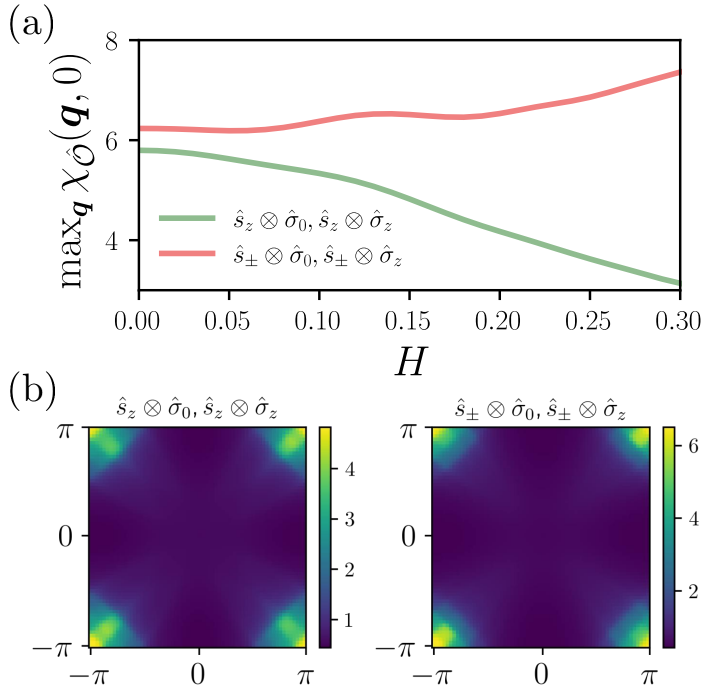

Figure 3.2: (a) The magnetic field dependence of static multipole fluctuations. The maxima of the longitudinal and transverse magnetic susceptibilities are shown. Note that the even-parity and odd-parity multipole fluctuations are nearly degenerate. We assume $\alpha/t_\perp = 2$ and $T = 0.01$. (b) The momentum dependence of longitudinal magnetic susceptibility (left) and transverse magnetic susceptibility (right) at $H = 0.15$.

numerically evaluate λ, eigenvalues of the linearized Éliashberg equation and determine the critical temperature T_c from the criterion $\lambda = 1$.

The crystal structure of CeRh2As2 belongs to the space group $P4/nmm$ (No.129), leading to the D_{4h} point group classification. However, when a magnetic field is applied parallel to the z axis, certain symmetry operations become forbidden, resulting in a reduction of the point group to C_{4h}. Consequently, the superconducting gap functions of $CeRh_2As_2$ are categorized based on the irreducible representations of the C_{4h} group. To describe these gap functions, we use a conventional notation that separates them into spin-singlet and spin-triplet components for both intrasublattice and intersublattice pairing channels:

$$\Delta^{\sigma\sigma'}(\boldsymbol{k}) = \{\psi^{\sigma\sigma'}(\boldsymbol{k}) + \boldsymbol{d}^{\sigma\sigma'}(\boldsymbol{k}) \cdot \boldsymbol{s}\} i s_y, \tag{3.4.3}$$

where $\psi^{\mathrm{AA}}(\boldsymbol{k})$ and $\psi^{\mathrm{AB}}(\boldsymbol{k})$ denote the intrasublattice and intersublattice spin-singlet order parameters, respectively. Similarly, $\boldsymbol{d}^{\mathrm{AA}}(\boldsymbol{k})$ and $\boldsymbol{d}^{\mathrm{AB}}(\boldsymbol{k})$ represent the corresponding spin-triplet order parameters. It is important to note that, in our calculations, the order parameters associated with intersublattice pairing are found to be negligibly small. For a comprehensive understanding, we have summarized the basis functions of the intrasublattice order parameters corresponding to each irreducible representation of C_{4h} in Table 3.2. Note that, In our system, intrasublattice pairing is equivalent to intra-layer pairing, while intersublattice pairing corresponds to inter-layer pairing.

Table 3.2: The basis functions for the intrasublattice superconducting order parameter. IR represents the irreducible representations of the point group C_{4h}. We take into account the time-reversal symmetry breaking under the magnetic field, and the degeneracy of the $E_{g/u}$ states is lifted. Thus, we distinguish them as $E^1_{g/u}$ and $E^2_{g/u}$. Note that the spin-singlet component $\psi(\boldsymbol{k})$ and spin-triplet in-plane component $d_{x,y}(\boldsymbol{k})$ for the E representations are prohibited due to the C_2^z rotation symmetry.

IR	$\psi(\boldsymbol{k})$	$\boldsymbol{d}(\boldsymbol{k})$
A_g, A_u	1, $k_x k_y \left(k_x^2 - k_y^2\right)$	$k_x\hat{\boldsymbol{x}} + k_y\hat{\boldsymbol{y}}$, $k_y\hat{\boldsymbol{x}} - k_x\hat{\boldsymbol{y}}$
B_g, B_u	$k_x k_y$, $k_x^2 - k_y^2$	$k_x\hat{\boldsymbol{x}} - k_y\hat{\boldsymbol{y}}$, $k_y\hat{\boldsymbol{x}} + k_x\hat{\boldsymbol{y}}$
E^1_g, E^1_u	0	$(k_x + ik_y)\,\hat{\boldsymbol{z}}$
E^2_g, E^2_u	0	$(k_x - ik_y)\,\hat{\boldsymbol{z}}$

In Fig. 4.2(a), we illustrate the eigenvalues of the Éliashberg equation corresponding to each irreducible representation. Notably, the representations B_g and B_u emerge as the dominant ones. As evidenced by the momentum dependence depicted in Fig. 4.2(b), both these states predominantly exhibit spin-singlet $d_{x^2-y^2}$-wave pairing. Additionally, they possess a spin-triplet subdominant pairing component characterized by p-wave symmetry. These unconventional Cooper pairings are primarily stabilized by the antiferromagnetic fluctuations

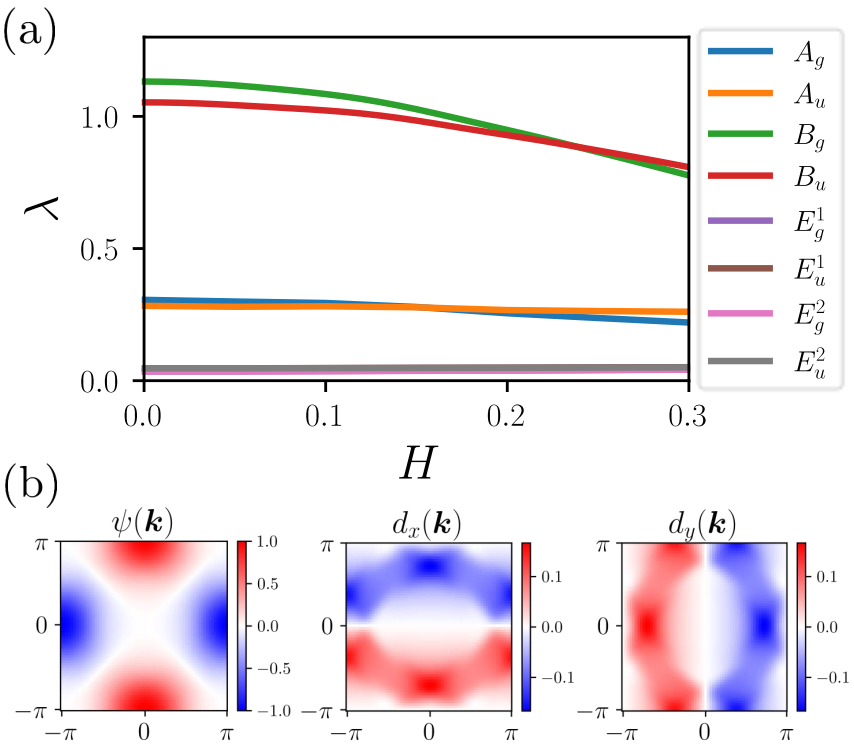

Figure 3.3: (a) The magnetic field dependence of eigenvalues of the Éliashberg equation for each irreducible representation. We assume $\alpha/t_\perp = 2$ and $T = 0.01$. (b) The momentum dependence of intra-sublattice spin-singlet and spin-triplet gap functions, $\psi^{\mathrm{AA}}(\boldsymbol{k})$ and $\boldsymbol{d}^{\mathrm{AA}}(\boldsymbol{k})$, of the B_g representation for $H = 0.15$. Note that $d_z^{\sigma\sigma}(\boldsymbol{k}) = 0$. Results for the B_u representation are almost the same as the figures.

and the presence of spin-orbit coupling. Remarkably, their stability remains largely unaffected by the application of a magnetic field.

The momentum dependence of the gap functions is similar for both B_g and B_u representations; however, their distinct sublattice structures set them apart. In the even-parity B_g representation, the spin-singlet gap function exhibits the same sign on both sublattices A and B, as demonstrated by $\psi^{\mathrm{AA}}(\boldsymbol{k}) = \psi^{\mathrm{BB}}(\boldsymbol{k})$. Conversely, the spin-triplet gap function shows opposite signs, as indicated by $\boldsymbol{d}^{\mathrm{AA}}(\boldsymbol{k}) = -\boldsymbol{d}^{\mathrm{BB}}(\boldsymbol{k})$. In contrast, the odd-parity B_u representation displays opposite signs for the spin-singlet gap function between the sublattices, $\psi^{\mathrm{AA}}(\boldsymbol{k}) = -\psi^{\mathrm{BB}}(\boldsymbol{k})$, while the spin-triplet gap function maintains the same sign, $\boldsymbol{d}^{\mathrm{AA}}(\boldsymbol{k}) = \boldsymbol{d}^{\mathrm{BB}}(\boldsymbol{k})$. These distinctions imply that the B_g and B_u representations correspond to the BCS and PDW states, respectively, as predicted in weak-coupling theory [1]. As illustrated in Fig 4.2(a), the eigenvalues of the 'Eliashberg equation for both representations diminish under the influence of a magnetic field, a result of the Pauli depairing effect. No-

tably, the B_u state demonstrates greater robustness against the magnetic field compared to the B_g state. Consequently, at a magnetic field strength of $H = 0.24$, a parity transition occurs from the even-parity B_g state to the odd-parity B_u state. This transition can be interpreted through the intrinsic magnetic response of these states, where the B_g state is limited by Pauli susceptibility, but the B_u state largely circumvents Pauli limiting as the magnetic susceptibility remains unchanged through the superconducting transition [18, 122].

3.5 Phase diagram

In this section, we analyze the H-T phase diagrams of the bilayer Rashba-Hubbard model, as depicted in Figs. 4.4(a)-(d). These phase diagrams correspond to different values of the parameter $\alpha/t_\perp$, a key control variable for local noncentrosymmetry, as for Maruyama *et al.* [18]. We consider cases where $\alpha/t_\perp = 0$, 1, 2, and 3. It's notable that the case $\alpha/t_\perp = 0$ represents the bilayer system without spin-orbit coupling, whereas at $\alpha/t_\perp = \infty$, the system effectively behaves like a collection of monolayer systems with Rashba-type spin-orbit coupling [18]. The superconducting transition lines for the B_g and B_u states are also depicted, corresponding respectively to the BCS and PDW states as mentioned earlier

Based on the phase diagrams we have derived, the zero-field superconducting transition temperature, denoted as T_c, and the magnetic field strength at the parity transition point, denoted as H^*, have been estimated. For $\alpha/t_\perp = 1$, 2, and 3, these values are $(T_\mathrm{c}, H^*) = (0.0141, 0.195)$, $(0.0135, 0.212)$, and $(0.0124, 0.192)$, respectively. From these values, we proceed to evaluate H^* in units of T_c, enabling a normalized comparison across different $\alpha/t_\perp$ ratios.

$$\frac{H^*}{T_\mathrm{c}} = \begin{cases} 13.8 & (\alpha/t_\perp = 1) \\ 15.7 & (\alpha/t_\perp = 2) \\ 15.5 & (\alpha/t_\perp = 3). \end{cases} \tag{3.5.1}$$

From this analysis, we find that the parity transition fields, when scaled by the superconducting transition temperature, approximate to a universal value of $H^/T_\mathrm{c} \simeq 15$, irrespective of variations in $\alpha/t_\perp$. This result contrasts with the much smaller value of $H^/T_\mathrm{c} \simeq 2$ predicted by mean-field theory [1]. However, in the case of CeRh2As2, experimental observations reveal $H^* \simeq 3.9$,T and Tc $\simeq 0.26$,K, leading to an experimental ratio of $(H^*/T_\mathrm{c})_\mathrm{exp} \simeq 10$ [2]. Our theoretical findings, therefore, show quantitative consistency with the experimental phase diagram of $CeRh_2As_2$ and effectively bridge the gap between weak-coupling theory predictions and experimental data

Now, we examine potential reasons for the observed enhancement in the parity transition field H^*. First, one possibility is the influence of nonsymmorphic crystalline symmetry, as suggested in Ref. [104]. Indeed, the local noncentrosymmetricity indicator $\alpha/\tilde{t}_\perp(\boldsymbol{k})$ diverges

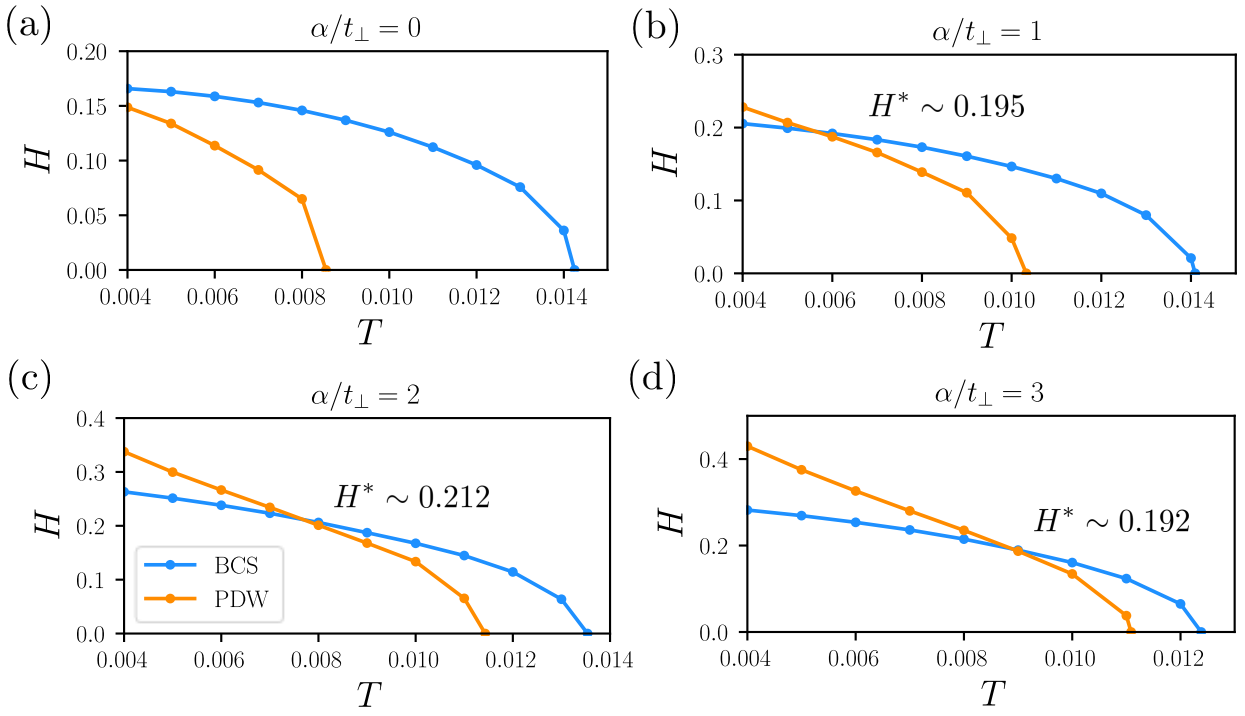

Figure 3.4: (a)-(d) H-T phase diagrams of the bilayer Rashba-Hubbard model for $\alpha/t_\perp = 0, 1, 2, 3$. We show the superconducting transition lines of the even-parity B_g and odd-parity B_u states, on which eigenvalues of the Éliashberg equation become unity. The BCS and PDW states correspond to the B_g and B_u superconducting phases, respectively. H^* denotes the magnetic field at the parity transition point.

at the Brillouin zone faces in nonsymmorphic crystals, due to $\tilde{t}_\perp(\boldsymbol{k}_{\rm face}) = 0$, which implies a more pronounced effect of spin-orbit coupling compared to the symmorphic case [104, 161]. However, our analysis of the bilayer Rashba-Hubbard model does not support this hypothesis, as the ratio $H^*/T_{\rm c}$ remains constant across different values of $\alpha/t_\perp$. Secondly, the presence of a spin-triplet component in the gap function could potentially alter the spin state of Cooper pairs, thus increasing H^*. Yet, this seems unlikely since a strong dependence of the parity mixing parameter r on $\alpha/t_\perp$ is observed (Fig. 3.5), defined as:

$$r = \frac{\max_{\boldsymbol{k}} |\boldsymbol{d}^{\rm AA}(\boldsymbol{k})|^2}{\max_{\boldsymbol{k}} |\psi^{\rm AA}(\boldsymbol{k})|^2}. \tag{3.5.2}$$

From Eq. (3.5.1) and Fig. 3.5, we note that there is no significant correlation between $H^*/T_{\rm c}$ and r. Thirdly, the field dependence of the effective interaction is also considered. In the bilayer Rashba-Hubbard model, the effective pairing interaction varies with the field due to field-enhanced magnetic anisotropy (see Fig. 4.1). Figure 3.6 illustrates the eigenvalues of

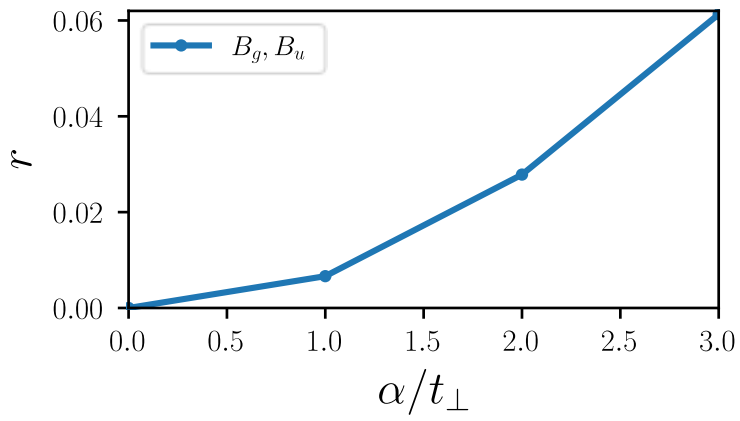

Figure 3.5: The parity mixing parameter r as a function of $\alpha/t_\perp$. The values for the B_g and B_u representations are nearly the same. We assume $T = 0.01$ and $H = 0.15$.

the 'Eliashberg equation both with and without the field dependence of magnetic anisotropy,[3] and we observe that this anisotropy weakens superconducting instabilities. However, it has a negligible effect on H^*. Consequently, field-enhanced magnetic anisotropy is not the primary factor in the enhancement of H^*. Conclusively, our findings suggest that the large parity transition field in $CeRh_2As_2$ is primarily due to the internal field resulting from quantum critical antiferromagnetic fluctuation. Near the antiferromagnetic critical point, electron spin correlations significantly intensify, and electrons exert an internal field on one another. In our model, the external Zeeman field applied to an electron is effectively screened by surrounding electrons, substantially increasing the scale of the magnetic fields [162]. This theory aligns with the observation of large upper critical fields in $CeRh_2As_2$, which notably surpass the Pauli-Clogston-Chandrasekhar limit, even in the in-plane direction [2].

3.6 Conclusion

Our study delved into the nature of quantum critical multipole fluctuation and superconductivity within the framework of the bilayer Rashba-Hubbard model, a simplified representa-

[3] To assess the impact of field-induced changes in the effective interaction, we solve the 'Eliashberg equation using zero-field vertex functions while adopting Green functions at $H \neq 0$. The eigenvalue without field-enhanced magnetic anisotropy, $\lambda^{\rm iso}$, is defined by the following equations:

$$\lambda^{\rm iso}\Delta_{\xi\xi'}(k) = \frac{T}{N}\sum_{k'}\Gamma^{a,H=0}_{\xi\xi_1\xi_2\xi'}(k-k')F^{H\neq0}_{\xi_1\xi_2}(k),$$
$$F^{H\neq0}_{\xi_1\xi_2}(k) = G^{H\neq0}_{\xi_1\xi_3}(k')\Delta_{\xi_3\xi_4}(k')G^{H\neq0}_{\xi_2\xi_4}(-k').$$

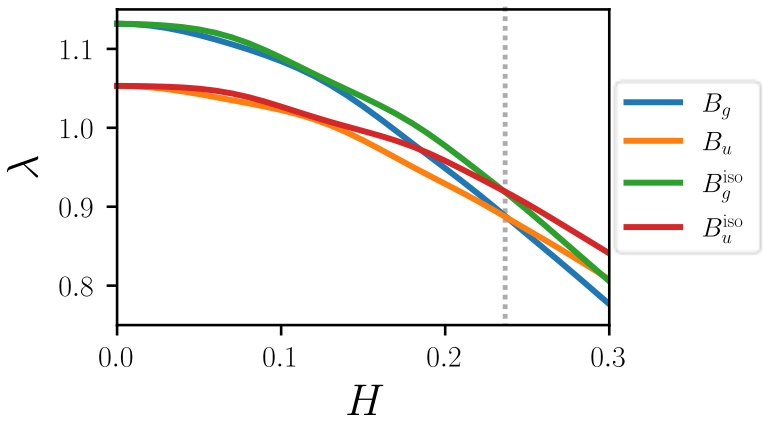

Figure 3.6: The magnetic field dependence of eigenvalues of the Éliashberg equation for the B_g and B_u representations. B_g^{iso} and B_u^{iso} represent the eigenvalues without the field-enhanced magnetic anisotropy. The parity transition points are indicated by the gray dashed line. We assume $\alpha/t_\perp = 2$ and $T = 0.01$.

tion of locally noncentrosymmetric, strongly correlated electron systems. This investigation was partly inspired by recent experimental findings in the newly discovered superconductor $CeRh_2As_2$ [2]. We found that XY-type antiferromagnetic fluctuations, which align with the results of NMR studies [16], are enhanced when a magnetic field is applied along the z axis. Due to these critical antiferromagnetic fluctuations, superconductivity characterized by dominant $d_{x^2-y^2}$-wave pairing and a subdominant p-wave pairing component is stabilized. Consequently, two distinct superconducting phases, differing in space inversion parity, emerge in the H-T phase diagram. This is consistent with observations made in $CeRh_2As_2$. Notably, the parity transition field is significantly enhanced by the quantum critical fluctuations, with the calculated value showing quantitative agreement with experimental measurements. These findings not only corroborate the parity transition observed in the superconducting state of $CeRh_2As_2$ [2] but also suggest the presence of topological superconductivity [127]. Furthermore, our theoretical framework contributes to resolving outstanding issues related to $CeRh_2As_2$ and provides insights into the general behavior of locally noncentrosymmetric, strongly correlated superconductors [163].

Chapter 4

Field-induced superconductivity mediated by odd-parity multipole fluctuation

Superconductivity, traditionally known to be suppressed by a magnetic field due to both Pauli and orbital-depairing effects [164], can paradoxically be induced by the magnetic field in certain systems. This counterintuitive phenomenon has attracted significant interest for its potential to reveal unconventional mechanisms underlying superconductivity. A well-recognized mechanism driving field-induced superconductivity is the Jaccarino-Peter effect [165, 166]. This effect describes how an external magnetic field can counterbalance the internal field generated by magnetic ions. Notable examples include the Chevrel phase superconductor $Eu_xSn_{1-x}Mo_6S_8$ [167, 168], and the organic superconductors λ-$(BETS)_2FeCl_4$ [169, 170] and κ-$(BETS)_2FeBr_4$ [171], where the Jaccarino-Peter effect has been observed. Furthermore, the reduction of Kondo scattering [172, 173] and the diminishment of the quasi-particle renormalization effect [174] are also theorized as alternative mechanisms contributing to field-induced superconductivity.

Field-induced superconductivity in uranium-based superconductors has been experimentally established in compounds such as UGe_2 [175, 176], URhGe [177, 178], UCoGe [179, 180], and UTe_2 [130, 181, 182, 183]. This phenomenon is largely attributed to changes in the effective interactions facilitating Cooper pairing, particularly through the enhancement of ferromagnetic fluctuations. The application of a magnetic field in these systems approaches a quantum critical point, thereby intensifying the effective interactions crucial for field-induced superconductivity. This relationship between field-induced superconductivity and quantum criticality has been supported by a range of studies [184, 185, 186, 187, 188, 189, 190, 191, 192], emphasizing the importance of ferromagnetic fluctuations near the quantum critical point.

The recent discovery of field-induced parity transition in $CeRh_2As_2$ has shed light on the role of sublattice degrees of freedom in heavy-fermion systems [2]. This finding has sparked

a flurry of both experimental and theoretical research, demonstrating that local inversion symmetry breaking can facilitate the formation of odd-parity pairings in Cooper pairs under high magnetic fields [3, 7, 8, 9, 10, 11, 15, 16, 17, 19, 22, 23, 24, 101, 102, 103, 104, 127, 137, 138, 163, 193, 194, 195, 196, 197, 198]. Interestingly, similar sublattice structures are also present in the uranium compounds discussed earlier, suggesting a broader relevance of these findings. Additionally, field-induced superconductivity has been reported in the locally noncentrosymmetric cerium-based superconductor $CeSb_2$ [199, 200] and in magic-angle twisted trilayer graphene [201, 202]. These observations in both uranium- and cerium-based superconductors, as well as in moiré systems, indicate that electron correlation effects might drive the superconducting states in these materials. Thus, theoretical investigations that concentrate on the interplay between strong correlation effects, sublattice degrees of freedom, and magnetic fields are of paramount importance. However, it is critical to note that most previous theoretical studies have relied on weak coupling theory, often assuming *degenerate* interactions within the sublattice degrees of freedom. This assumption may overlook key aspects of these complex systems, pointing to the need for more comprehensive theoretical models.

4.1 Effective Action

In this chapter, we present a novel mechanism for field-induced superconductivity, stemming from *degeneracy-lifted* pairing interactions within the sublattice degrees of freedom in strongly correlated superconductors. The theoretical underpinning of our model is encapsulated in the following effective action:

$$\begin{aligned}\mathcal{S}_{\text{eff}}[\bar{\psi},\psi] &= \mathcal{S}_{\text{eff},0}[\bar{\psi},\psi] + \mathcal{S}_{\text{eff, int}}[\bar{\psi},\psi] \\ &= \sum_{k} \bar{\psi}_{k,\alpha}(-i\omega_n\delta^{\alpha\beta} + \mathcal{H}_{\boldsymbol{k}}^{\alpha\beta} + \Sigma_k^{\alpha\beta})\psi_{k,\beta} \\ &+ \sum_{k,k',q} \bar{\psi}_{k+q,\alpha}\psi_{k,\beta}\Gamma_q^{\alpha\beta\gamma\delta}\bar{\psi}_{-k',\delta}\psi_{-k'+q,\gamma}, \end{aligned} \tag{4.1.1}$$

where we employ the abbreviated notation: $k = (\boldsymbol{k}, i\omega_n)$, $q = (\boldsymbol{q}, i\nu_n)$, and $\alpha = (s,\sigma)$. In this notation, $\boldsymbol{k}$ denotes the momentum, while $\omega_n = (2n+1)\pi T$ and $\nu_n = 2n\pi T$ are the fermionic and bosonic Matsubara frequencies, respectively. These represent the space-time dependence of the electron field $\psi_{k,\alpha}$ and the associated correlation functions. The indices s and σ correspond to spin and sublattice degrees of freedom, respectively. The term $\mathcal{H}^{\alpha\beta}\boldsymbol{k}$ represents the single-particle Hamiltonian. We also introduce the self-energy (Σ) and the vertex function (Γ). The self-energy is responsible for the renormalization of mass and damping of quasi-particles, while the vertex function facilitates superconductivity. These elements adhere to the Ward-Takahashi identity: $\Sigma_k^{\alpha\beta} = \sum_q \Gamma_q^{\alpha\gamma\beta\delta} G_{k-q}^{\delta\gamma}$ [203, 204], where $G_k^{\alpha\beta} = -\langle\psi_{k,\alpha}\bar{\psi}_{k,\beta}\rangle$ denotes the single-particle Green function. While we simplify the model

by omitting k and k' dependence in the vertex function, extending the analysis to include such momentum dependence is feasible and can be found in other works [205, 206].

In our study, we utilize diagrammatic techniques, such as the fluctuation exchange (FLEX) approximation [207, 208, 209] and the Parquet approximation [210, 211], to derive the effective action from the following bare action:

$$\begin{aligned}\mathcal{S}_{\mathrm{bare}}[\bar{\psi},\psi] = &\sum_{k} \bar{\psi}_{k,\alpha}(-i\omega_n\delta^{\alpha\beta} + \mathcal{H}_{\boldsymbol{k}}^{\alpha\beta})\psi_{k,\beta} \\ &+ \sum_{k,k',q} \bar{\psi}_{k+q,\alpha}\psi_{k,\beta}\Gamma_q^{0,\alpha\beta\gamma\delta}\bar{\psi}_{-k',\delta}\psi_{-k'+q,\gamma}. \end{aligned} \tag{4.1.2}$$

This study primarily focuses on two-sublattice superconductors, encompassing both bilayer superconductors and two-fold non-symmorphic crystalline superconductors. The Hamiltonian $\mathcal{H}_{\boldsymbol{k}}^{\alpha\beta}$ in the bare action describes the two-sublattice system and is given by:

$$\mathcal{H}\boldsymbol{k} = \varepsilon_{\boldsymbol{k}} s_0 \otimes \sigma_0 + \alpha \boldsymbol{g}_{\boldsymbol{k}} \cdot \boldsymbol{s} \otimes \sigma_z + t_\perp s_0 \otimes \sigma_x - \mu_{\mathrm{B}} H s_z \otimes \sigma_0.$$

Here, $\varepsilon_{\boldsymbol{k}} = -2t(\cos k_x + \cos k_y) + 4t' \cos k_x \cos k_y - \mu$ and $t_\perp$ denote intra- and inter-sublattice hopping terms, respectively. The sublattice-dependent $\boldsymbol{g}_{\boldsymbol{k}} \cdot \boldsymbol{s}$ term represents staggered Rashba-type spin-orbit coupling, arising from local inversion symmetry breaking [1, 18, 81, 101, 115, 116, 117, 118, 121, 122, 141, 212, 213]. The g-vector $\boldsymbol{g}_{\boldsymbol{k}} = [-\partial\varepsilon_{\boldsymbol{k}}/\partial k_y, \partial\varepsilon_{\boldsymbol{k}}/\partial k_x, 0]$ introduces momentum-dependent spin polarization [109]. The term H represents the Zeeman magnetic field parallel to the z-axis. The bare action also includes the Hubbard-type on-site Coulomb repulsion as its interaction term:

$$\mathcal{S}_{\mathrm{bare,\,int}} = U \sum_{\sigma} \bar{\psi}_{i,\uparrow,\sigma}\psi_{i,\uparrow,\sigma}\bar{\psi}_{i,\downarrow,\sigma}\psi_{i,\downarrow,\sigma}.$$

From this interaction, the bare interaction tensor Γ^0 is derived, serving as the basis for further analysis.

In our two-sublattice model, the internal degrees of freedom are characterized using the augmented multipole operator $\hat{\mathcal{Q}}$ [158, 159, 160]. This operator is defined as $\hat{\mathcal{Q}}^{\mu\nu} = \sum_k \bar{\psi}_{k+q,\alpha}\mathcal{Q}^{\mu\nu}\alpha\beta\psi_{k,\beta}$, where $\mathcal{Q}^{\mu\nu} = \bar{s}^\mu \otimes \bar{\sigma}^\nu$ adheres to the normalization condition $\mathrm{tr}[\mathcal{Q}\mathcal{Q}^\dagger] = 1$. Here, $\bar{s}^\mu = s^\mu/\sqrt{2}$ and $\bar{\sigma}^\mu = \sigma^\mu/\sqrt{2}$ represent the normalized Pauli and unit matrices, respectively. The interaction term of the effective action, $\mathcal{S}_{\mathrm{eff,\,int}}$, can be reformulated as a sum of bilinear interactions of these multipoles [214, 215, 216, 217, 218]:

$$\mathcal{S}_{\mathrm{eff,\,int}}[\bar{\psi},\psi] \approx \sum_{\mathcal{Q},q} \hat{\mathcal{Q}}_q V_q^{\mathcal{Q}} \hat{\mathcal{Q}}_{-q}, \tag{4.1.3}$$

where $V_q^{\mathcal{Q}} = \mathcal{Q}_{\alpha\beta}\Gamma_q^{\beta\alpha\gamma\delta}\mathcal{Q}_{\gamma\delta}$ represents the coupling constants for interactions between the augmented multipoles. To simplify the discussion, interactions between different types of multipoles are omitted in this context.

In this chapter, we delve into the mechanism of field-induced superconductivity originating from degeneracy-lifted pairing interactions in sublattice degrees of freedom. Utilizing multipole resolved interactions, zero-momentum ($q = k - k' = 0$) Cooper pairing interactions are derived [205, 206]. Specifically, intra-sublattice even- and odd-parity multipole fluctuations, denoted by $\bar{\sigma}^0$ and $\bar{\sigma}^z$, give rise to distinct Cooper pairing interactions [206]:

$$\mathcal{S}_{\sigma_0}[\bar{\psi},\psi] = \frac{1}{2}\sum_{k,k'} V^{\sigma^0}_{k-k'}\{\hat{\mathcal{P}}^{0,\dagger}_k\hat{\mathcal{P}}^0_{k'} + \hat{\mathcal{P}}^{z,\dagger}_k\hat{\mathcal{P}}^z_{k'} + \hat{\mathcal{P}}^{x,\dagger}_k\hat{\mathcal{P}}^x_{k'} + \hat{\mathcal{P}}^{y,\dagger}_k\hat{\mathcal{P}}^y_{k'}\}, \tag{4.1.4}$$

$$\mathcal{S}_{\sigma_z}[\bar{\psi},\psi] = \frac{1}{2}\sum_{k,k'} V^{\sigma^z}_{k-k'}\{\hat{\mathcal{P}}^{0,\dagger}_k\hat{\mathcal{P}}^0_{k'} + \hat{\mathcal{P}}^{z,\dagger}_k\hat{\mathcal{P}}^z_{k'} - \hat{\mathcal{P}}^{x,\dagger}_k\hat{\mathcal{P}}^x_{k'} - \hat{\mathcal{P}}^{y,\dagger}_k\hat{\mathcal{P}}^y_{k'}\}, \tag{4.1.5}$$

where $\hat{\mathcal{P}}^\mu = \psi_\alpha\bar{\sigma}^\mu_{\alpha\beta}\psi_\beta$. In scenarios where even- and odd-parity multipole interactions share the same coupling constant (i.e., $V_{k-k'} := V^{\sigma^0}_{k-k'} = V^{\sigma^z}_{k-k'}$), a degenerate interaction model is realized:

$$\mathcal{S}_{\text{degenerate}} = \sum_{k,k'} V_{k-k'}\{\hat{\mathcal{P}}^{0,\dagger}_k\hat{\mathcal{P}}^0_{k'} + \hat{\mathcal{P}}^{z,\dagger}_k\hat{\mathcal{P}}^z_{k'}\}. \tag{4.1.6}$$

This model represents the typical pairing interaction often assumed for two-sublattice models [1, 18, 101, 115, 116, 117, 118, 121, 219, 220]. When degeneracy is lifted, as in Eqs. (4.1.4) and (4.1.5), unconventional inter-sublattice Cooper pairing channels emerge. This degeneracy-lifted interaction, commonplace in strongly correlated systems, is key to field-induced superconductivity, as discussed in this chapter. The FLEX approximation extended to spin-orbit-coupled two-sublattice systems is applied to derive the effective action in our model [221, 222, 223, 224] (for detail see Sec. 3.2). Hereafter, we set $t' = 0.3$, $\mu_{\text{B}} = 1$, and $U = 3.9$ with a unit of energy $t = 1$ and determine the chemical potential so that the electron density per site n is 0.85. In the numerical study, we use 64×64 $\boldsymbol{k}$-meshes, and 16384, 8192, or 4096 Matsubara frequencies for $T = 0.004$, $0.004 < T < 0.01$, or $0.01 \leq T$, respectively.

4.2 Odd-parity multipole fluctuation

First, we summarize multipole operator in our system and multipole decomposition of the generalized susceptibility. The normalized Pauli matrices ($\bar{\boldsymbol{\sigma}} = \boldsymbol{\sigma}/\sqrt{2}$) and the unit matrix ($\bar{\sigma}^0 = \sigma^0/\sqrt{2}$) compose a complete basis of 2×2 matrix space. Here, we adopt the normalization convention $\text{tr}[(\sigma^\mu)^\dagger\sigma^\mu] = 1$. Namely, any 2×2 complex matrix A can be represented as a linear combination of the normalized Pauli matrices and the unit matrix,

$$A = \sum_\mu a_\mu\bar{\sigma}^\mu, \tag{4.2.1}$$

where a_μ are complex coefficients. When A is a Hermitian matrix, a_μ should be real numbers. The completeness of the Pauli matrices and the unit matrix leads to the following identity:

$$\sum_\mu \bar{\sigma}^\mu_{ij}(\bar{\sigma}^\mu_{kl})^* = \sum_\mu \bar{\sigma}^\mu_{ij}\bar{\sigma}^\mu_{lk} = \delta_{ik}\delta_{jl}, \tag{4.2.2}$$

where δ_{ij} is Kronecker delta. Here, the Hermite property of the Pauli and unit matrices $\bar{\sigma}_{ij} = (\bar{\sigma}_{ji})^*$ is used in the first equal sign.

The multipole operator in a two-sublattice system is represented by the tensor product of the Pauli matrices in spin- and sublattice-spaces: $\bar{\mathcal{Q}}^{\mu\nu} = \bar{s}^\mu \otimes \bar{\sigma}^\nu$. Consequently, the following identity holds:

$$\sum_{\mathcal{Q}} \bar{\mathcal{Q}}_{ij}\bar{\mathcal{Q}}_{kl} = \delta_{il}\delta_{jk}. \tag{4.2.3}$$

This identity facilitates the analysis of multipole-resolved fluctuations. It should be noted that extending the current discussion to cases with general N degrees of freedom is straightforward. This involves replacing the Pauli matrix with the $\mathfrak{su}(N)$ Lie algebra.

Upon inserting Eq. (4.2.3), Eq. (3.2.9) can be reformulated into a multipole-resolved form as,

$$\begin{aligned}
\chi^{\mathcal{Q}}(\boldsymbol{q}, i\nu_n) &= \bar{\mathcal{Q}}_{\xi_1\xi_2}\chi_{\xi_2\xi_1\xi_3\xi_4}(\boldsymbol{q}, i\nu_n)\bar{\mathcal{Q}}_{\xi_3\xi_4} \\
&= \chi^{0,\mathcal{Q}}(\boldsymbol{q}, i\nu_n) \\
&+ \sum_{\mathcal{Q}'\mathcal{Q}''} \bar{\mathcal{Q}}_{\xi_1\xi_2}\chi^0_{\xi_2\xi_1\xi_5\xi_6}(\boldsymbol{q}, i\nu_n)\bar{\mathcal{Q}}'_{\xi_5\xi_6}\bar{\mathcal{Q}}'_{\xi_7\xi_8}U_{\xi_8\xi_7\xi_9\xi_{10}}\bar{\mathcal{Q}}''_{\xi_9\xi_{10}}\bar{\mathcal{Q}}''_{\xi_{11}\xi_{12}}\chi_{\xi_{12}\xi_{11}\xi_3\xi_4}(\boldsymbol{q}, i\nu_n)\bar{\mathcal{Q}}_{\xi_3\xi_4}
\end{aligned} \tag{4.2.4}$$

$$\approx \chi^{0,\mathcal{Q}}(\boldsymbol{q}, i\nu_n) + \chi^{0,\mathcal{Q}}(\boldsymbol{q}, i\nu_n)U^{\mathcal{Q}}\chi^{\mathcal{Q}}(\boldsymbol{q}, i\nu_n), \tag{4.2.5}$$

where $U^{\mathcal{Q}} = \bar{\mathcal{Q}}_{\xi_1\xi_2}U_{\xi_1\xi_2\xi_3\xi_4}\bar{\mathcal{Q}}_{\xi_4\xi_3}$. In this final expression, the cross terms between different multipole terms, denoted as $\chi^{\mathcal{Q}\mathcal{Q}'} = \bar{\mathcal{Q}}_{\xi_1\xi_2}\chi_{\xi_1\xi_2\xi_3\xi_4}\bar{\mathcal{Q}}'_{\xi_4\xi_3}$, are ignored. Solving Eq. (4.2.5), we obtain the enhanced multipole susceptibility due to interactions:

$$\chi^{\mathcal{Q}}(q) \approx \frac{\chi^{0,\mathcal{Q}}(q)}{1 - U^{\mathcal{Q}}\chi^{0,\mathcal{Q}}(q)}. \tag{4.2.6}$$

A sufficient condition for achieving a large $\chi^{\mathcal{Q}}(q)$ entails having a large $\chi^{0,\mathcal{Q}}(q)$ and a positive U^{Q}. When we ignore the self-energy, the bare multipole susceptibility $\chi^{0,\mathcal{Q}}(q)$ can be

expressed in the band basis as,

$$\begin{aligned}
\chi^{0,\mathcal{Q}}(q) &= \bar{\mathcal{Q}}_{\beta\alpha}\chi^{(0)}_{\alpha\beta\gamma\delta}(q)\bar{\mathcal{Q}}_{\gamma\delta} \\
&= -\bar{\mathcal{Q}}_{\beta\alpha}\frac{T}{N}\sum_{k} G_{\alpha\gamma}(k)G_{\delta\beta}(k-q)\bar{\mathcal{Q}}_{\gamma\delta} \\
&= -\bar{\mathcal{Q}}_{\beta\alpha}\frac{T}{N}\sum_{k} U_{\alpha\zeta}(\boldsymbol{k})\mathcal{G}_{\zeta}(k)U^{*}_{\gamma\zeta}(\boldsymbol{k})U_{\delta\eta}(\boldsymbol{k}-\boldsymbol{q})\mathcal{G}_{\eta}(k-q)U^{*}_{\beta\eta}(\boldsymbol{k}-\boldsymbol{q})\bar{\mathcal{Q}}_{\gamma\delta} \\
&= -\frac{T}{N}\sum_{k}\left(U^{\dagger}(\boldsymbol{k}-\boldsymbol{q})\bar{\mathcal{Q}}U(\boldsymbol{k})\right)_{\eta\zeta}\mathcal{G}_{\zeta}(k)\mathcal{G}_{\eta}(k-q)\left(U^{\dagger}(\boldsymbol{k})\bar{\mathcal{Q}}U(\boldsymbol{k}-\boldsymbol{q})\right)_{\zeta\eta} \\
&= -\frac{1}{N}\sum_{\boldsymbol{k}}\langle u_{\eta,\boldsymbol{k}-\boldsymbol{q}}|\bar{\mathcal{Q}}|u_{\zeta,\boldsymbol{k}}\rangle\langle u_{\zeta,\boldsymbol{k}}|\bar{\mathcal{Q}}|u_{\eta,\boldsymbol{k}-\boldsymbol{q}}\rangle \times \frac{f(\varepsilon_{\eta}(\boldsymbol{k}-\boldsymbol{q}))-f(\varepsilon_{\zeta}(\boldsymbol{k}))}{i\nu_n+\varepsilon_{\eta}(\boldsymbol{k}-\boldsymbol{q})-\varepsilon_{\zeta}(\boldsymbol{k})} \\
&= \sum_{\boldsymbol{k}}\langle u_{\eta,\boldsymbol{k}-\boldsymbol{q}}|\bar{\mathcal{Q}}|u_{\zeta,\boldsymbol{k}}\rangle\langle u_{\zeta,\boldsymbol{k}}|\bar{\mathcal{Q}}|u_{\eta,\boldsymbol{k}-\boldsymbol{q}}\rangle\, L_{\zeta\eta}(\boldsymbol{k},\boldsymbol{q},i\nu_n), \qquad (4.2.7)
\end{aligned}$$

where $L_{\zeta\eta}(\boldsymbol{k},\boldsymbol{q},i\nu_n) = -\frac{1}{N}\{f(\varepsilon_{\eta}(\boldsymbol{k}-\boldsymbol{q}))-f(\varepsilon_{\zeta}(\boldsymbol{k}))\}/\{i\nu_n+\varepsilon_{\eta}(\boldsymbol{k}-\boldsymbol{q})-\varepsilon_{\zeta}(\boldsymbol{k})\}$ denotes the momentum-resolved Lindhard function between ζ and η bands. Here, $U(\boldsymbol{k})_{\alpha\zeta} = \langle\alpha|u_{\zeta,\boldsymbol{k}}\rangle$ represents the unitary matrix that diagonalizes Hamiltonian:

$$U^{\dagger}(\boldsymbol{k})\mathcal{H}(\boldsymbol{k})U(\boldsymbol{k}) = \mathcal{H}^{\mathrm{diag}}(\boldsymbol{k}), \qquad (4.2.8)$$

$$\mathcal{H}(\boldsymbol{k})\,|u_{\zeta,\boldsymbol{k}}\rangle = \varepsilon_{\zeta}(\boldsymbol{k})\,|u_{\zeta,\boldsymbol{k}}\rangle\,. \qquad (4.2.9)$$

The Green function in the band basis is given by

$$\begin{aligned}
\mathcal{G}(k) &= U^{\dagger}(\boldsymbol{k})G(k)U(\boldsymbol{k}), \\
\mathcal{G}_{\zeta}(k) &= \frac{1}{i\omega_n-\varepsilon_{\zeta}(\boldsymbol{k})}. \qquad (4.2.10)
\end{aligned}$$

In the same manner, we can decompose the effective interaction $\Gamma^{n}(q)$ [as defined in Eq. (3.2.4)] and $\Gamma^{a}(q)$ [as defined in Eq. (3.2.11)] into their respective multipole channels. The decomposition is expressed as follows:

$$\Gamma^{n,\mathcal{Q}}(q) \approx U^{\mathcal{Q}}\left(\chi^{\mathcal{Q}}(q)-\frac{1}{2}\chi^{0,\mathcal{Q}}(q)\right)U^{\mathcal{Q}}, \qquad (4.2.11)$$

$$\Gamma^{a,\mathcal{Q}}(q) \approx \frac{U^{\mathcal{Q}}}{2}+U^{\mathcal{Q}}\chi^{\mathcal{Q}}(q)U^{\mathcal{Q}}. \qquad (4.2.12)$$

In Eq. (4.2.11), the effective interaction for the particle-hole channel, $\Gamma^{n,\mathcal{Q}}(q)$, is expressed as a function of the multipole susceptibility $\chi^{\mathcal{Q}}(q)$ and the bare susceptibility $\chi^{0,\mathcal{Q}}(q)$ modulated by the interaction $U^{\mathcal{Q}}$. Similarly, Eq. (4.2.12) depicts the effective interaction for the particle-particle channel, $\Gamma^{a,\mathcal{Q}}(q)$, also as a function of the multipole susceptibility and interaction.

In this work, we demonstrate that a two-sublattice structure inherently encourages odd-parity multipole fluctuations. As depicted in Figure 4.1(a), the Fermi surfaces of our two-sublattice tight-binding model are characterized by two bands, labeled $|1\rangle$ and $|2\rangle$. A notable

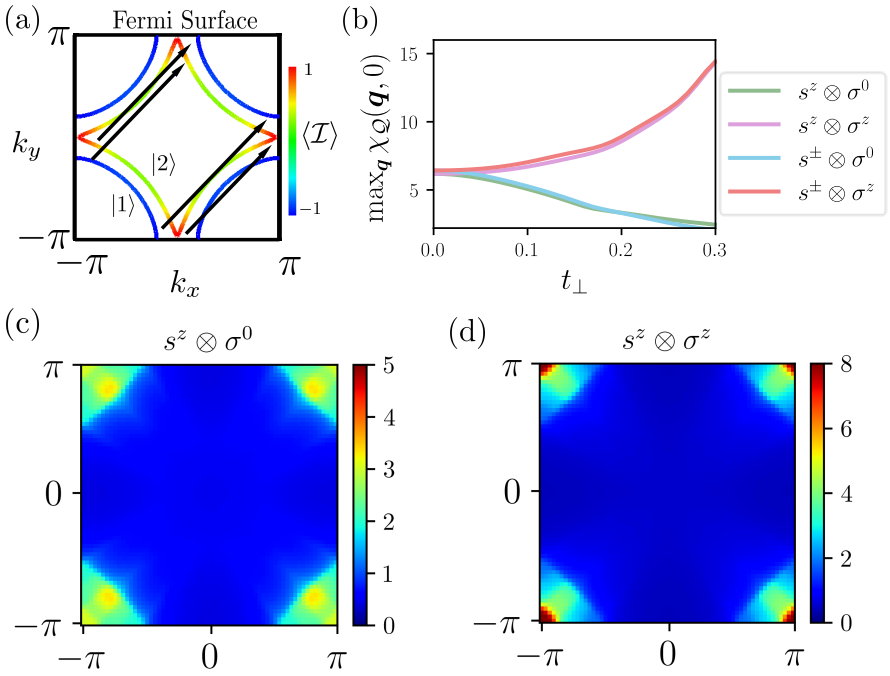

Figure 4.1: (a) The Fermi surface of the two-sublattice tight-binding model with the model parameters: $\alpha = 0.2$, $t_\perp = 0.2$. The coloration on the Fermi surface signifies the expectation value of the inversion symmetry operator $\mathcal{I} = s_0 \otimes \sigma_z$. (b) The inter-sublattice hopping $t_\perp$ dependence of static multipole fluctuations. The maximum of the even-parity (odd-parity) longitudinal (transverse) magnetic multipole susceptibilities are shown. Other multipole fluctuations are negligibly small. We assume $\alpha = 0.2$, $t_\perp = 0.2$ and $T = 0.01$. (c), (d) The momentum dependence of the even-parity and odd-parity longitudinal magnetic susceptibilities, respectively.

feature of our system is the presence of type-II van Hove singularities, a consequence of Rashba-type spin-orbit coupling [114, 225, 226]. These singularities are specifically located at $\boldsymbol{k} = (\pm\delta, \pi)$, $(0, \pi \pm \delta)$, $(\pi, \pm\delta)$, and $(\pi \pm \delta, 0)$, positions distinct from time-reversal invariant momentum points that satisfy $\boldsymbol{K} = -\boldsymbol{K}$ modulo reciprocal lattice vectors. Furthermore, Figure 4.1(a) illustrates the expectation values of the inversion symmetry operator $\mathcal{I} = s_0 \otimes \sigma_z$ on the Fermi surfaces. The bonding and anti-bonding orbitals, defined as $|\mathrm{BO}\rangle \equiv (1,1)^\top_\sigma / \sqrt{2}$ and $|\mathrm{ABO}\rangle \equiv (1,-1)^\top_\sigma / \sqrt{2}$, interact with $\mathcal{I}$ such that $\mathcal{I}\,|\mathrm{BO}\rangle = |\mathrm{BO}\rangle$ and $\mathcal{I}\,|\mathrm{ABO}\rangle = -\,|\mathrm{ABO}\rangle$. Given that the expectation values of $\mathcal{I}$ on the Fermi surfaces are approximately ± 1, it can be inferred that the wave functions around the type-II van Hove singularities predominantly resemble either bonding or anti-bonding orbitals.

In itinerant electron systems, multipole fluctuations are often driven by the nesting of Fermi surfaces, particularly near van Hove singularities [139, 227]. There are two primary

nesting scenarios to consider: the first involves nesting within the same Fermi surface, either from bonding to bonding or anti-bonding to anti-bonding states. The second scenario entails nesting between different Fermi surfaces, such as bonding to anti-bonding. Figure 4.1(a) illustrates the nesting vectors corresponding to each of these scenarios. It is important to note that while the nesting vectors connecting identical Fermi surfaces (i.e., bonding to bonding or anti-bonding to anti-bonding) differ from one another, those that connect different Fermi surfaces (bonding to anti-bonding) are equivalent. Consequently, in the context of a two-sublattice model, the nesting between different Fermi surfaces plays a crucial role in significantly enhancing multipole fluctuations. This enhancement is particularly pronounced for operators with strong matrix elements between the Fermi surfaces $|1\rangle$ and $|2\rangle$.

By utilizing the approximated wave functions established earlier, we can conduct a rough estimation of the matrix elements for the sublattice operator. Specifically, we find that $\langle 1|\sigma^0|1\rangle \approx \langle 1|\sigma^z|2\rangle \approx 1$ and $\langle 1|\sigma^0|2\rangle \approx \langle 1|\sigma^z|1\rangle \approx 0$. This analysis indicates that nesting within the same Fermi surface predominantly enhances even-parity multipole fluctuations. Conversely, nesting between different Fermi surfaces is more likely to lead to odd-parity fluctuations. From these observations, we infer that a two-sublattice structure inherently favors the emergence of odd-parity multipole fluctuations. This tendency is particularly pronounced when the inter-sublattice hopping term, $t_\perp$, is large and the chemical potential is positioned near the van Hove singularity. This conclusion is vital for understanding the nature of multipole fluctuations in two-sublattice systems and their implications for superconductivity.

In our model, the Hubbard-type Coulomb interaction is articulated in the multipole basis as follows:

$$\mathcal{S}_{\rm int} = -U \sum_{\nu=0,z} \hat{\mathcal{Q}}^{0\nu}_q \hat{\mathcal{Q}}^{0\nu}_{-q} + U \sum_{\substack{\mu=x,y,z \\ \nu=0,z}} \hat{\mathcal{Q}}^{\mu\nu}_q \hat{\mathcal{Q}}^{\mu\nu}_{-q}. \tag{4.2.13}$$

This formulation of the multipole-resolved interaction indicates that the Coulomb interaction promotes both even-parity and odd-parity magnetic multipoles with equal strength. Figure 4.1(b) visualizes how these multipole fluctuations vary with changes in $t_\perp$, as calculated using the fluctuation exchange (FLEX) approximation. We observe that with an increase in the inter-sublattice hopping parameter $t_\perp$, there is a pronounced enhancement in odd-parity fluctuations, while even-parity fluctuations tend to be suppressed. This trend aligns with our previous discussions and the theoretical framework outlined in the model.

Figures 4.1(c) and (d) present the momentum dependence of the multipole susceptibilities. Specifically, the even-parity longitudinal magnetic fluctuation, represented by the multipole operator $\mathcal{Q}^{z0} = \bar{s}^z \otimes \bar{\sigma}^0$, is characterized by a double peak structure around $\boldsymbol{Q} \sim (\pi, \pi)$ and $(\pi - \delta, \pi - \delta)$, as shown in Figure 4.1(c). Conversely, the odd-parity longitudinal magnetic fluctuation, denoted by the multipole operator $\mathcal{Q}^{zz} = \bar{s}^z \otimes \bar{\sigma}^z$, displays a single peak structure centered around $\boldsymbol{Q} \sim (\pi, \pi)$, as depicted in Figure 4.1(d). These observations lend further support to our prior analysis concerning the nesting and wave functions of the Fermi surfaces, providing a more quantitative perspective. It is also noteworthy that the transverse magnetic

fluctuations exhibit a momentum dependence similar to that of the longitudinal fluctuations, indicating a consistent pattern across different types of magnetic fluctuations in the system.

It is important to note that the Hubbard-type Coulomb interaction, as expressed in Equation (4.2.13), appears degenerate when analyzed within a multipole basis. This degeneracy implies that, at a mean-field level, all magnetic multipole interactions are considered to be equivalent. However, this degeneracy is not absolute and gets lifted when many-body effects are taken into account. Specifically, the intrinsic properties of the wave functions of itinerant electrons play a crucial role in this context, leading to a predominance of odd-parity multipole fluctuations at low energy levels. This observation highlights the dynamic nature of the interaction in itinerant electron systems. While the mean-field analysis provides a foundational understanding, the inclusion of many-body effects reveals a more nuanced picture, particularly in the emergence of dominant odd-parity multipole fluctuations, which are key to understanding the low-energy behavior of these systems.

4.3 Superconductivity

In our study, we examine superconductivity predominantly mediated by odd-parity multipole fluctuations through the linearized Éliashberg equation. Figure 4.2(a) illustrates how the eigenvalues of this equation vary with the external magnetic field. In the left panel, corresponding to $t_\perp = 0.1$, a typical response of superconductivity to an external magnetic field is observed. The eigenvalues for all irreducible representations are progressively suppressed as the magnetic field strength increases. A notable feature at $H = 0.22$ is the intersection of the eigenvalue curves for the B_g and B_u representations. This intersection indicates a phase transition from even-parity to odd-parity superconductivity, a phenomenon similar to that observed in $CeRh_2As_2$ [1, 2, 163]. Conversely, the right panel for $t_\perp = 0.2$ demonstrates a distinct behavior. Here, the eigenvalue for the B_u representation actually increases with the application of the magnetic field, whereas the eigenvalue for the B_g representation decreases. This pattern suggests the intriguing possibility of field-induced odd-parity superconductivity emerging in two-sublattice strongly correlated electron systems.

We investigate the underlying mechanism of field-induced superconductivity in our model. Initially, we examine the intra-sublattice pair potential, $\Delta^{\rm intra}_{B_u}(k) = \psi(\boldsymbol{k}) i s_y \otimes \sigma_z + \boldsymbol{d}(\boldsymbol{k}) \cdot \boldsymbol{s}, i s_y \otimes \sigma_0$, as illustrated in Figs. 4.2(b)-(d). Influenced by antiferromagnetic fluctuation, the spin-singlet component of this potential adopts a $d_{x^2-y^2}$-wave form, while the spin-triplet components, induced by spin-orbit coupling, exhibit a p-wave momentum dependence. Notably, these gap functions show a relative insensitivity to the external magnetic field [1, 2, 163]. Next, we analyze the inter-sublattice pair potentials. As shown in Fig.4.2(e), the magnetic field influences these gap functions significantly. A key observation is the induction of a sizable spin-triplet and inter-sublattice anti-symmetric pair potential by the magnetic field,

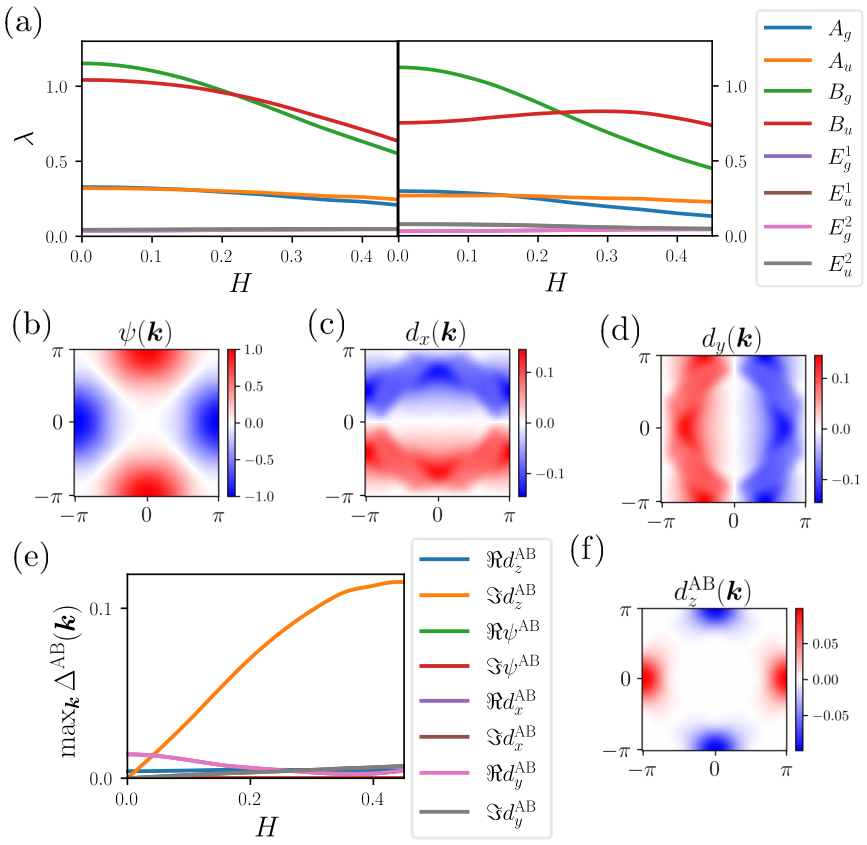

Figure 4.2: (a) The magnetic field dependence of eigenvalues of the Éliashberg equation for each irreducible representation. We assume $\alpha = 0.2$ and $T = 0.01$. (Left) $t_\perp = 0.1$. (Right) $t_\perp = 0.2$. Superconducting instabilities are classified by the irreducible representation of the point group of the system, C_{4h}. The superscript of $E_{g/u}^{1,2}$ representations expresses the degeneracy lifted by time-reversal symmetry breaking due to the magnetic field. (b-d) The momentum dependence of intra-sublattice spin-singlet and spin-triplet gap functions, $\psi(\boldsymbol{k})$ and $\boldsymbol{d}(\boldsymbol{k})$, of the B_u representation for $H = 0.15$. Results for the B_g representation are almost the same as the figures. (e) The magnetic field dependence of the component-resolved weight of the inter-sublattice gap function. (f) The momentum dependence of the inter-sublattice spin-triplet gap function, $\mathrm{Im}\, d_z^{\mathrm{AB}}(\boldsymbol{k})$.

represented by:

$$\mathrm{Im}\, d_z^{\mathrm{AB}}(\boldsymbol{k}) s_z i s_y \otimes \sigma_y, \tag{4.3.1}$$

This pair potential, which is forbidden in the absence of a magnetic field due to time-reversal symmetry, gains prominence under magnetic influence. Its momentum dependence is depicted in Fig.4.2(f). Equation (4.3.1) highlights the σ_y-component in the sublattice degree of freedom, signifying that the pairing channel $\mathcal{P}_k^y$, as discussed in Eqs. (4.1.4) and (4.1.5), becomes crucial. This channel arises due to the lifting of degeneracy between even-parity and odd-parity multipole fluctuations. In summary, the Cooper pairing described by Eq.(4.3.1) is fundamentally a result of multipole-mediated interactions [Eqs.(4.1.4) and (4.1.5)] and the disruption of time-reversal symmetry by the external magnetic field. Consequently, field-induced superconductivity in the two-sublattice system emerges through a synergistic interaction between the odd-parity multipole fluctuation and the magnetic field.

Additional support for our interpretation of the mechanism driving field-induced superconductivity emerges from analyses based on Feynman diagrams. These diagrams provide a visual and analytical method to understand the interactions and processes occurring within the system. Specifically, the gap function, as described in Eq. (4.3.1), assumes a vital role in this context. It facilitates the coupling between intra-sublattice gap functions through a second-order scattering process. This process, visualized and analyzed using Feynman diagrams, illustrates how the gap function effectively acts as an intermediary, enabling interactions between gap functions of the same sublattice. The second-order scattering process, involving the exchange of virtual quasiparticles or collective excitations, contributes significantly to the development of superconductivity under the influence of an external magnetic field.

Let us elucidate the distinctive role of inter-sublattice pairing in the field-induced odd-parity superconductivity. Utilizing the diagrammatic expression of the Éliashberg equation, we specify the important scattering process. While simplification is attained by solely considering the transverse spin fluctuation denoted by $\chi^{\pm}$ or $\chi^{\mp}$, expanding the following analysis to include longitudinal spin fluctuation χ^{zz} is straightforward. In the following, we denote the dominant intra-sublattice spin-singlet component in the A and B sublattices as $\psi^{\mathrm{AA}}(\boldsymbol{k})$ and $\psi^{\mathrm{BB}}(\boldsymbol{k})$, respectively.

The scattering processes illustrated in Figs. 4.3(a-b) highlight how the unusual inter-sublattice pairing, represented by $\mathrm{Im}\, d_z^{\mathrm{AB}}(\boldsymbol{k}) s_z i s_y \otimes \sigma_y$, introduces the attractive force between $\psi^{\mathrm{AA}}(\boldsymbol{k})$ and $\psi^{\mathrm{BB}}(\boldsymbol{k})$. By amalgamating these two diagrams and tracing out the gap function d_z^{BA}, a composite diagram elucidating the second-order scattering process between $\psi^{\mathrm{AA}}(\boldsymbol{k})$ and $\psi^{\mathrm{BB}}(\boldsymbol{k})$ is derived. Due to the positive sign of $\chi^{\pm}_{\mathrm{AA}}$ and the negative sign of $\chi^{\mp}_{\mathrm{BA}}$ [see Fig. 4.3(c,d)], the overall sign of this second-order scattering process is negative. This scattering process with negative sign necessitates a sign change of gap functions through $2\boldsymbol{q} = (0, 0)$ momentum transfer, a condition intrinsically met due to the relation $\psi^{\mathrm{AA}}(\boldsymbol{k}) = -\psi^{\mathrm{BB}}(\boldsymbol{k})$. Notably, spin-orbit coupling is not required in this mechanism, thereby implying that field-

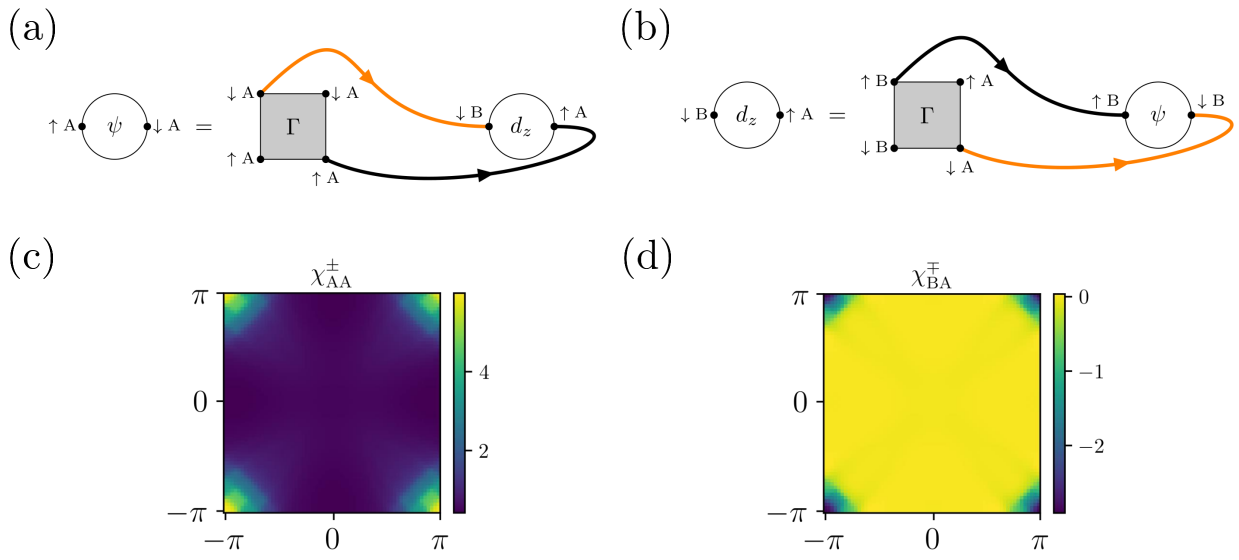

Figure 4.3: (a) (b) The diagrammatic representation of the dominant scattering process between the Cooper pairs represented by ψ^{AA}, ψ^{BB}, and d_z^{AB}. The black line and orange line represent the intra-sublattice Green function $G^{\mathrm{AA}}(k)$ and the inter-sublattice Green function $G^{\mathrm{AB}}(k)$, respectively. The scattering process between d_z^{AB} and ψ^{AA} or ψ^{BB} via the transverse magnetic fluctuation are shown. (c) The momentum dependence of the intra-sublattice transverse magnetic fluctuation which appears in the diagram (a). (d) The momentum dependence of the inter-sublattice transverse magnetic fluctuation which appears in the diagram (b).

induced superconductivity can be achieved in materials with weak spin-orbit coupling.

4.4 Phase diagram

Figures 4.4(a)-(d) display the phase diagrams for various ratios of $\alpha/t_\perp$, namely 0, 0.5, 1, and 2, while keeping $t_\perp = 0.2$ constant. In all these scenarios, the odd-parity superconducting state demonstrates field-induced behaviors. A notable observation is that even in the absence of spin-orbit coupling ($\alpha = 0$), the external magnetic field still induces the odd-parity superconducting phase. This finding indicates that field-induced superconductivity can occur independently of spin-orbit coupling. However, the presence of stronger spin-orbit coupling ($\alpha > 0$) significantly enhances the stability of the field-induced odd-parity superconducting phase, as evidenced by the increase in transition temperature. In the context of spin-orbit coupling, the gap function described in Eq. (4.3.1) includes intra-band components, expressed as:

$$\Delta^{\pm}(\boldsymbol{k}) = \frac{d_z^{\mathrm{AB}}(\boldsymbol{k})}{|\boldsymbol{g}(\boldsymbol{k})|^2 + t_\perp^2} \left\{ \mp \tilde{\boldsymbol{d}} \cdot \tilde{\boldsymbol{s}} + i\tilde{\psi}(\boldsymbol{k}) \tilde{s}_0 \right\} i\tilde{s}_y, \tag{4.4.1}$$

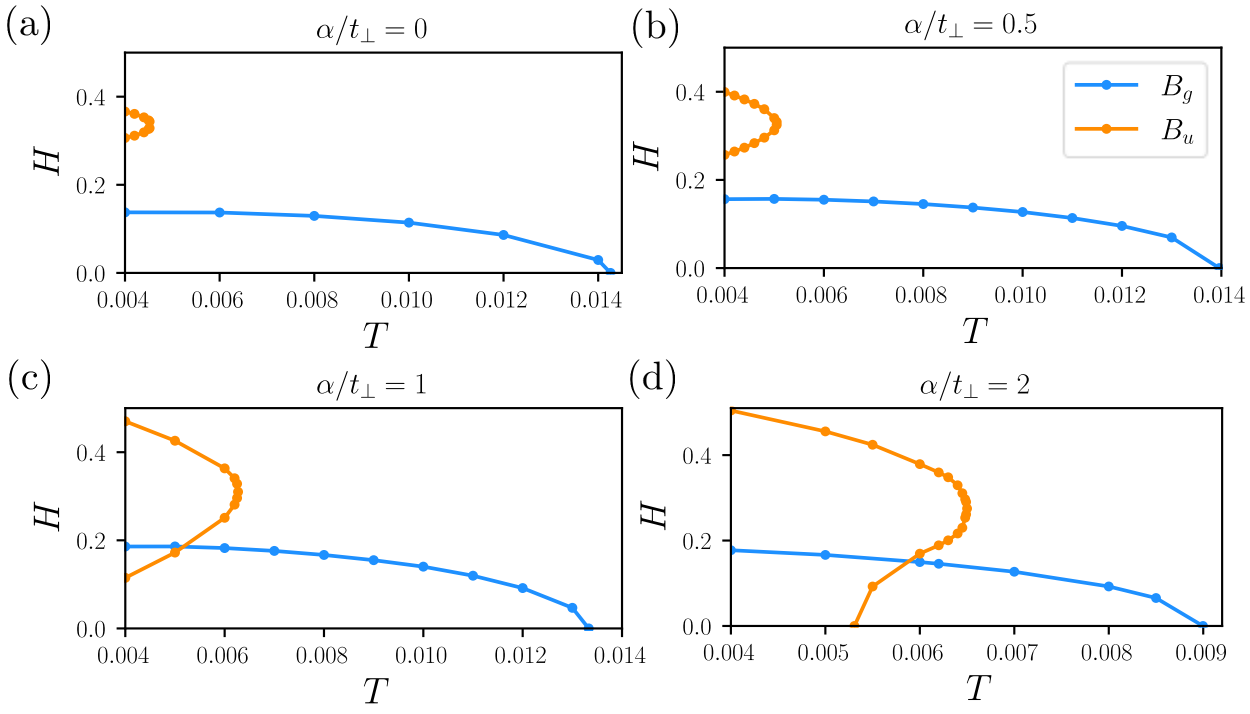

Figure 4.4: (a)-(d) H-T phase diagrams of the two-sublattice Rashba-Hubbard model for $\alpha/t_\perp = 0$, 0.5, 1, 2. We show the superconducting transition lines of the even-parity B_g and odd-parity B_u states, on which eigenvalues of the Éliashberg equation become unity.

where $\tilde{\psi}(\boldsymbol{k}) = |\boldsymbol{g}(\boldsymbol{k})|^2$ and $\tilde{\boldsymbol{d}} = [g_y(\boldsymbol{k}), g_x(\boldsymbol{k}), 0]$. These expressions demonstrate how the spin-orbit coupling, by incorporating intra-band components, significantly contributes to the thermodynamic stability of the odd-parity superconducting phase.

The field-induced odd-parity superconducting state, while robust under certain conditions, encounters a significant challenge when subjected to extremely high magnetic fields, specifically those exceeding $H > 0.3$. In such intense fields, the Pauli depairing effect, which disrupts Cooper pairs, becomes a dominant factor. Consequently, this effect leads to a decrease in the stability of the odd-parity superconducting state, manifesting as the non-monotonic behavior observed in the phase transition line of the B_u state. This nonmonotonic behavior can be understood as resulting from the interplay between two opposing influences: the enhancement of the superconducting state due to the field, particularly as facilitated by the inter-sublattice gap function, and the disruptive Pauli depairing effect under high magnetic fields. The observed phase transition line's behavior, therefore, reflects the balance between these competing mechanisms, underscoring the complex dynamics of field-induced superconductivity in the presence of high magnetic fields.

4.5 Summary

In conclusion, our study has performed a detailed multipole-resolved analysis to investigate unconventional superconductivity in strongly-correlated two-sublattice systems. A critical aspect of our findings is the lifting of degeneracy between even- and odd-parity multipole fluctuations, which leads to the emergence of an unconventional pairing channel. Our results demonstrate that the two-sublattice structure inherently encourages fluctuations predominantly of an odd-parity nature. These fluctuations, in turn, lead to the formation of sublattice-antisymmetric pairing, but only under the influence of an external magnetic field. This phenomenon results in field-induced superconductivity, a notable finding of our research. Furthermore, the phase diagrams obtained from our analysis reveal the existence of field-reentrant odd-parity superconducting states. This observation underscores the complex interplay between the two-sublattice structure, multipole fluctuations, and external magnetic fields, contributing to a deeper understanding of the mechanisms driving unconventional superconductivity in such systems [228].

Field-induced superconductivity within the bilayer model, similar to what we have explored, has been previously proposed in several studies [229, 230, 231, 232, 233]. These earlier theories generally posit that an applied magnetic field shifts the energy levels of electronic states, thereby promoting unconventional inter-band Cooper pairing. However, a crucial distinction between these models and the mechanism we present in this Chapter lies in the interaction within the layers. Unlike the earlier models which assume isotropic interaction within the layers, our proposal is fundamentally built on the concept of anisotropic effective interaction. This anisotropy is a direct consequence of degeneracy-lifted multipole fluctuations, forming the cornerstone of our theoretical framework. This distinction highlights the uniqueness of our approach in explaining field-induced superconductivity. The anisotropic nature of the effective interaction, stemming from multipole fluctuations, provides a deeper understanding of the complexities involved in the bilayer superconducting system, particularly under the influence of an external magnetic field.

In conclusion, our theoretical insights into multipole fluctuations and field-induced superconductivity could have significant implications for understanding the electronic structure of materials such as magic-angle twisted trilayer graphene. In this system, the electronic structure comprises a flat band from the moiré pattern and a dispersive Dirac band, notably in the absence of a displacement field [234, 235, 236]. The presence of the flat band could amplify degenerated multipole fluctuations, which are inherently symmetrical. A relevant example is the fifteen-fold degenerate fluctuations protected by SU(4) symmetry, as proposed in magic-angle twisted bilayer graphene [237]. When a displacement field is introduced, it leads to the hybridization of these bands, potentially resulting in the lifting of multipole fluctuation degeneracy [202]. The application of an external magnetic field in such a system could induce unconventional Cooper pairing via the degeneracy-lifted multipole fluctuations, as elucidated

in our study. This proposed mechanism may offer an explanation for the magnetic field-reentrant superconductivity observed in magic-angle twisted trilayer graphene [202]. Our theory may also find relevance in other materials such as uni-axially strained $CeRh_2As_2$ and pressurized $CeSb_2$ [200]. In these materials, pressure could amplify inter-sublattice hopping, leading to the similar lifting of multipole fluctuation degeneracy. The potential applications of our theory to these diverse and complex systems underscore the significance of our findings. Comprehensive investigations into these phenomena, particularly focusing on the interplay between electronic structures, external fields, and superconductivity, are highly anticipated and could further validate and extend the applicability of our theoretical framework.

Chapter 5

Conclusion

In this thesis, we studied a novel topological superconductivity and bulk-boundary correspondence.

In Chap. 2, we classified the group-theoretical relation and showed that the Fermi surface formula preserved by the non-symmorphic glide symmetry can be defined in the one-dimensional system in the Brillouin Zone. By virtue of the Fermi surface formula, we can determine the topological number that characterizes the emergence of the Majorana edge state on the glide-symmetry preserved surface. Calculating the electronic structure of $CeRh_2As_2$ by density functional theory calculation, we revealed the Fermi surface theoretically. Counting the number of the Fermi surface along the glide-preserved one-dimensional system, we showed that the glide-preserved topological invariants have non-trivial value in $CeRh_2As_2$. We also pointed out that the possibility of Lifshitz transition resulting in Weyl superconductivity. Finally, the demonstration of the Majorana surface state in the simple tight-binding model is given for all odd-parity irreducible representations.

In Chap. 3, we constructed non-symmorphic bilayer Rashba-Hubbard model which mimic the crystalline structure of $CeRh_2As_2$. Adopting the fluctuation exchange (FLEX) approximation, we revealed that XY-type antiferromagnetic fluctuation and resulting $d_{x^2-y^2}+p$-wave superconductivity. Following after the unity of the eigenvalue of the linearized Éliashberg equation, the phase diagrams for a wide range of the spin-orbit coupling were calculated. For all phase diagrams which shows a finite odd-parity superconducting state, the parity transition field are significantly enhanced. By this study, the discrepancy between mean-field theory and experiment is resolved.

In Chap. 4, we analyzed symmorphic two-sublattice model which is minimal model for many heavy-fermion systems. We first decompose the multipole fluctuations into the Cooper pairing channnel and showed that degeneracy-lift of multipole fluctuationos leads to the unconventional Cooper pairing. Second, the two-sublattice crystaline structure intrinsicly favoars the odd-parity multipole dominant fluctuations, especialy in the large inter-sublattice hopping. The origin is due to the nature of the wave function of the system. Third, the field-

reinforcement behavior for such parameter region is shown. The microscopic mechanism is undoerstood by the diagramatic considerations. Fourth, the calculated phase diagrams exhivit the field-induced odd-parity superconducting state for a wide range of the spin-orbit coupling.

We have contributed to the deeper understanding of the topological properties and strong correlation effect in hidden symmetry breaking superconductors, through the studies presented in Chaps. 2, 3, and 4. It is also an interesting future issue to further develop the theories presented above, as discussed in each chapter.

Bibliography

[1] T. Yoshida, M. Sigrist, and Y. Yanase, Phys. Rev. B **86**, 134514 (2012).

[2] S. Khim, J. F. Landaeta, J. Banda, N. Bannor, M. Brando, P. M. R. Brydon, D. Hafner, R. Küchler, R. Cardoso-Gil, U. Stockert, A. P. Mackenzie, D. F. Agterberg, C. Geibel, and E. Hassinger, Science **373**, 1012 (2021).

[3] S.-i. Kimura, J. Sichelschmidt, and S. Khim, Phys. Rev. B **104**, 245116 (2021).

[4] S. ichi Kimura, Y. S. Kwon, C. Krellner, and J. Sichelschmidt, Electronic Structure **3**, 024007 (2021).

[5] S.-i. Kimura, T. Iizuka, and Y.-s. Kwon, Journal of the Physical Society of Japan **78**, 013710 (2009).

[6] S.-i. Kimura, Phys. Rev. B **80**, 073103 (2009).

[7] D. Hafner, P. Khanenko, E.-O. Eljaouhari, R. Küchler, J. Banda, N. Bannor, T. Lühmann, J. F. Landaeta, S. Mishra, I. Sheikin, E. Hassinger, S. Khim, C. Geibel, G. Zwicknagl, and M. Brando, Phys. Rev. X **12**, 011023 (2022).

[8] J. F. Landaeta, P. Khanenko, D. C. Cavanagh, C. Geibel, S. Khim, S. Mishra, I. Sheikin, P. M. R. Brydon, D. F. Agterberg, M. Brando, and E. Hassinger, Phys. Rev. X **12**, 031001 (2022).

[9] S. Mishra, Y. Liu, E. D. Bauer, F. Ronning, and S. M. Thomas, Phys. Rev. B **106**, L140502 (2022).

[10] K. Semeniuk, D. Hafner, P. Khanenko, T. Lühmann, J. Banda, J. F. Landaeta, C. Geibel, S. Khim, E. Hassinger, and M. Brando, Phys. Rev. B **107**, L220504 (2023).

[11] H. Siddiquee, Z. Rehfuss, C. Broyles, and S. Ran, Phys. Rev. B **108**, L020504 (2023).

[12] M. Pfeiffer, K. Semeniuk, J. F. Landaeta, R. Borth, C. Geibel, M. Nicklas, M. Brando, S. Khim, and E. Hassinger, "Pressure-tuned quantum criticality in the locally non-centrosymmetric superconductor $cerh_2as_2$," (2023), arXiv:2312.09728 [cond-mat.str-el] .

[13] M. Pfeiffer, K. Semeniuk, J. F. Landaeta, M. Nicklas, C. Geibel, M. Brando, S. Khim, and E. Hassinger, "Exposing the odd-parity superconductivity in $cerh_2as_2$ with hydrostatic pressure," (2023), arXiv:2312.09729 [cond-mat.supr-con] .

[14] G. Zwicknagl, Reports on Progress in Physics **79**, 124501 (2016).

[15] M. Kibune, S. Kitagawa, K. Kinjo, S. Ogata, M. Manago, T. Taniguchi, K. Ishida, M. Brando, E. Hassinger, H. Rosner, C. Geibel, and S. Khim, Phys. Rev. Lett. **128**, 057002 (2022).

[16] S. Kitagawa, M. Kibune, K. Kinjo, M. Manago, T. Taniguchi, K. Ishida, M. Brando, E. Hassinger, C. Geibel, and S. Khim, Journal of the Physical Society of Japan **91**, 043702 (2022).

[17] S. Ogata, S. Kitagawa, K. Kinjo, K. Ishida, M. Brando, E. Hassinger, C. Geibel, and S. Khim, Phys. Rev. Lett. **130**, 166001 (2023).

[18] D. Maruyama, M. Sigrist, and Y. Yanase, Journal of the Physical Society of Japan **81**, 034702 (2012).

[19] S. Onishi, U. Stockert, S. Khim, J. Banda, M. Brando, and E. Hassinger, Frontiers in Electronic Materials **2** (2022), 10.3389/femat.2022.880579.

[20] M. Falkowski and A. Kowalczyk, Journal of Applied Physics **110**, 043709 (2011).

[21] V. K. Anand, D. T. Adroja, A. Bhattacharyya, B. Klemke, and B. Lake, Journal of Physics: Condensed Matter **29**, 135601 (2017).

[22] D. S. Christovam, M. Ferreira-Carvalho, A. Marino, M. Sundermann, D. Takegami, A. Melendez-Sans, K. D. Tsuei, Z. Hu, S. Roessler, M. Valvidares, M. W. Haverkort, Y. Liu, E. D. Bauer, L. H. Tjeng, G. Zwicknagl, and A. Severing, "Spectroscopic evidence of kondo-induced quasi-quartet in $cerh_2as_2$," (2023), arXiv:2308.10663 [cond-mat.str-el] .

[23] X. Chen, L. Wang, J. Ishizuka, K. Nogaki, Y. Cheng, F. Yang, R. Zhang, Z. Chen, F. Zhu, Y. Yanase, B. Lv, and Y. Huang, "Coexistence of near-ef flat band and van hove singularity in a two-phase superconductor," (2023), arXiv:2309.05895 [cond-mat.str-el] .

[24] Y. Wu, Y. Zhang, S. Ju, Y. Hu, Y. Huang, Y. Zhang, H. Zhang, H. Zheng, G. Yang, E.-O. Eljaouhari, B. Song, N. C. Plumb, F. Steglich, M. Shi, G. Zwicknagl, C. Cao, H. Yuan, and Y. Liu, "Fermi surface nesting with heavy quasiparticles in the locally noncentrosymmetric superconductor cerh2as2," (2023), arXiv:2309.06732 [cond-mat.str-el] .

[25] L. Landau and E. Lifshitz, *Statistical Physics: Volume 5* (Elsevier Science, 2013).

[26] X.-L. Qi and S.-C. Zhang, Rev. Mod. Phys. **83**, 1057 (2011).

[27] Y. Tanaka, M. Sato, and N. Nagaosa, Journal of the Physical Society of Japan **81**, 011013 (2012).

[28] M. Sato and S. Fujimoto, Journal of the Physical Society of Japan **85**, 072001 (2016).

[29] M. Sato and Y. Ando, Reports on Progress in Physics **80**, 076501 (2017).

[30] A. Y. Kitaev, Physics-Uspekhi **44**, 131 (2001).

[31] C. Nayak, S. H. Simon, A. Stern, M. Freedman, and S. Das Sarma, Rev. Mod. Phys. **80**, 1083 (2008).

[32] L. Fu and C. L. Kane, Phys. Rev. Lett. **100**, 096407 (2008).

[33] M. Sato, Y. Takahashi, and S. Fujimoto, Phys. Rev. Lett. **103**, 020401 (2009).

[34] J. D. Sau, R. M. Lutchyn, S. Tewari, and S. Das Sarma, Phys. Rev. Lett. **104**, 040502 (2010).

[35] R. M. Lutchyn, J. D. Sau, and S. Das Sarma, Phys. Rev. Lett. **105**, 077001 (2010).

[36] Y. Oreg, G. Refael, and F. von Oppen, Phys. Rev. Lett. **105**, 177002 (2010).

[37] J. Alicea, Phys. Rev. B **81**, 125318 (2010).

[38] X.-L. Qi, T. L. Hughes, and S.-C. Zhang, Phys. Rev. B **82**, 184516 (2010).

[39] S. B. Chung, X.-L. Qi, J. Maciejko, and S.-C. Zhang, Phys. Rev. B **83**, 100512(R) (2011).

[40] V. Mourik, K. Zuo, S. M. Frolov, S. R. Plissard, E. P. A. M. Bakkers, and L. P. Kouwenhoven, Science **336**, 1003 (2012).

[41] A. Das, Y. Ronen, Y. Most, Y. Oreg, M. Heiblum, and H. Shtrikman, Nature Physics **8**, 887 (2012).

[42] M. T. Deng, C. L. Yu, G. Y. Huang, M. Larsson, P. Caroff, and H. Q. Xu, Nano Letters **12**, 6414 (2012).

[43] M.-X. Wang, C. Liu, J.-P. Xu, F. Yang, L. Miao, M.-Y. Yao, C. L. Gao, C. Shen, X. Ma, X. Chen, Z.-A. Xu, Y. Liu, S.-C. Zhang, D. Qian, J.-F. Jia, and Q.-K. Xue, Science **336**, 52 (2012).

[44] S. Nadj-Perge, I. K. Drozdov, J. Li, H. Chen, S. Jeon, J. Seo, A. H. MacDonald, B. A. Bernevig, and A. Yazdani, Science **346**, 602 (2014).

[45] J.-P. Xu, C. Liu, M.-X. Wang, J. Ge, Z.-L. Liu, X. Yang, Y. Chen, Y. Liu, Z.-A. Xu, C.-L. Gao, D. Qian, F.-C. Zhang, and J.-F. Jia, Phys. Rev. Lett. **112**, 217001 (2014).

[46] J.-P. Xu, M.-X. Wang, Z. L. Liu, J.-F. Ge, X. Yang, C. Liu, Z. A. Xu, D. Guan, C. L. Gao, D. Qian, Y. Liu, Q.-H. Wang, F.-C. Zhang, Q.-K. Xue, and J.-F. Jia, Phys. Rev. Lett. **114**, 017001 (2015).

[47] J. Wang, Q. Zhou, B. Lian, and S.-C. Zhang, Phys. Rev. B **92**, 064520 (2015).

[48] H.-H. Sun, K.-W. Zhang, L.-H. Hu, C. Li, G.-Y. Wang, H.-Y. Ma, Z.-A. Xu, C.-L. Gao, D.-D. Guan, Y.-Y. Li, C. Liu, D. Qian, Y. Zhou, L. Fu, S.-C. Li, F.-C. Zhang, and J.-F. Jia, Phys. Rev. Lett. **116**, 257003 (2016).

[49] Q. L. He, L. Pan, A. L. Stern, E. C. Burks, X. Che, G. Yin, J. Wang, B. Lian, Q. Zhou, E. S. Choi, K. Murata, X. Kou, Z. Chen, T. Nie, Q. Shao, Y. Fan, S.-C. Zhang, K. Liu, J. Xia, and K. L. Wang, Science **357**, 294 (2017).

[50] G. C. Ménard, S. Guissart, C. Brun, R. T. Leriche, M. Trif, F. Debontridder, D. Demaille, D. Roditchev, P. Simon, and T. Cren, Nature Communications **8**, 2040 (2017).

[51] H. Zhang, C.-X. Liu, S. Gazibegovic, D. Xu, J. A. Logan, G. Wang, N. van Loo, J. D. S. Bommer, M. W. A. de Moor, D. Car, R. L. M. Op het Veld, P. J. van Veldhoven, S. Koelling, M. A. Verheijen, M. Pendharkar, D. J. Pennachio, B. Shojaei, J. S. Lee, C. J. Palmstrøm, E. P. A. M. Bakkers, S. D. Sarma, and L. P. Kouwenhoven, Nature **556**, 74 (2018).

[52] D. Wang, L. Kong, P. Fan, H. Chen, S. Zhu, W. Liu, L. Cao, Y. Sun, S. Du, J. Schneeloch, *et al.*, Science **362**, 333 (2018).

[53] T. Machida, Y. Sun, S. Pyon, S. Takeda, Y. Kohsaka, T. Hanaguri, T. Sasagawa, and T. Tamegai, Nature Materials **18**, 811 (2019).

[54] Z. Wang, J. O. Rodriguez, L. Jiao, S. Howard, M. Graham, G. D. Gu, T. L. Hughes, D. K. Morr, and V. Madhavan, Science **367**, 104 (2020).

[55] L. Fu and E. Berg, Phys. Rev. Lett. **105**, 097001 (2010).

[56] M. Sato, Phys. Rev. B **81**, 220504(R) (2010).

[57] P. Hosur, P. Ghaemi, R. S. K. Mong, and A. Vishwanath, Phys. Rev. Lett. **107**, 097001 (2011).

[58] L. Fu, Phys. Rev. B **90**, 100509(R) (2014).

[59] P. Hosur, X. Dai, Z. Fang, and X.-L. Qi, Phys. Rev. B **90**, 045130 (2014).

[60] S. Kobayashi and M. Sato, Phys. Rev. Lett. **115**, 187001 (2015).

[61] Z. Wang, P. Zhang, G. Xu, L. K. Zeng, H. Miao, X. Xu, T. Qian, H. Weng, P. Richard, A. V. Fedorov, H. Ding, X. Dai, and Z. Fang, Phys. Rev. B **92**, 115119 (2015).

[62] G. Xu, B. Lian, P. Tang, X.-L. Qi, and S.-C. Zhang, Phys. Rev. Lett. **117**, 047001 (2016).

[63] Y. Pan, A. M. Nikitin, G. K. Araizi, Y. K. Huang, Y. Matsushita, T. Naka, and A. de Visser, Scientific Reports **6**, 28632 (2016).

[64] K. Matano, M. Kriener, K. Segawa, Y. Ando, and G.-q. Zheng, Nature Physics **12**, 852 (2016).

[65] S. Yonezawa, K. Tajiri, S. Nakata, Y. Nagai, Z. Wang, K. Segawa, Y. Ando, and Y. Maeno, Nature Physics **13**, 123 (2017).

[66] P. Zhang, K. Yaji, T. Hashimoto, Y. Ota, T. Kondo, K. Okazaki, Z. Wang, J. Wen, G. D. Gu, H. Ding, and S. Shin, Science **360**, 182 (2018).

[67] T. Yoshida and Y. Yanase, Phys. Rev. B **93**, 054504 (2016).

[68] A. Daido and Y. Yanase, Phys. Rev. B **94**, 054519 (2016).

[69] O. Can, T. Tummuru, R. P. Day, I. Elfimov, A. Damascelli, and M. Franz, Nature Physics **17**, 519 (2021).

[70] A. P. Schnyder, S. Ryu, A. Furusaki, and A. W. W. Ludwig, Phys. Rev. B **78**, 195125 (2008).

[71] A. Kitaev, AIP Conf. Proc. **1134**, 22 (2009).

[72] S. Ryu, A. P. Schnyder, A. Furusaki, and A. W. W. Ludwig, New J. Phys. **12**, 065010 (2010).

[73] L. Fu, Phys. Rev. Lett. **106**, 106802 (2011).

[74] F. Zhang, C. L. Kane, and E. J. Mele, Phys. Rev. Lett. **111**, 056403 (2013).

[75] C.-K. Chiu, H. Yao, and S. Ryu, Phys. Rev. B **88**, 075142 (2013).

[76] T. Morimoto and A. Furusaki, Phys. Rev. B **88**, 125129 (2013).

[77] Y. Ueno, A. Yamakage, Y. Tanaka, and M. Sato, Phys. Rev. Lett. **111**, 087002 (2013).

[78] Y. Tsutsumi, M. Ishikawa, T. Kawakami, T. Mizushima, M. Sato, M. Ichioka, and K. Machida, Journal of the Physical Society of Japan **82**, 113707 (2013).

[79] K. Shiozaki and M. Sato, Phys. Rev. B **90**, 165114 (2014).

[80] C.-K. Chiu and A. P. Schnyder, Phys. Rev. B **90**, 205136 (2014).

[81] T. Yoshida, M. Sigrist, and Y. Yanase, Phys. Rev. Lett. **115**, 027001 (2015).

[82] C. Fang and L. Fu, Phys. Rev. B **91**, 161105(R) (2015).

[83] K. Shiozaki, M. Sato, and K. Gomi, Phys. Rev. B **91**, 155120 (2015).

[84] K. Shiozaki, M. Sato, and K. Gomi, Phys. Rev. B **93**, 195413 (2016).

[85] H. Shapourian, Y. Wang, and S. Ryu, Phys. Rev. B **97**, 094508 (2018).

[86] Y. Yanase and K. Shiozaki, Phys. Rev. B **95**, 224514 (2017).

[87] A. Daido, T. Yoshida, and Y. Yanase, Phys. Rev. Lett. **122**, 227001 (2019).

[88] S. Ono, Y. Yanase, and H. Watanabe, Phys. Rev. Research **1**, 013012 (2019).

[89] S. Ono, H. C. Po, and H. Watanabe, Science Advances **6**, eaaz8367 (2020).

[90] S. Ono, H. C. Po, and K. Shiozaki, Phys. Rev. Research **3**, 023086(R) (2021).

[91] A. Skurativska, T. Neupert, and M. H. Fischer, Phys. Rev. Research **2**, 013064 (2020).

[92] M. Geier, P. W. Brouwer, and L. Trifunovic, Phys. Rev. B **101**, 245128 (2020).

[93] K. Shiozaki, "Variants of the symmetry-based indicator," (2019), arXiv:1907.13632 [cond-mat.mes-hall] .

[94] J. Ahn and B.-J. Yang, Phys. Rev. Research **2**, 012060(R) (2020).

[95] M. Sigrist and K. Ueda, Rev. Mod. Phys. **63**, 239 (1991).

[96] R. Joynt and L. Taillefer, Rev. Mod. Phys. **74**, 235 (2002).

[97] D. Braithwaite, M. Vališka, G. Knebel, G. Lapertot, J.-P. Brison, A. Pourret, M. E. Zhitomirsky, J. Flouquet, F. Honda, and D. Aoki, Communications Physics **2**, 147 (2019).

[98] S. Ran, H. Kim, I.-L. Liu, S. R. Saha, I. Hayes, T. Metz, Y. S. Eo, J. Paglione, and N. P. Butch, Phys. Rev. B **101**, 140503(R) (2020).

[99] D. Aoki, F. Honda, G. Knebel, D. Braithwaite, A. Nakamura, D. Li, Y. Homma, Y. Shimizu, Y. J. Sato, J.-P. Brison, and J. Flouquet, J. Phys. Soc. Jpn. **89**, 053705 (2020).

[100] J. Ishizuka and Y. Yanase, Phys. Rev. B **103**, 094504 (2021).

[101] E. G. Schertenleib, M. H. Fischer, and M. Sigrist, Phys. Rev. Research **3**, 023179 (2021).

[102] D. Möckli and A. Ramires, Phys. Rev. Research **3**, 023204 (2021).

[103] A. Ptok, K. J. Kapcia, P. T. Jochym, J. Łażewski, A. M. Oleś, and P. Piekarz, Phys. Rev. B **104**, L041109 (2021).

[104] D. C. Cavanagh, T. Shishidou, M. Weinert, P. M. R. Brydon, and D. F. Agterberg, Phys. Rev. B **105**, L020505 (2022).

[105] V. M. Edel'shtein, Soviet Physics - JETP (English Translation) **68**, 1244 (1989).

[106] V. M. Edelstein, Phys. Rev. Lett. **75**, 2004 (1995).

[107] E. Bauer, G. Hilscher, H. Michor, C. Paul, E. W. Scheidt, A. Gribanov, Y. Seropegin, H. Noël, M. Sigrist, and P. Rogl, Phys. Rev. Lett. **92**, 027003 (2004).

[108] D. F. Agterberg and R. P. Kaur, Phys. Rev. B **75**, 064511 (2007).

[109] E. Bauer and M. Sigrist, *Non-centrosymmetric superconductors: introduction and overview*, Vol. 847 (Springer Science & Business Media, 2012).

[110] Y. Saito, Y. Nakamura, M. S. Bahramy, Y. Kohama, J. Ye, Y. Kasahara, Y. Nakagawa, M. Onga, M. Tokunaga, T. Nojima, Y. Yanase, and Y. Iwasa, Nature Physics **12**, 144 (2016).

[111] M. Smidman, M. B. Salamon, H. Q. Yuan, and D. F. Agterberg, Reports on Progress in Physics **80**, 036501 (2017).

[112] R. Wakatsuki and N. Nagaosa, Phys. Rev. Lett. **121**, 026601 (2018).

[113] F. Ando, Y. Miyasaka, T. Li, J. Ishizuka, T. Arakawa, Y. Shiota, T. Moriyama, Y. Yanase, and T. Ono, Nature **584**, 373 (2020).

[114] K. Nogaki and Y. Yanase, Phys. Rev. B **102**, 165114 (2020).

[115] M. H. Fischer, F. Loder, and M. Sigrist, Phys. Rev. B **84**, 184533 (2011).

[116] D. Maruyama, M. Sigrist, and Y. Yanase, Journal of the Physical Society of Japan **82**, 043703 (2013).

[117] T. Yoshida, M. Sigrist, and Y. Yanase, Journal of the Physical Society of Japan **82**, 074714 (2013).

[118] T. Yoshida, M. Sigrist, and Y. Yanase, Journal of the Physical Society of Japan **83**, 013703 (2014).

[119] M. Shimozawa, S. K. Goh, T. Shibauchi, and Y. Matsuda, Reports on Progress in Physics **79**, 074503 (2016).

[120] Y. Nakamura and Y. Yanase, Phys. Rev. B **96**, 054501 (2017).

[121] D. Möckli, Y. Yanase, and M. Sigrist, Phys. Rev. B **97**, 144508 (2018).

[122] A. Skurativska, M. Sigrist, and M. H. Fischer, Phys. Rev. Research **3**, 033133 (2021).

[123] J. Ishizuka, S. Sumita, A. Daido, and Y. Yanase, Phys. Rev. Lett. **123**, 217001 (2019).

[124] P. Blaha, K. Schwarz, G. Madsen, D. Kvasnicka, J. Luitz, R. Laskowsk, F. Tran, L. Marks, and L. Marks, *WIEN2k: An Augmented Plane Wave Plus Local Orbitals Program for Calculating Crystal Properties* (Techn. Universitat, 2019).

[125] A. Kokalj, Journal of Molecular Graphics and Modelling **17**, 176 (1999).

[126] Y. Yanase, Phys. Rev. B **94**, 174502 (2016).

[127] K. Nogaki, A. Daido, J. Ishizuka, and Y. Yanase, Phys. Rev. Research **3**, L032071 (2021).

[128] J. Bardeen, L. N. Cooper, and J. R. Schrieffer, Phys. Rev. **108**, 1175 (1957).

[129] D. Aoki and J. Flouquet, Journal of the Physical Society of Japan **83**, 061011 (2014).

[130] D. Aoki, K. Ishida, and J. Flouquet, Journal of the Physical Society of Japan **88**, 022001 (2019).

[131] H. Fujibayashi, G. Nakamine, K. Kinjo, S. Kitagawa, K. Ishida, Y. Tokunaga, H. Sakai, S. Kambe, A. Nakamura, Y. Shimizu, Y. Homma, D. Li, F. Honda, and D. Aoki, Journal of the Physical Society of Japan **91**, 043705 (2022).

[132] Y. Higashi, Y. Nagai, T. Yoshida, Y. Masaki, and Y. Yanase, Phys. Rev. B **93**, 104529 (2016).

[133] S.-L. Wu, K. Sumida, K. Miyamoto, K. Taguchi, T. Yoshikawa, A. Kimura, Y. Ueda, M. Arita, M. Nagao, S. Watauchi, I. Tanaka, and T. Okuda, Nature Communications **8**, 1919 (2017).

[134] K. Gotlieb, C.-Y. Lin, M. Serbyn, W. Zhang, C. L. Smallwood, C. Jozwiak, H. Eisaki, Z. Hussain, A. Vishwanath, and A. Lanzara, Science **362**, 1271 (2018).

[135] M. H. Fischer, M. Sigrist, D. F. Agterberg, and Y. Yanase, Annual Review of Condensed Matter Physics **14**, 153 (2023).

[136] A. Pourret and G. Knebel, Science **373**, 962 (2021).

[137] D. Möckli and A. Ramires, Phys. Rev. B **104**, 134517 (2021).

[138] T. Hazra and P. Coleman, Phys. Rev. Lett. **130**, 136002 (2023).

[139] T. Moriya and K. Ueda, Advances in Physics **49**, 555 (2000).

[140] L. Craco, Phys. Rev. B **104**, 064509 (2021).

[141] X. Lu and D. Sénéchal, Phys. Rev. B **104**, 024502 (2021).

[142] K. Shigeta, S. Onari, and Y. Tanaka, Journal of the Physical Society of Japan **82**, 014702 (2013).

[143] Y. Fujimoto, K. Miyake, and H. Matsuura, Journal of the Physical Society of Japan **84**, 043702 (2015).

[144] D. Maruyama and Y. Yanase, Journal of the Physical Society of Japan **84**, 074702 (2015).

[145] A. Greco and A. P. Schnyder, Phys. Rev. Lett. **120**, 177002 (2018).

[146] X. Lu and D. Sénéchal, Phys. Rev. B **98**, 245118 (2018).

[147] R. Ghadimi, M. Kargarian, and S. A. Jafari, Phys. Rev. B **99**, 115122 (2019).

[148] A. Greco, M. Bejas, and A. P. Schnyder, Phys. Rev. B **101**, 174420 (2020).

[149] S. Wolf and S. Rachel, Phys. Rev. B **102**, 174512 (2020).

[150] M. J. Trott and C. A. Hooley, Phys. Rev. Research **2**, 013106 (2020).

[151] R. Soni, A. B. Sanyal, N. Kaushal, S. Okamoto, A. Moreo, and E. Dagotto, Phys. Rev. B **104**, 235115 (2021).

[152] M. Biderang, M.-H. Zare, and J. Sirker, Phys. Rev. B **105**, 064504 (2022).

[153] N. E. Bickers and S. R. White, Phys. Rev. B **43**, 8044 (1991).

[154] N. Bulut, D. J. Scalapino, and S. R. White, Phys. Rev. B **47**, 2742 (1993).

[155] N. Bulut, D. J. Scalapino, and S. R. White, Phys. Rev. B **47**, 6157 (1993).

[156] N. Bulut, D. Scalapino, and S. White, Physica C: Superconductivity **246**, 85 (1995).

[157] N. Bulut, Advances in Physics **51**, 1587 (2002).

[158] H. Watanabe and Y. Yanase, Phys. Rev. B **98**, 245129 (2018).

[159] S. Hayami, M. Yatsushiro, Y. Yanagi, and H. Kusunose, Phys. Rev. B **98**, 165110 (2018).

[160] M. Yatsushiro, H. Kusunose, and S. Hayami, Phys. Rev. B **104**, 054412 (2021).

[161] S. Sumita and Y. Yanase, Phys. Rev. B **93**, 224507 (2016).

[162] Y. Yanase, Journal of the Physical Society of Japan **77**, 063705 (2008).

[163] K. Nogaki and Y. Yanase, Phys. Rev. B **106**, L100504 (2022).

[164] M. Tinkham, *Introduction to superconductivity*, 2nd ed. (Dover Publications Mineola, N.Y., Mineola, N.Y., 2004).

[165] V. Jaccarino and M. Peter, Phys. Rev. Lett. **9**, 290 (1962).

[166] O. H. Fischer, Helv. Phys. Acta. **45**, 331 (1972).

[167] H. W. Meul, C. Rossel, M. Decroux, O. Fischer, G. Remenyi, and A. Briggs, Phys. Rev. Lett. **53**, 497 (1984).

[168] O. Fischer, H. W. Meul, M. G. Karkut, G. Remenyi, U. Welp, J. C. Piccoche, and K. Maki, Phys. Rev. Lett. **55**, 2972 (1985).

[169] S. Uji, H. Shinagawa, T. Terashima, T. Yakabe, Y. Terai, M. Tokumoto, A. Kobayashi, H. Tanaka, and H. Kobayashi, Nature **410**, 908 (2001).

[170] L. Balicas, J. S. Brooks, K. Storr, S. Uji, M. Tokumoto, H. Tanaka, H. Kobayashi, A. Kobayashi, V. Barzykin, and L. P. Gor'kov, Phys. Rev. Lett. **87**, 067002 (2001).

[171] T. Konoike, S. Uji, T. Terashima, M. Nishimura, S. Yasuzuka, K. Enomoto, H. Fujiwara, B. Zhang, and H. Kobayashi, Phys. Rev. B **70**, 094514 (2004).

[172] A. N. Podmarkov and I. S. Sandalov, Superconductor Science and Technology **2**, 66 (1989).

[173] A. N. Podmarkov and I. S. Sandalov, Journal of Experimental and Theoretical Physics **68**, 1291 (1989).

[174] M. Tachiki, B. D. Dunlap, G. W. Crabtree, S. Takahashi, and T. Koyama, Phys. Rev. B **34**, 7603 (1986).

[175] S. S. Saxena, P. Agarwal, K. Ahilan, F. M. Grosche, R. K. W. Haselwimmer, M. J. Steiner, E. Pugh, I. R. Walker, S. R. Julian, P. Monthoux, G. G. Lonzarich, A. Huxley, I. Sheikin, D. Braithwaite, and J. Flouquet, Nature **406**, 587 (2000).

[176] I. Sheikin, A. Huxley, D. Braithwaite, J. P. Brison, S. Watanabe, K. Miyake, and J. Flouquet, Phys. Rev. B **64**, 220503 (2001).

[177] D. Aoki, A. Huxley, E. Ressouche, D. Braithwaite, J. Flouquet, J.-P. Brison, E. Lhotel, and C. Paulsen, Nature **413**, 613 (2001).

[178] F. Lévy, I. Sheikin, B. Grenier, and A. D. Huxley, Science **309**, 1343 (2005).

[179] N. T. Huy, A. Gasparini, D. E. de Nijs, Y. Huang, J. C. P. Klaasse, T. Gortenmulder, A. de Visser, A. Hamann, T. Görlach, and H. v. Löhneysen, Phys. Rev. Lett. **99**, 067006 (2007).

[180] D. Aoki, T. D. Matsuda, V. Taufour, E. Hassinger, G. Knebel, and J. Flouquet, Journal of the Physical Society of Japan **78**, 113709 (2009).

[181] S. Ran, C. Eckberg, Q.-P. Ding, Y. Furukawa, T. Metz, S. R. Saha, I.-L. Liu, M. Zic, H. Kim, J. Paglione, and N. P. Butch, Science **365**, 684 (2019).

[182] S. Ran, I.-L. Liu, Y. S. Eo, D. J. Campbell, P. M. Neves, W. T. Fuhrman, S. R. Saha, C. Eckberg, H. Kim, D. Graf, F. Balakirev, J. Singleton, J. Paglione, and N. P. Butch, Nature Physics **15**, 1250 (2019).

[183] G. Knebel, W. Knafo, A. Pourret, Q. Niu, M. Vališka, D. Braithwaite, G. Lapertot, M. Nardone, A. Zitouni, S. Mishra, I. Sheikin, G. Seyfarth, J.-P. Brison, D. Aoki, and J. Flouquet, Journal of the Physical Society of Japan **88**, 063707 (2019).

[184] T. Hattori, Y. Ihara, Y. Nakai, K. Ishida, Y. Tada, S. Fujimoto, N. Kawakami, E. Osaki, K. Deguchi, N. K. Sato, and I. Satoh, Phys. Rev. Lett. **108**, 066403 (2012).

[185] K. Hattori and H. Tsunetsugu, Phys. Rev. B **87**, 064501 (2013).

[186] Y. Tada, S. Fujimoto, N. Kawakami, T. Hattori, Y. Ihara, K. Ishida, K. Deguchi, N. K. Sato, and I. Satoh, Journal of Physics: Conference Series **449**, 012029 (2013).

[187] T. Hattori, K. Karube, K. Ishida, K. Deguchi, N. K. Sato, and T. Yamamura, Journal of the Physical Society of Japan **83**, 073708 (2014).

[188] Y. Tokunaga, D. Aoki, H. Mayaffre, S. Krämer, M.-H. Julien, C. Berthier, M. Horvatić, H. Sakai, S. Kambe, and S. Araki, Phys. Rev. Lett. **114**, 216401 (2015).

[189] Y. Tokunaga, D. Aoki, H. Mayaffre, S. Krämer, M.-H. Julien, C. Berthier, M. Horvatić, H. Sakai, T. Hattori, S. Kambe, and S. Araki, Phys. Rev. B **93**, 201112 (2016).

[190] Y. Tada, S. Takayoshi, and S. Fujimoto, Phys. Rev. B **93**, 174512 (2016).

[191] B. Wu, G. Bastien, M. Taupin, C. Paulsen, L. Howald, D. Aoki, and J.-P. Brison, Nature Communications **8**, 14480 (2017).

[192] A. Rosuel, C. Marcenat, G. Knebel, T. Klein, A. Pourret, N. Marquardt, Q. Niu, S. Rousseau, A. Demuer, G. Seyfarth, G. Lapertot, D. Aoki, D. Braithwaite, J. Flouquet, and J. P. Brison, Phys. Rev. X **13**, 011022 (2023).

[193] K. Machida, Phys. Rev. B **106**, 184509 (2022).

[194] C. Lee and S. B. Chung, "Linear optical response from the odd parity bardasis-schrieffer mode in locally non-centrosymmetric superconductors," (2022), arXiv:2212.13722 [cond-mat.supr-con] .

[195] N. A. Hackner and P. M. R. Brydon, "Bardasis-schrieffer-like phase mode in a superconducting bilayer," (2023), arXiv:2306.16611 [cond-mat.supr-con] .

[196] A. L. Szabó, M. H. Fischer, and M. Sigrist, "Effects of nucleation at a first-order transition between two superconducting phases: Application to $cerh_2as_2$," (2023), arXiv:2307.10374 [cond-mat.supr-con] .

[197] A. Szabo and A. Ramires, "Superconductivity-induced improper orders," (2023), arXiv:2309.05664 [cond-mat.supr-con] .

[198] J. Ishizuka, K. Nogaki, M. Sigrist, and Y. Yanase, "Correlation-induced fermi surface evolution and topological crystalline superconductivity in cerh2as2," (2023), arXiv:2311.00324 [cond-mat.supr-con] .

[199] P. C. Canfield, J. D. Thompson, and Z. Fisk, Journal of Applied Physics **70**, 5992 (1991).

[200] O. P. Squire, S. A. Hodgson, J. Chen, V. Fedoseev, C. K. de Podesta, T. I. Weinberger, P. L. Alireza, and F. M. Grosche, Phys. Rev. Lett. **131**, 026001 (2023).

[201] J. M. Park, Y. Cao, K. Watanabe, T. Taniguchi, and P. Jarillo-Herrero, Nature **590**, 249 (2021).

[202] Y. Cao, J. M. Park, K. Watanabe, T. Taniguchi, and P. Jarillo-Herrero, Nature **595**, 526 (2021).

[203] J. C. Ward, Phys. Rev. **78**, 182 (1950).

[204] Y. Takahashi, Il Nuovo Cimento (1955-1965) **6**, 371 (1957).

[205] V. Kozii and L. Fu, Phys. Rev. Lett. **115**, 207002 (2015).

[206] S. Sumita and Y. Yanase, Phys. Rev. Res. **2**, 033225 (2020).

[207] N. E. Bickers, D. J. Scalapino, and S. R. White, Phys. Rev. Lett. **62**, 961 (1989).

[208] N. Bickers and D. Scalapino, Annals of Physics **193**, 206 (1989).

[209] N. E. Bickers and S. R. White, Phys. Rev. B **43**, 8044 (1991).

[210] B. Roulet, J. Gavoret, and P. Nozières, Phys. Rev. **178**, 1072 (1969).

[211] N. E. Bickers, "Self-consistent many-body theory for condensed matter systems," in *Theoretical Methods for Strongly Correlated Electrons*, edited by D. Sénéchal, A.-M. Tremblay, and C. Bourbonnais (Springer New York, New York, NY, 2004) pp. 237–296.

[212] Y. Yanase, Journal of the Physical Society of Japan **79**, 084701 (2010).

[213] T. Hitomi and Y. Yanase, Journal of the Physical Society of Japan **85**, 124702 (2016).

[214] in *Multiplets of Transition-Metal Ions in Crystals*, Pure and Applied Physics, Vol. 33, edited by S. Sugano, Y. Tanabe, and H. Kamimura (Elsevier, 1970) pp. 38–65.

[215] A. C. Simmonett, I. Pickard, Frank C., I. Schaefer, Henry F., and B. R. Brooks, The Journal of Chemical Physics **140**, 184101 (2014).

[216] M. E. A. Coury, S. L. Dudarev, W. M. C. Foulkes, A. P. Horsfield, P.-W. Ma, and J. S. Spencer, Phys. Rev. B **93**, 075101 (2016).

[217] J. Bünemann and F. Gebhard, Journal of Physics: Condensed Matter **29**, 165601 (2017).

[218] S. Iimura, M. Hirayama, and S. Hoshino, Phys. Rev. B **104**, L081108 (2021).

[219] S. J. Youn, M. H. Fischer, S. H. Rhim, M. Sigrist, and D. F. Agterberg, Phys. Rev. B **85**, 220505 (2012).

[220] J. Goryo, M. H. Fischer, and M. Sigrist, Phys. Rev. B **86**, 100507 (2012).

[221] J. M. Luttinger and J. C. Ward, Phys. Rev. **118**, 1417 (1960).

[222] J. M. Luttinger, Phys. Rev. **119**, 1153 (1960).

[223] G. Baym and L. P. Kadanoff, Phys. Rev. **124**, 287 (1961).

[224] G. Baym, Phys. Rev. **127**, 1391 (1962).

[225] H. Yao and F. Yang, Phys. Rev. B **92**, 035132 (2015).

[226] X. Wu, M. Fink, W. Hanke, R. Thomale, and D. Di Sante, Phys. Rev. B **100**, 041117 (2019).

[227] Y. Yanase, T. Jujo, T. Nomura, H. Ikeda, T. Hotta, and K. Yamada, Physics Reports **387**, 1 (2003).

[228] K. Nogaki and Y. Yanase, "Field-induced superconductivity mediated by odd-parity multipole fluctuation," (2023), arXiv:2312.07053 [cond-mat.supr-con] .

[229] M. Houzet and A. Buzdin, Europhysics Letters **58**, 596 (2002).

[230] A. Buzdin, S. Tollis, and J. Cayssol, Phys. Rev. Lett. **95**, 167003 (2005).

[231] S. Tollis, J. Cayssol, and A. Buzdin, Phys. Rev. B **73**, 174519 (2006).

[232] A. Buzdin, S. Tollis, and J. Cayssol, Physica C: Superconductivity **460-462**, 1028 (2007), proceedings of the 8th International Conference on Materials and Mechanisms of Superconductivity and High Temperature Superconductors.

[233] X. Montiel and A. I. Buzdin, Phys. Rev. B **84**, 054518 (2011).

[234] E. Khalaf, A. J. Kruchkov, G. Tarnopolsky, and A. Vishwanath, Phys. Rev. B **100**, 085109 (2019).

[235] S. Carr, C. Li, Z. Zhu, E. Kaxiras, S. Sachdev, and A. Kruchkov, Nano Letters **20**, 3030 (2020).

[236] C. Lei, L. Linhart, W. Qin, F. Libisch, and A. H. MacDonald, Phys. Rev. B **104**, 035139 (2021).

[237] S. Onari and H. Kontani, Phys. Rev. Lett. **128**, 066401 (2022).

[238] M. Wallerberger, S. Badr, S. Hoshino, S. Huber, F. Kakizawa, T. Koretsune, Y. Nagai, K. Nogaki, T. Nomoto, H. Mori, J. Otsuki, S. Ozaki, T. Plaikner, R. Sakurai, C. Vogel, N. Witt, K. Yoshimi, and H. Shinaoka, SoftwareX **21**, 101266 (2023).

[239] K. Nogaki and H. Shinaoka, Journal of the Physical Society of Japan **92**, 035001 (2023).

[240] H. Shinaoka, M. Wallerberger, Y. Murakami, K. Nogaki, R. Sakurai, P. Werner, and A. Kauch, Phys. Rev. X **13**, 021015 (2023).

[241] K. Nogaki, J. Fei, E. Gull, and H. Shinaoka, SciPost Phys. Codebases , 19 (2023).

Acknowledgment

I would like to express my sincere gratitude to my exceptional supervisor, Prof. Youichi Yanase, for his helpful and careful supervision. His advice, ranging from physics to the life of a scientist, has played *the* essential and indispensable role throughout my master's and doctoral courses. Without his supervision, I would not have been able to complete my work or enjoy my daily life in graduate school.

I am also deeply thankful to Prof. Akito Daido and Prof. Jun Ishizuka for the fruitful collaboration on the work presented in Chap. 2. I am profoundly grateful to Prof. Hiroshi Shinaoka for his dedication to our collaboration [238, 239, 240, 241]. Although the work conducted with him is not presented in this thesis, my experience in computational physics was priceless, providing me with exciting insights and wisdom. I extend my gratitude to the staff of the Condensed Matter Theory Group at Kyoto University, including Prof. Norio Kawakami, Prof. Ryusuke Ikeda, Prof. Tsuneya Yoshida, Prof. Robert Peters, and Prof. Masaki Tezuka.

I acknowledge the financial support from the Japan Society for the Promotion of Science (JSPS) KAKENHI (Grant Nos. JP21J23007 and JP22KJ1716), and the Research Grants of the WISE Program, MEXT at Kyoto University, in 2020 and 2022.

Lastly, I wish to convey my deepest appreciation to my family, especially my parents, Yukikazu and Yoshimi, for their invaluable, irreplaceable, and inexhaustible affection throughout my whole life.